ELECTRONIC STATES AND OPTICAL TRANSITIONS IN BULK AND QUANTUM WELL STRUCTURES OF III-V COMPOUND SEMICONDUCTORS

A Dissertation

by

YONG HEE CHO

Submitted to the Office of Graduate Studies of
Texas A&M University
in partial fulfillment of the requirements for the degree of

DOCTOR OF PHILOSOPHY

May 2011

Major Subject: Physics

ELECTRONIC STATES AND OPTICAL TRANSITIONS IN BULK AND QUANTUM WELL STRUCTURES OF III-V COMPOUND SEMICONDUCTORS

A Dissertation

by

YONG HEE CHO

Submitted to the Office of Graduate Studies of
Texas A&M University
in partial fulfillment of the requirements for the degree of

DOCTOR OF PHILOSOPHY

Approved by:

Chair of Committee,	Alexey Belyanin
Committee Members,	Olga Kocharovskaya
	Jairo Sinova
	Ohannes Eknoyan
Head of Department,	Edward Fry

May 2011

Major Subject: Physics

ABSTRACT

Electronic States and Optical Transitions in Bulk and

Quantum Well Structures of III-V Compound Semiconductors.

(May 2011)

Yong Hee Cho, B.S., Hanyang University at Seoul

Chair of Advisory Committee: Dr. Alexey Belyanin

In this work we apply the methods of band structure calculation combined with a self-consistent treatment of the light-matter interaction to a variety of problems in bulk semiconductors and semiconductor heterostructures as well as in new optoelectronic devices.

In particular, we utilize the 30- and 8-band k • p band structure calculation methods to study the electronic, magnetic, and optical properties of the diluted magnetic semiconductor, GaMnAs, in the mean-field Zener model. We calculate the anisotropic dielectric response of GaMnAs in the metallic regime and show that our model produces a good agreement with the experimental results of magneto-optical Kerr spectroscopy in the interband transition region. We also discuss the advantages of the 30-band k • p model for spin-polarized ferromagnetic GaMnAs.

We present new methods for calculating electronic states in low-dimensional semiconductor heterostructures based on the real-space Hamiltonian. The formalism provides an extremely simple numerical implementation that gives accurate results. It is

applicable to a general *n*-band k • p model; we specifically test it in the 6- and 8-band k • p models, and a simple parabolic one band model. Spurious solutions have long been a major issue in low- dimensional band structure calculations. The transparency of the new method allows us to investigate the origin of both types of spurious solutions in a unified manner and eliminate fast oscillating spurious solutions.

We apply this method to two-dimensional nonlinear optical semiconductor heterostructures. We calculate the upper limits on the efficiency of the passive terahertz difference frequency generation based on the intersubband resonant nonlinearity. Our approach incorporates electronic states together with propagating coupled fields through a self-consistent calculation of the Poisson equation, density matrix equations, and coupled wave equations. We develop optimal device geometries and systematically study the device performance as a function of various parameters. The results are compared with a simplified analytic solution.

ACKNOWLEDGEMENTS

First of all, I would like to express my deep appreciation to Dr. Alexey Belyanin. As my dissertation advisor, his patience, endurance, and guidance are foremost respected. The uncountable discussions with him became driving force in successfully finishing my Ph.D program. Without doubt, his academic network as a result of his achievements gave me valuable opportunities to meet and to collaborate with great scholars in other universities as well as in TAMU. While proceeding with multiple projects together, sometimes as a teacher and sometimes as a warm colleague, he made me simultaneously expand my problem-solving experiences and capabilities. Also, I want to thank him for financial support from the time I joined his group until my graduation as well as for his generous support and encouragement to present my research at many professional conferences.

I also would like to thank my committee members, Dr. Olga Kocharovskaya, Dr. Ohannes Eknoyan, and Dr. Jairo Sinova, for their guidance, time, and interest in my research. Especially, I would give special thanks to Dr. Sinova for valuable discussions on DMS and multiple suggestions for important issues in the related subject.

As an associate on collaborating projects (MOKE in GaMnAs and THz DFG), I am grateful to Dr. Junichiro Kono and Dr. Chanjuan Sun (currently in CGG Veritas) at Rice University, Dr. Hiro Munekata in the Tokyo Institute of Technology, and Dr. Mikhail Belkin in the University of Texas at Austin not only for providing experimental

data, but also for many valuable discussions about the challenging work, our efforts to write Journal publications, and prospective suggestions for future research.

My gratitude is also given to Dr. Myunghwan Kim at the University of Maryland for giving me his advice on the subject of MOKE based on his experimental know-how and to Dr. Soondo Kweon in the Aerospace Engineering Department at TAMU for helping me to expand my viewpoint on numerical simulations.

Also, I can not forget to express my appreciation to Dr. Gerhard Paulus, my former advisor, for giving me hard training and guidance to many skills in experiments as well as in software and programming for the very first year and a half in TAMU. I am sure that they became the rudiment for later research.

I would extend my appreciation to the faculty members in the Physics Department, Dr. Pokrovsky, Dr. Pope, Dr. Agnolet, Dr. McIntyre, Dr. Saslow, Dr. Finkelstein, Dr. Nanopoulos, and Dr. Keldysh for making me jump to the next level through advanced course work and for making me view physics problems from various angles. Also, I greatly appreciate the staff members in the department for helping me through administrative work. Particularly, I would like to thank Sandi Smith for her care in many important academic affairs and Tom Weimer for his concern and support even before and after my TA position in the course of Scientific Instrument Making back in Spring 2007.

Also, many thanks go to Dr. Jaewoong Yoon, Jaehong Park, Heesung Choi, Heedeuk Shin, and my fellow Korean students in the TAMU Physics Department, and my many friends in VMC and in KATC for sharing their research fields and broad

interests in daily life, and for helping me settle down in an unfamiliar environment during my first year in College Station.

Lastly, I would like to thank my parents, Jong-Gyu Cho and Jin Yang, who consistently prayed with sincerity and devotion for my health and study. Especially, my mother's unflagging encouragement through consistent weekly emails is memorable and priceless. Also, I wish to thank my brother, Yong-Rok Cho, and his wife, Jee-Hye Lee, and their children, Gyu-Hyun and Seo-Hyun for their warm support.

NOMENCLATURE

AlInAs	Aluminum Indium Arsenide
χ	Optical Susceptibility
CB	Conduction Band
Cd	Cadmium
DFG	Difference Frequency Generation
DFM	Delta Function Method
DQW	Double Quantum Well
ε_{ij}	Dielectric Tensor Components
ε_F	Fermi Energy
$\varepsilon_{ij}^{strain}$	Strain Tensor Components
EFA	Envelope Function Approximation
F	Helmholtz Free Energy
fca	Free Carrier Absorption
FGHM	Fourier Grid Hamiltonian Method
G	Gibbs Free Energy
GaAs	Gallium Arsenide
GaInAs	Gallium Indium Arsenide
H_{an}	Magnetic Anisotropy Field
Hg	Mercury
K	Kelvin

Γ	Confinement Factor
$\Gamma^{(2)}$	Nonlinear Overlap Integral
k_B	Boltzman Constant
M	Magnetization
MBE	Molecular Beam Epitaxy
MFGHM	Modified Fourier Grid Hamiltonian Method
Mn	Manganese
MOCVD	Metal-Organic Chemical Vapor Deposition
MOKE	Magneto-Optical Kerr Effect
MQW	Multiple Quantum Well
μ	Chemical Potential
NL	Nonlinear
NPDA	Non-Pump Depletion Approximation
p	Hole Density
P	Pressure
Se	Sellenium
SO	Spin-Orbit Band
T	Temperature
T_C	Curie Temperature
THz	Terahertz
V	Volume
VB	Valence Band

Ω	Rabi Frequency
Zn	Zinc

TABLE OF CONTENTS

Page

Page

LIST OF FIGURES

FIGURE Page

FIGURE Page

FIGURE Page

FIGURE Page

FIGURE Page

FIGURE Page

FIGURE Page

FIGURE Page

LIST OF TABLES

TABLE Page

1. INTRODUCTION*

1.1 Band Structure Based on the k • p Model for Bulk Semiconductors

Electronic states in semiconductors are best described by the series of quasi-continuous energy bands (for example, see Fig. 1-1) or in other words, by the dispersion relation between energy and momentum of a quasi-particle. The band structure contains information such as effective masses in high symmetry points or in band extrema and transition energies between interband critical points, band edge energies, the band gap, and so on.

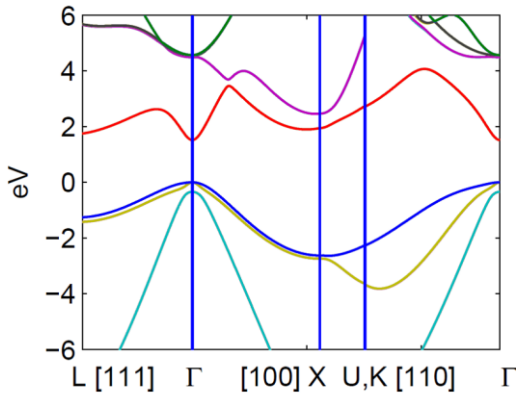

Fig. 1-1. GaAs band structure calculated by a 30-band k • p model.

This dissertation follows the style of Physical Review Letters.

*Part of this section is reprinted from "Above-bandgap magneto-optical Kerr effect in ferromagnetic $Ga_{1-x}Mn_xAs$" by C. Sun, J. Kono, Y.-H. Cho, A. K. Wojcik, A. Belyanin, and H. Munekata, (2011), Physical Review B, 83, 125206, Copyright © 2011 by American Physical Society (APS).

There are several methods to calculate the semiconductor band structure. The pseudo-potential method [1-5] uses the effective smooth potential for valence electrons based on the plane wave-basis wave functions instead of true potential, showing similarity with the nearly free electron model [6, 7]. The method can be further categorized into empirical and *ab-initio* (or first principle) pseudo-potential methods [8, 9] according to whether or not experimental data is used for determining pseudo-potential form factors, which is the Fourier transformation of pseudo-potential [10]. The empirical method often uses the band gap as an experimental input parameter. The local density approximation (LDA) [11-13] taking into account the many body effects such as exchange and correlation effects is an example of the *ab-initio* pseudo-potential method. On the other hand, the tight-binding method [14] assumes that electrons are tightly bound to nuclei sites. The method basically utilizes the overlap parameters for the interaction of electrons with nearby atoms. The k • p method [15, 16] provides another approach to the semiconductor band structure calculation. Compared to the empirical pseudo-potential method, it uses more experimental data such as all band edge energies and optically measured momentum matrix elements which represent band-to-band interactions.

Among the semiconductor band structure calculation methods, the k • p model is one of the most attractive since it provides convenient and efficient approach not only for bulk semiconductors but also for low dimensional semiconductor structures, particularly two-dimensional layered quantum well heterostructures [16].

The k • p method has a long history starting from Luttinger and Kohn's work based on the envelope function approximation back in 1955 [17]. It reduced finding the complicated valence band structure of semiconductors to a straightforward eigenvalue problem with a simple Hamiltonian matrix form based on the second order canonical transformation. The valence band structure consisted of 6 bands, i.e., the heavy hole (HH) band, the light hole (LH) band, and the spin-orbit (SO) band with Kramers double degeneracy of spin-up and spin-down states. The interactions between the valence band and the other bands were effectively taken into account by, so called, the Luttinger parameters [18]. Later, the conduction band (CB) structure has been added to the 6-band k • p model by Kane based on the perturbation theory [19], and the 8-band k • p model is now often referred to as the Kane model (see Fig. 1-2 for its band structure). It is accompanied by the modification of the valence band interaction parameters or the Luttinger parameters in the 6-valence band k • p model by subtracting the contribution of the conduction band (see APPENDIX A). Also, the difference from the 6-valence k • p Hamiltonian lies in the appearance of interband terms taking into account the interaction between the conduction band and the valence band. The explicit 8-band Hamiltonian matrix is given in APPENDIX A.

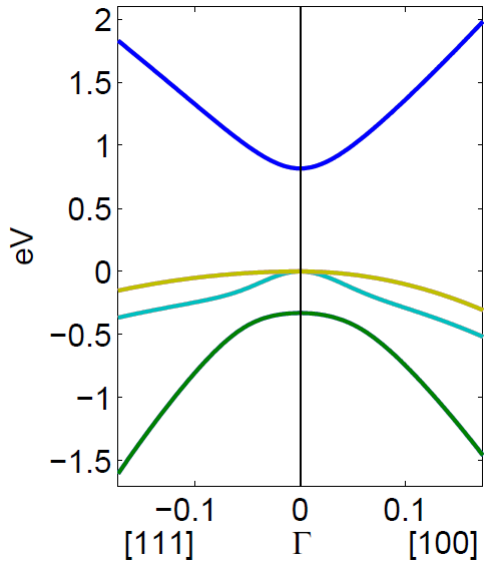

Fig. 1-2. GaAs band structure near Γ symmetry point, calculated by the 8-band k • p model. The band parameters in Ref. [20] are used.

However, the validity of this two-level k • p model, i.e., the 8-band k • p model is limited to the near vicinity of the Γ symmetry point, approximately up to the quasi-particle wave number k ~ 0.1 $Å^{-1}$ as one can see in Fig. 1-3. It does not correctly take into account the nonparabolic and anisotropic nature of semiconductor band structure at larger wave numbers. The validity of the model can be extended by explicitly including remote bands. Such k • p models are called the extended k • p models, differentiated from the 8-band k • p model. The 14-band [21-24], 15-band [25-28], 16-band [29], 20-band [30, 31], 24-band [32, 33], 30-band [34-37], and 34-band k • p models [38, 39] have been proposed. The development of the extended k • p method has been somewhat slow as compared to other band structure calculation methods because of the difficulty to find the *d*-level symmetry and its basis [34]. Before the emergence of the 30-band k • p model, they have been described by the Luttinger-like parameters [31-33]. In the 30-

band k • p model [34, 35], the symmetry was explicitly taken into account. The Luttinger parameters are not required anymore in the 30-band Hamiltonian matrix (the 15-band k • p model [25-28] also does not require them, but the spin degeneracy is neglected), and the valence band interactions with remote bands are fully taken into account by band-to-band momentum matrix elements and band edge energies. The 30-band k • p model provides an accurate semiconductor band structure which is valid over the whole first Brillouin zone. For most problems there is no need to go beyond the 30-band k • p model.

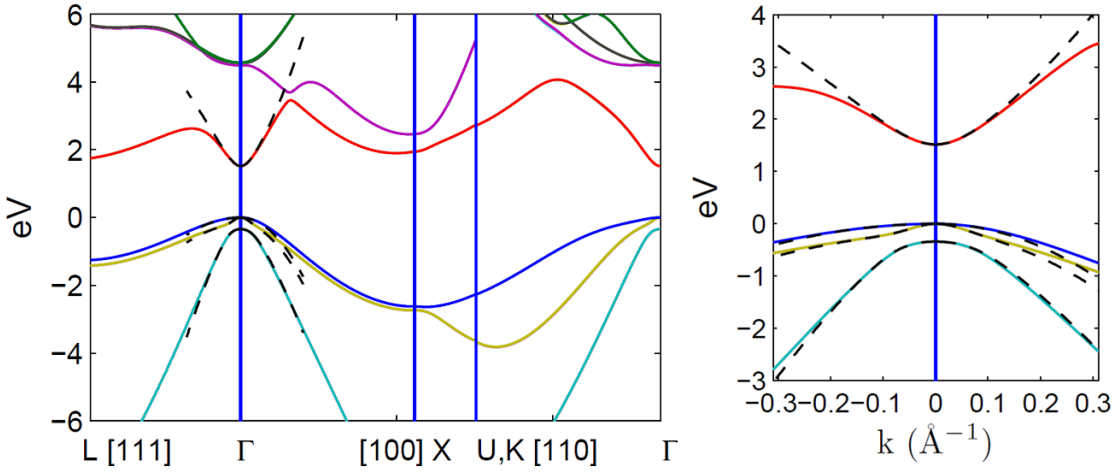

Fig. 1-3. The comparison between the band structure obtained by the 8-band (dashed) and the 30-band k • p models (solid) (a) over the whole Brillouin zone and (b) near the Γ symmetry point (magnified).

The 30-band k • p method is valid up to 5 eV above and 6 eV below the top of the valence band (see Fig. 1-3 and Ref. [34]), covering interband transitions of energies up to 11 eV. It has been successfully applied to calculating effective masses and Landé g

factors for the group IV and III-V semiconductors [36]. The general shortcomings of the method are also known: e.g., limited experimental data for remote bands and the numerical difficulty in ensuring the continuity between U and K symmetry points [34]. However, the GaAs band structure calculated by the 30-band method, which we will use, is quite accurate, and its results are adopted in the Landolt Börnstein database. The lack of inversion symmetry is taken into account through the matrix element between Γ_{6C} and Γ_{8V}/Γ_{7V} (here we follow the T_d double group notation throughout the paper). The 30-band k • p Hamiltonian matrix elements are obtained by the inner product of the 30-band basis orbitals [35] on (A.1). The energy level structures, band edge energies, and momentum matrix elements for GaAs in a 30-band model can be found in Ref. [34, 35].

1.2 The Dilute Magnetic Semiconductor, (Ga,Mn)As

The diluted magnetic semiconductor, $Ga_{1-x}Mn_xAs$, is obtained by heavy doping of the transition metal element, manganese (Mn), on GaAs. (Ga,Mn)As is an attractive material among III-V compound diluted magnetic semiconductors due to the mature growth technology and its possible coherent transition to new functional devices for spin-electronics [40]. Usual doping impurities in *n*- and *p*-type GaAs semiconductors are zinc (Zn) and selenium (Se) respectively [41]. Each of them has the atomic configuration of $[Ar]4s^23d^{10}$ and of $[Ar]4s^23d^{10}4p^4$. Accordingly, Zn and Se become an acceptor and a donor of an electron. Mn has the electronic configuration similar to Zn, but with a half

filled *d*-shell, i.e., $[Ar]4s^2 3d^5$. In terms of the Hund's rule [42], all five electrons have the same spin-up or spin-down configuration with the ground state term symbol of ${}^6S_{5/2}$. Therefore, the Mn impurities in GaMnAs not only play a role of acceptors while substituting Ga sites, but also show the possibility of the Mn spin-ordering mediated by the hole spin depending on their favored ferromagnetic or antiferromagnetic exchange couplings.

The ferromagnetic GaMnAs was first realized [43] back in 1996, seven years after the demonstration of the ferromagnetic InMnAs [44] along with the advent of the low temperature (LT) non-equilibrium MBE growth technology. After that, the material has been extensively explored in both experiment and theory. However, its ferromagnetic nature in the metallic regime is still controversial in (Ga,Mn)As with the high doping of Mn > 1%. In particular it is still debated whether the holes reside (i) in the valence band [45-48], (ii) in the impurity *d* band, or (iii) in the acceptor level above the valence band [49-53].

The early diluted magnetic semiconductors based on II-VI compounds (ZnSe, HgTe, and CdTe) back in 1970s through 1980s [54] did not reveal ferromagnetism. Nowadays due to the increased solubility of transition metal elements into II-VI semiconductors, allowed by the LT-MBE technology, one can achieve free carrier-mediated ferromagnetism in II-Mn-VI materials, but the ferromagnetic transition temperature is only ~2.5K [55], which is low as compared to the III-Mn-V materials (~190K for $Ga_{1-x}Mn_xAs$ with $x \geq 10\%$ [56]). It can be attributed to the fact that the doping impurity Mn has the same number of electrons as in the outer shell of column II

elements in the host semiconductors such as Zn, Hg, and Cd, which are substituted by Mn.

Not all Mn impurities in GaAs are substituted in Ga sites; some of them reside in interstitial sites [57, 58]. Since the ionized Mn^{2+} is regarded as neutral, the Mn impurities for such cases give out two electrons which effectively compensate two substitutional Mn ions (one hole for each substitutional Mn). However, such defects can be reduced by heating up samples after sample growth, and then such an annealing process increases the hole density. Consequently, the ferromagnetic transition temperature in the system also increases.

The (Ga,Mn)As samples which we will investigate were grown by the LT-MBE in Munekata's group in Tokyo Institute of Technology, and then they were experimentally characterized by interband magneto-optical (MO) Kerr (see section 1.3) spectroscopy and SQUID measurements in Kono's group at Rice University. We microscopically model the electronic states, Curie temperatures, magnetic anisotropies, and the dielectric responses of the samples adopting the valence band picture for metallic GaMnAs, as addressed above, based on the mean-field Zener model. Later, we compare with the experimental results.

Within the approach utilizing the k • p band model for electronic states of GaMnAs, the 8-band k • p model is usually adopted in many references [59-66]. It was applied to describe the response in the infrared spectral region near the Fermi level located inside the valence band in the metallic regime. Most recently such approach with

the antiferromagnetic *p-d* spin exchange coupling was used to explain experimentally observed magneto-optical effect in GaMnAs in a semi-quantitative way [66].

Our approach is similar but we use a 30-band k • p method instead of the effective band structure calculation based on the two-level model, which includes only Γ_{6C} (CB) and Γ_{8V}/ Γ_{7V} (VB). Since our primary interest is to reproduce the experimental magneto-optical Kerr spectra in the interband region up to ~ 3 eV, the band structure should be valid in this energy range. In that sense, the 8-band k • p method is not sufficient since it holds up to ~ 2 eV. The simulation of the magneto-optical Kerr spectra requires the calculation of the dielectric response or the conductivity of the material. It is significantly influenced by states with k-vectors higher than ~ 0.1 $Å^{-1}$, in which the two-level model starts to break down. Also, the model based on the 8-band k • p method has to include an adjustable static dielectric constant added by hand.

Furthermore, within the two-level k • p model, one needs to specify the Luttinger parameters in order to take into account any change of the interaction between the valence band and remote bands, which can occur due to adding additional interactions such as the spin exchange coupling in the ferromagnetic GaMnAs. On the other hand, it is automatically taken into account in the 30-band k • p model because the Luttinger parameters are not required in the Hamiltonian. Rather, they can be calculated especially upon adding the spin exchange interaction in GaMnAs. This is an important advantage of the 30-band k • p method as compared to the 8-band k • p method. Therefore, the modification of the valence band interaction with remote bands due to antiferromagnetic Mn-hole spin exchange coupling, the epitaxial strain of samples, and Coulomb

interaction effects in diluted magnetic semiconductors can be simultaneously taken into account within the 30-band k • p model.

At the same time, the 8-band k • p model is enough to deal with the magnetic properties of GaMnAs such as temperature-dependent magnetization and magnetic anisotropy based on the Zener model [67] which describes that the magnetic ordering of ion spins is mediated by free carrier spins, since they are associated with a very top portion of the valence band structure up to the quasi-Fermi level. The derivation of the *s,p-d* spin exchange interaction Hamiltonian for arbitrary magnetization directions in the 8-band k • p basis is presented in APPENDIX B.

1.3 Magneto-Optical Kerr Effect (MOKE)

The magneto-optical Kerr effect (MOKE) [68, 69] has long been a useful tool to investigate anisotropic dielectric materials that have non-zero net magnetization. When a linearly polarized electromagnetic field is incident on such samples, the polarization axis of the reflected light is rotated from the initial direction by an angle (the Kerr angle) that depends on the magnitude and direction of the magnetization. MOKE is originated from the refractive index difference between the right and left circular polarizations. In other words, it is attributed to the anisotropic dielectric response or conductivity of magnetic samples to the incident electromagnetic field.

1.4 Eigensolutions of Low-Dimensional Semiconductor Nanostructure

The development of semiconductor epitaxial growth technologies such as the molecular beam epitaxy (MBE) [70] and the metal-organic chemical vapor deposition (MOCVD) [71] has enabled fabrication of high-quality nanostructures in which layer thicknesses are controlled with one monolayer precision and electrons experience quantum confinement in one, two, or three dimensions [7]. The methods of calculating confined electron states, particularly in semiconductor layered heterostructures, are more complex than in bulk since the momentum component in the confinement direction (or the growth direction) becomes an operator, allowing only discrete eigen-energies in that direction instead of continuous ones. It requires solving coupled high-order partial differential equations depending on the number of bands included. This is usually handled by complicated numerical techniques as well as huge computing resources. Therefore, it is important to find a simple, accurate, and efficient methodology.

A number of methods in the real space [72-75] as well as in the momentum space [76-78] have been developed for calculating eigenstates in coupled low dimensional semiconductor heterostructures. However, many of them suffered from unphysical spurious solutions, and much effort have been spent on trying to remove these artifacts in various ways [77-86] even without being restricted[81, 86-88] to the k • p theory [15-17, 19]. However, it seems that there are no universal methods for removing spurious solutions until now. Many of them are for particular or simplified band models, or for

specific numerical models, and it is sometimes required to change the k • p Hamiltonian matrix or band parameters. The methods are not compatible to one another.

The spurious solutions are usually referred to as eigen solutions that are located in the middle of the band gap or that are fast oscillating envelope functions. It is heuristically known that multi-band Hamiltonians expanded up to the second order in terms of the confined momentum component generate such spurious solutions upon simultaneously seeking eigenstates in both the conduction and the valence bands. It occurs regardless of the simplicity of the k • p band models. Often, the origin is attributed to large *k* values outside the first Brillouin zone edge.

In the momentum space, the cut-off method [77] has been recently suggested for removing fast oscillating envelope-function-type spurious solutions in the plane wave expansion for confined states. It truncates the wave number vector at the cut-off value which is determined by the conduction band bending and is much smaller than the edge of the first Brillouin zone. The method is based on a miscalculated bulk 8-band structure, in which the contribution due to the explicit inclusion of the conduction band had not been subtracted from the valence band parameters. In other words, the Luttinger parameters were not modified properly. Consequently, the conduction band is bowed down into the band gap as the wave vector increases, which is obviously unphysical. The basic idea of introducing a cutoff to remove spurious solutions has been employed in other papers [81, 86].

The correct interface boundary condition, which connects wells and barriers at abrupt jump interfaces, in heterostructures is still being disputed [89-95]. Here, we

follow the ideology of the Fourier grid Hamiltonian (FGH) method [96], in which explicit boundary conditions are not necessary. Therefore, the ambiguity of the interface boundary condition on eigen solutions in semiconductor heterostructure problems can be ruled out within the EFA. Such approach to the heterostucture problem has been previously used in Ref. [76] in the momentum space instead of that in the real space as in our present work.

The FGH method [96] uses the forward and backward Fourier transformation, the variational method, and the fact that natural representations for the kinetic and the potential energies are in the momentum and the coordinate space, respectively. The resulting Hamiltonian for a bound system in a simple one-dimensional Schrödinger equation forms an $N \times N$ square matrix, in which N is equally discretized number of grid points in the coordinate space. The method has been further developed in various ways [97-102].

1.5 THz DFG in Quantum Well Heterostructures

As an application of the layered semiconductor heterostructures, we treat the optical device emitting terahertz (THz) radiation in quantum well heterostructures. The ability of the terahertz (THz; 1THz ~ 4 meV) radiation to penetrate non-destructively through dry opaque materials such as tissue, plastics, and fabrics, drives the development of THz sources for a wide range of potential applications, for example, in medical

imaging, gas sensing, security screening, and manufacturing [103]. For such practical applications, compact and efficient sources of for THz radiation operating at room temperature are in high demand. Among various kinds of THz radiation sources [104-123], the difference frequency generation (DFG) [124] based on intersubband resonant nonlinearity in multiple quantum well structures [104-107, 112-114] has attracted much interest. This process utilizes a large second-order optical susceptibility (at least 10^3 times larger than in conventional nonlinear crystals), originated from the broken parity of subband envelope functions in properly engineered multiple quantum well structures. The large optical nonlinearity opens the way to achieve high enough conversion efficiency even with moderate mid-infrared pump powers generated by mid-infrared quantum cascade laser sources.

The THz radiation at room temperature has been demonstrated particularly in the intracavity DFG scheme [105], in which the nonlinear mixing region was integrated within a dual-wavelength quantum cascade laser structure and in fact served as the active region for laser generation. However, due to a relatively small nonlinear overlap integral and the gain competition [125], the conversion efficiency to THz power is only $10^{-6}W^{-1}$ for the pump power of 1W. Also, the design of such devices is constrained by the requirement to have dual-wavelength mid-infrared laser generation in a monolithic device [126, 127].

Here, we consider an externally pumped THz DFG in semiconductor quantum well heterostructures, when two external pump fields at mid-infrared frequencies nearly resonant with intersubband transition energies E_{31} and E_{21} in Fig. 1-4, are incident on a

thick stack of multiple quantum wells designed to have a large optical nonlinearity for THz DFG. In this case, the nonlinear structure can be fully optimized for maximal nonlinear conversion efficiency without any negative effect on the mid-infrared laser performance. Also, since both pump laser radiation and THz-difference frequency mode can reside in a same thick nonlinear section, the nonlinear overlap integral can be approximately twenty times larger as compared to the intracavity THz DFG laser. Therefore, one can expect a much larger THz DFG output power in despite of the increased resonant absorption of pump fields due to the increased thickness of the nonlinear section.

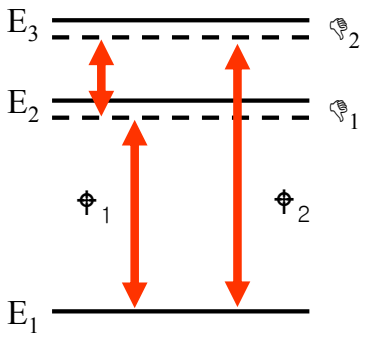

Fig. 1-4. A schematic picture of the energy levels (E_1, E_2, and E_3) and nearly resonant pump fields or the Rabi frequencies (Ω_1, Ω_2) with detunings (Δ_1, Δ_2) in the three-level medium for THz DFG. The difference ($\Omega_3 = \Omega_2 - \Omega_1$) between the two pump fields corresponds to the THz field.

The non-pump-depletion approximation in the coupled field theory [104] is usually adopted to explain the efficiency of the intracavity THz DFG in semiconductor quantum well structures since it provides simple physical interpretation for optimal

conditions of the efficient generation of DFG. According to the approximation, the THz intensity is given by Eq. (1.1): [128, 129]

$$I(\omega_3) = \frac{\omega_3^2}{8\varepsilon_0 c^3 n(\omega_1) n(\omega_2) n(\omega_3)} \left|\chi_{eff}^{(2)}\right|^2 \frac{I(\omega_1) I(\omega_2)}{S_{eff}} l_{eff} \tag{1.1}$$

where

$$l_{eff}^2 = \frac{e^{-\alpha_3 L} \left| e^{(\alpha_3/2 + i\Delta k)L} - 1 \right|^2}{(\Delta k)^2 + (\alpha_3/2)^2}$$

and L is the nonlinear section length, $\Delta k = k_1 + k_3 - k_2$ is the phase mismatch, and k_i and α_i are the propagation constant and the absorption coefficient for the i^{th} beam at frequency ω_i. When $\alpha_1, \alpha_2 \approx 0$ and $L >> 1/\alpha_3$, the coherence length l_{eff} is determined by the absorption at frequency ω_3, reducing to $l_{eff}^2 = 1/\left[(\Delta k)^2 + (\alpha_3/2)^2\right]$.

As follows from Eq. (1.1), for efficient generation of the THz-difference frequency field, the device needs to provide a large effective optical nonlinear susceptibility, a large overlap integral of pumps and DFG fields in the active region of a waveguide (or a small effective interaction area), high intensity of pump fields, phase matching, and low absorption. However, this approximation cannot be directly applied to the passive devices, where pump fields are significantly depleting due to resonant absorption and optical saturation effects which affect the electron distribution over subbands. Later we show that one can extend the analytic formula to include resonant absorption and saturation effects in an approximate way. However, significant deviation

from the analytic results still occurs at high pump powers or for longer waveguides. Therefore, a systematic and accurate numerical approach applicable for all input powers is required.

1.6 Overview of Dissertation

The dissertation deals with a III-V compound-base semiconductor bulk materials by the multi-band k • p methods and then moves to the two-dimensional system possessing the one-dimensional confinement in the momentum space together with applications for optical devices. Section 2 focuses on how to model and characterize the ferromagnetic GaMnAs materials by using the 30- and 8-band k • p method and the mean-field Zener model along with comparing with experimental Kerr spectroscopy and magnetization measurement results by SQUID. Section 3 plays a role of the bridge connecting bulk and low dimensional eigenvalue problems. Here we develop three different approaches for calculating the eigenstates in semiconductor heterostructures. First, starting from the ideology of the FGH method, we set up the formalism for the three approaches in the one-band model, and then they are extended to the general *n*-band **k • p** model based on the envelope function approximation. The differences between the approaches come from different approximations on the quasi-particle momentum integrals, which unavoidably appear due to the coordinate-dependent band parameters particularly in the heterostructure problems. These approximations have a

simple physical interpretation and their analysis helps us to pinpoint the origin of spurious solutions in the unified manner. In section 4, we use one of the new methods proposed in section 3, the delta function method, based on the one-band model with the nonparabolic correction. As applications, THz DFG optical devices are dealt by self-consistently taking into account the spatial charge distribution, electron distribution over excited subbands, and the propagation of coupled fields in waveguide structures of large nonlinear overlap integrals. In section 5, the summary and conclusions are provided.

2. ANISOTROPIC DIELECTRIC RESPONSE OF (Ga,Mn)As IN THE 30-BAND K • P MODEL[†]

2.1 $Ga_{1-x}Mn_xAs$ Sample Structure and Experimental Results

First we present the specific GaMnAs sample (grown by Munekata's group in Tokyo Institute of Technology) structure which we will study and the experimental results using MOKE and SQUID, obtained in Kono's group at Rice University. Experimentally obtained MOKE spectra will be compared with theoretical results in section 2.4.

The $Ga_{1-x}Mn_xAs$ samples are grown by low-temperature MBE, and its layer sequence is shown in Fig. 2-1. On a GaAs substrate, 1000 nm-thick GaInAs and 50 nm-thick GaMnAs layers are grown. There are three different kinds of samples depending on the nominal Mn fraction and post-growth annealing process, labeled as S-1, S-2, and S-3. The nominal Mn fractions of x = 0.01 and 0.024 are used in S-1 and S-2 respectively, and S-3 is the sample S-2 annealed at T = 190 ^{o}C in air for four hours. The samples show different ferromagnetic transition temperature T_C = 30, 45, and 70 K for S-1, S-2, and S-3 respectively, and temperature-dependent magnetization is measured by

[†]Part of this section is reprinted from "Above-bandgap magneto-optical Kerr effect in ferromagnetic $Ga_{1-x}Mn_xAs$" by C. Sun, J. Kono, Y.-H. Cho, A. K. Wojcik, A. Belyanin, and H. Munekata, (2011), Physical Review B, 83, 125206, Copyright © 2011 by American Physical Society (APS).

the remanent Kerr angle for S-2,-3 and by SQUID for S-1, as shown in Fig. 2-2. The ferromagnetic hysteresis for S-2 detected at 730 nm wavelength is shown in Fig. 2-3.

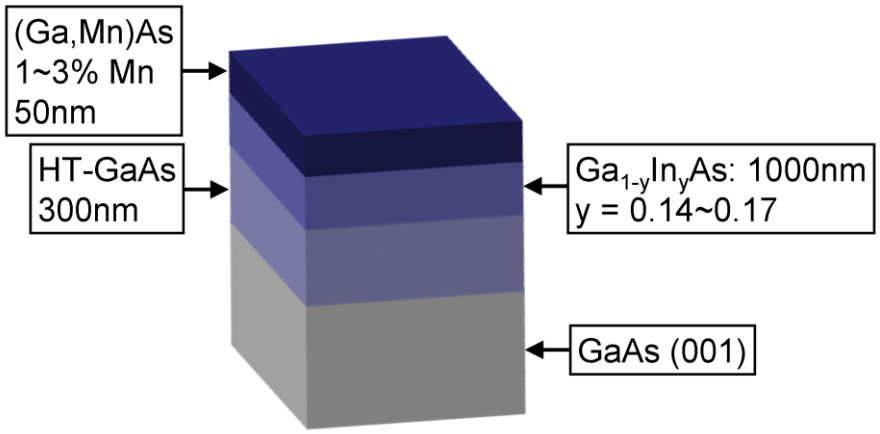

Fig. 2-1. GaMnAs sample structure grown by MBE at Munekata's group in Tokyo Institute of Technology.

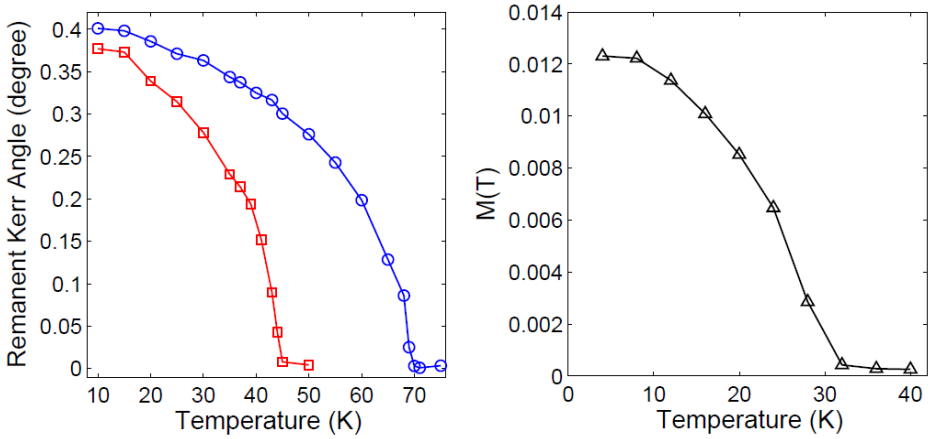

Fig. 2-2. Remanent Kerr angles (left) with 720nm wavelength of incident beam and magnetization (right) as functions of temperature are shown for three different GaMnAs samples; S-1 (triangle), S-2(square), and S-3 (circle). The right figure has been obtained by SQUID measurement. They indicate the temperature-dependent magnetization and Curie temperature (S-1: 30K, S-2: 45K, S-3: 70K) for the samples. The measurement data come from Kono's group at Rice University.

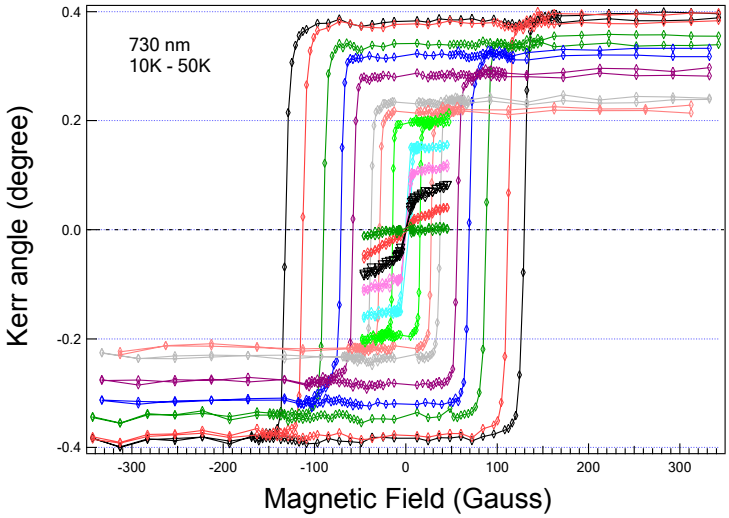

Fig. 2-3. Hysteresis loops measured at 730 nm for sample S-2 at multiple temperatures ranging from 10 K to 50 K under external magnetic field applied in the out-of-plane direction. The figure has been provided by Kono's group at Rice University.

2.2 Electronic States of GaMnAs Based on A 30-Band k • p Model

As discussed in section 1.2, our theoretical approach for investigating the samples shown in the section 2.1 is based on the k • p model and the mean-field Zener model [45, 46]. Our model-Hamiltonian is expressed as

$$H_T^{ij} = H_0^{ij} + H_{strain}^{ij} + H_{spin-ex}^{ij} \tag{2.1}$$

$$H_{strain}^{ij} = \sum_{\alpha,\beta} \langle i | D^{\alpha\beta} | j \rangle \varepsilon_{\alpha\beta}^{strain} \tag{2.2}$$

$$H_{spin-ex}^{ij} = \sum_{I}^{N_{Mn}} \left\langle i \left| J(\mathbf{r} - \mathbf{R}_I)\mathbf{S}_I \cdot \mathbf{s}_{sc} \right| j \right\rangle \approx J_{ij} N_{Mn} S_{Mn} \left\langle i \left| \hat{\mathbf{s}}_{sc} \right| j \right\rangle \tag{2.3}$$

where $\left\langle i \left| D^{\alpha\beta} \right| j \right\rangle = -\frac{\left(p_\alpha p_\beta\right)_{ij}}{m} + V_{ij}^{\alpha\beta}$. H_0^{ij} is a 30-band k • p matrix [35], H_{strain}^{ij} is the strain Hamiltonian matrix, $\varepsilon_{\alpha\beta}^{strain}$ is the strain tensor, in which all off-diagonal elements are zero; α and β are coordinates, $\left\langle i \left| D^{\alpha\beta} \right| j \right\rangle$ consists of the linear combination of the deformation potentials [15], m is the bare electron mass, and $H_{spin-ex}^{ij}$ describes the spin exchange interaction between the substitutional Mn magnetic impurity spins and the itinerant charge carrier spins in the host semiconductor in the mean-field approximation. The indices i and j run over all 30-band basis orbitals. The antiferromagnetic spin exchange constant J_{ij} is not zero only when the bases correspond to Γ_{6C}, $\Gamma_{8V,}$ and Γ_{7V}; J_{ij} = 54 $meV{\cdot}nm^3$ for Γ_{8V}/Γ_{7V}, J_{ij} = –9 $meV{\cdot}nm^3$ for Γ_{6C} [130, 131], and $N_{Mn} = 4 / a_{GaMnAs}^3$, where a_{GaMnAs} is the lattice constant of GaMnAs. The strain effects are included only for the bases Γ_{6C}, $\Gamma_{8V,}$ and Γ_{7V}. In this approximation, the Γ edges of Γ_{6C}, Γ_{8V}, and Γ_{7V} states are shifted by strain in the same trend as those in the 8-band model.

We qualitatively take into account many-body Coulomb interactions through the phenomenological band gap narrowing (BGN) [132]. The hole-occupied exchange spin split Γ_{8V} bands are assumed to be rigidly shifted by the total hole density dependence $a{\times}p^{1/3}$, where $a = 2.6{\times}10^{-8}$, hole density p is in cm^{-3}. The proportionality constant is compatible with that used in [66]. Several iterations are necessary to obtain self-consistent positions of the Γ_{8V} edges and the Fermi level. The disorder effect is also

phenomenologically described as broadening of interband optical transitions (~100 meV at half-width at half maximum (HWHM)) in the linear dielectric response function.

The thermal fluctuations of Mn spin ordering are estimated for the temperature T = 20 K, at which MOKE spectroscopy experiments are performed, by comparing the measured amplitudes of the remanent Kerr angle at 10 K and 20 K in Fig. 2-2. The effect of thermal fluctuations is included in the calculation of temperature-dependent dielectric tensors and Kerr angle spectra. The temperature dependence of other physical parameters, for example, the band gap, the lattice constant, the strain tensor, and the hole density are assumed to be negligible in this narrow temperature range.

We assume that our samples only have the epitaxial biaxial tensile strain (see Fig. 2-1), which breaks the crystallographic cubic symmetry due to the lattice mismatch between the GaMnAs epilayer and the relaxed GaInAs buffer layer. The same strain parameters as for GaAs [40] were used for the GaMnAs epilayer except for its lattice constant. Depending on the Mn (2 ~ 5%) and In (9.5%) contents, the strain tensor $\varepsilon_{ii}^{strain}$ ($i = x, y, z$) [15, 16] varies from 0.4 to 0.57% for the MnAs lattice constant 5.98 Å [5]. We assumed that our experimental post-growth procedure does not produce any additional significant strain. An example of the band structure calculated with the 30-band k • p method is shown in Fig. 2-4 for 5% Mn assuming a perpendicular magnetization (parallel to the sample growth direction). Contrary to the GaAs band structure shown in Fig. 1-1, the Kramers degeneracy is no longer valid, and spin-up and spin-down states are split. It indicates the spin polarization with different density of states for spin-up and spin-down of the valence band.

The conduction band and valence band splitting at Γ edge occur due to non-zero J_{sd} and J_{pd} respectively. Note that when $J_{pd} \neq 0$ and $J_{sd} = 0$, there is no spin splitting in the CB specifically at Γ edge. However, as k values increase, the spin splitting in CB rises because of the conduction and valence band mixing in the diagonalization process with the opposite sign of J_{sd}. Therefore, for $J_{pd} \neq 0$ and $J_{sd} \neq 0$, the spin splitting at $k \neq 0$ in the conduction band is more or less compensated with the splitting caused with $J_{pd} \neq 0$ and $J_{sd} = 0$, so that the first CB splitting becomes smaller as k increases as shown in Fig. 2-4(right). In the similar manner, the spin splitting in the valence band at larger k is affected by the non-zero J_{sd} exchange constant. But the effect is much smaller because of the relatively much smaller value of J_{sd} than J_{pd}.

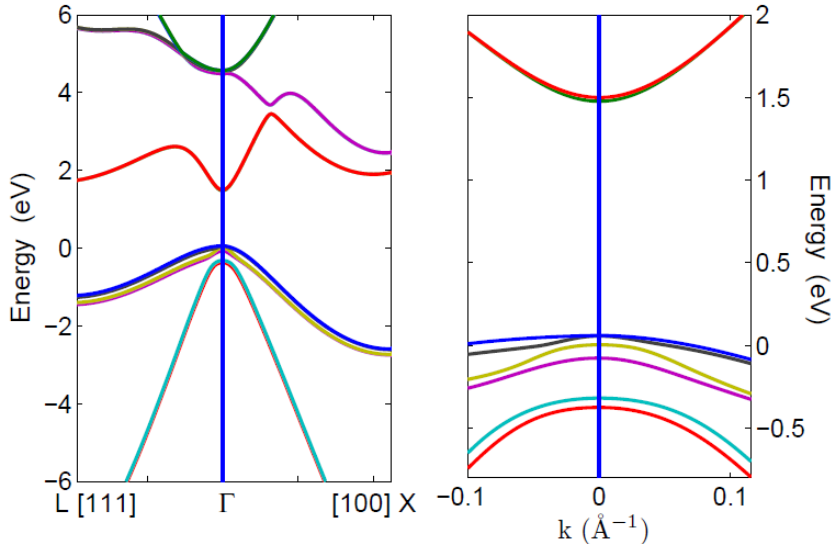

Fig. 2-4. Band structure of $Ga_{0.95}Mn_{0.05}As$, calculated with the 30-band k • p method described in the text, taking into account the Mn-hole spin exchange interaction as well as a biaxial tensile strain of $e_{xx}^{strain} = +0.4\%$. The right panel shows a magnified band structure near $k = 0$, in which split spin-up and spin-down states are clearly shown.

2.3 Temperature-Dependent Magnetization and Magnetic Anisotropy

Before proceeding with the calculation of the frequency-dependent dielectric tensor and magneto-optical Kerr angle spectra, we roughly estimate hole densities and Curie temperatures in our samples by calculating temperature-dependent magnetization. In addition, we determine the easy axis of magnetization with the estimated hole densities obtained for various Mn fractions. These will provide not only guidelines but also justification for subsequent Kerr angle calculations by the extended k • p method in the metallic regime in the interband range.

It is important to notice that the band structure is changed depending on magnetization direction as well as epitaxial strain. Figure 2-5 directly shows such effects on Fermi surfaces for 5% Mn and hole density $p = 3\times10^{20}\text{cm}^{-3}$ by varying the magnetization direction from in-plane [100] to out-of-plane [001] (parallel to the sample growth direction) and the strain from the compressive to the tensile. Two outer and inner surfaces correspond to spin-polarized HH and LH states respectively.

Since the ferromagnetism in GaMnAs comes from the ferromagnetic ordering of Mn spins mediated by antiferromagnetic coupling between hole spins and Mn spins based on the Zener model [67], the modeling of temperature-dependent magnetization requires that the hole free energy as a function of both hole density and magnetization is known prior to self-consistently dealing with the Brillouin function, B_s, obtained by the molecular-field approximation [133] in the canonical ensemble as can be seen in (2.4) under the absence of external magnetic fields.

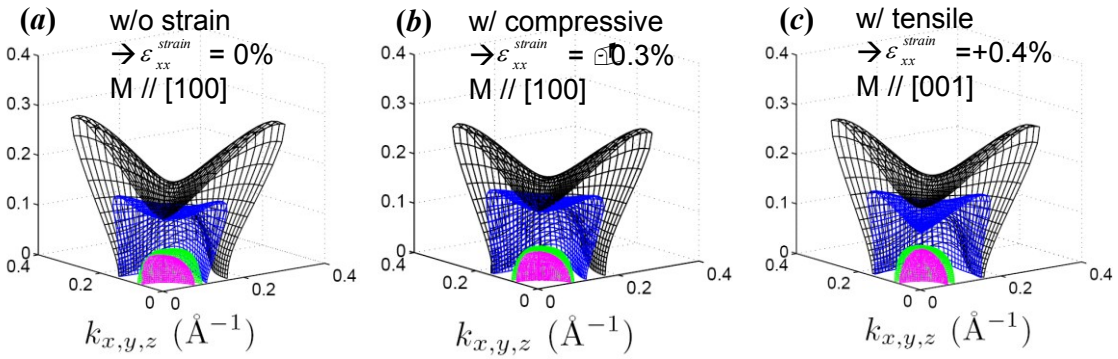

Fig. 2-5. Spin-polarized Fermi surfaces of GaMnAs for 5% Mn and hole density $p = 3\times10^{20}$cm^{-3} in the valence band with (*a*) in-plane direction [100] of magnetization *M* without strain, (*b*) in-plane direction [100] of *M* with strain tensor $\varepsilon_{xx}^{strain} = -0.3$ %, (*c*) out-of-plane magnetization *M* [001] with strain tensor $\varepsilon_{xx}^{strain} = 0.4$ %.

$$\langle S_z \rangle = SB_S\left(\frac{1}{(N_0 x k_B)T}\left(\frac{-\partial F[\langle S_z \rangle]}{\partial \langle S_z \rangle}\right)\right) \tag{2.4}$$

where

$$F(p,M) = \int_0^p dp'\,\varepsilon(p',M) \tag{2.5}$$

$$B_S(x) = \frac{2S+1}{2S}\coth\left(\frac{2S+1}{2}x\right) - \frac{1}{2S}\coth\left(\frac{x}{2}\right) \tag{2.6}$$

$$M = N_0 x g \mu_B \langle S_z \rangle \tag{2.7}$$

where $F(p,M)$ is Helmholtz hole free energy in the strongly degenerate limit (see APPENDIX C for derivation), p is hole density, M is the magnitude of magnetization, ε is the eigenvalue of the system for given p and M, $\langle S_z \rangle$ is Mn spin projection to [001] direction, x is Mn fraction, g is Landé g factor, and μ_B is Bohr magneton.

For a fixed Mn doping fraction, $F(p,M)$ can be calculated by integrating over a hole density in the graph, indicating the relation between Fermi levels and hole densities for each value of Mn spin orientation. Figure 2-6 shows the Fermi level dependence of hole density for fifty different Mn spin projections ranging from $\langle S_z \rangle$ = 0 to 5/2 with M//[001] and 4% Mn, and Fig. 2-7 shows the corresponding hole free energy behavior as a function of $\langle S_z \rangle$. Particularly near Curie temperature, i.e., $\langle S_z \rangle$ = 0, the hole free energy is parabolically increased as $\langle S_z \rangle$ is increased (or temperature is decreased).

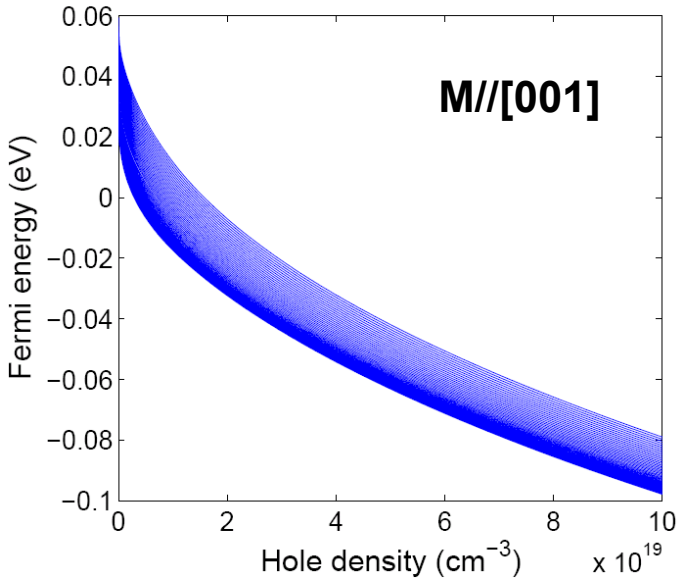

Fig. 2-6. Fermi energy as a function of hole density for fifty different Mn spin projections ranging from $\langle S_z \rangle$ = 0 to 5/2, assuming that *M*//[001] and 4% Mn.

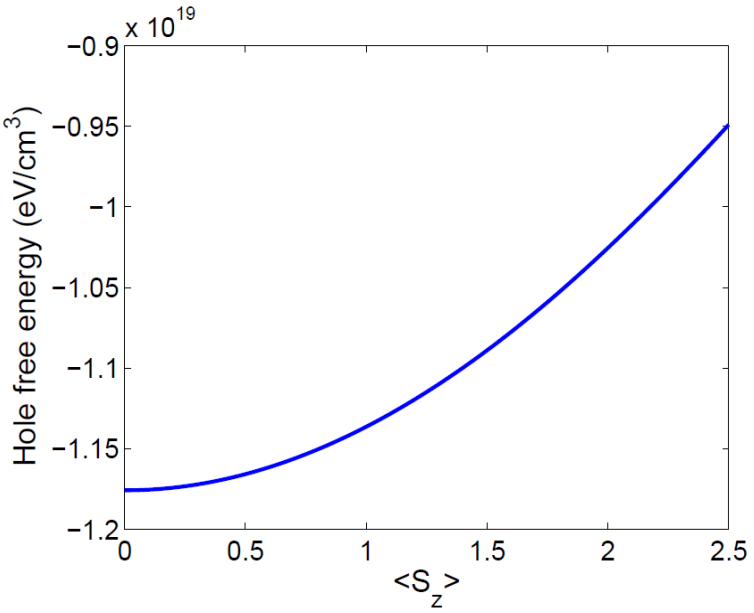

Fig. 2-7. Hole free energy as a function of $\langle S_z \rangle$ for *M*//[001], 4% Mn, and hole density $p = 10^{20}\text{cm}^{-3}$.

Now it is straightforward to obtain the gradient of $F[\langle S_z \rangle]$ in terms of $\langle S_z \rangle$ (see (2.4)), and the result is shown in Fig. 2-8. As consistent with Fig. 2-7, it shows the linear feature near $T_C = 0$. However, the gradient is nonlinear throughout $\langle S_z \rangle$. The extent of the nonlinearity indicates the interplay between the Fermi energy and *p-d* spin exchange coupling; the more linear gradient is, the smaller the Fermi energy.

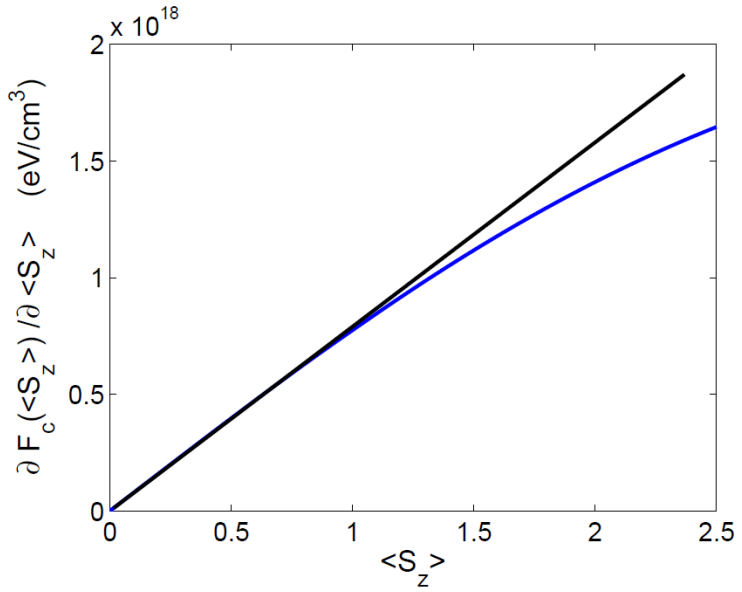

Fig. 2-8. Gradient of the hole free energy F as a function of $\langle S_z \rangle$ for 4% Mn and $p = 10^{20}\text{cm}^{-3}$ (Blue line). A linear reference line is indicated by black line.

The self-consistent solution for $\langle S_z \rangle$ with varying temperatures in (2.4) gives the temperature-dependent magnetization and Curie temperatures of GaMnAs. We tried various Mn fractions and hole densities (Table II-1), for which the calculated Curie temperatures are equal to the experimental ferromagnetic phase transition temperatures obtained from SQUID measurement and the saturated remanent Kerr angle as a function of temperature (Fig. 2-2). The calculated results for temperature dependent magnetization are shown in Fig. 2-9, and corresponding Mn fractions and hole densities are given in Table II-1. Here, we neglected the Fermi-liquid effect, which increases T_C [34], as well as the spin-wave excitations [35], which decrease T_C for a given Mn fraction and a hole density. We simulated the annealing effect [25], which increased T_C to 70 K for sample S-3, by increasing the hole density for each Mn fraction. Note that

generally not only the hole density increases, but also the lattice constant of GaMnAs is reduced upon annealing [26].

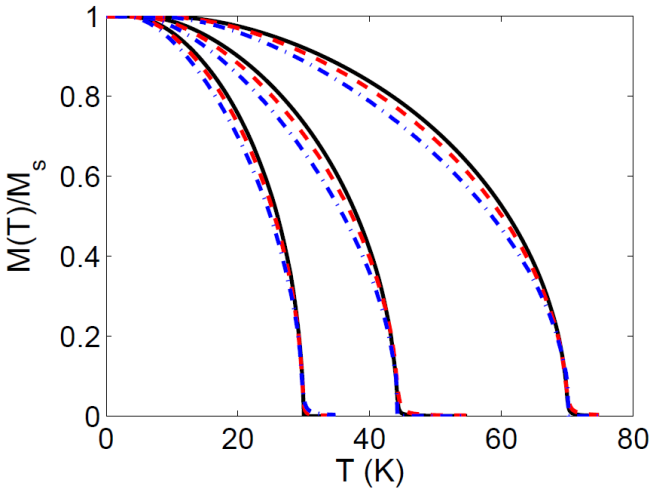

Fig. 2-9. Calculated temperature-dependent normalized magnetization based on the mean-field Zener model and the 8-band k • p method with different Mn fractions x = 0.03 (black solid line), 0.04 (red dashed line), 0.05 (blue dash-dotted line) for T_C = 45K (S-2) and 70K (annealed sample, S-3), and with x = 0.02 (black solid line), 0.03 (red dashed line), 0.04 (blue dash-dotted line) for T_C = 30K. The corresponding hole density for each case are summarized in Table II-1. The annealing effect was simply simulated by increasing hole densities for each Mn fraction. The results are all under tensile strain e_{xx}^{strain} = (0.57, 0.52, 0.46, 0.4) % for Mn fraction x = (0.02, 0.03, 0.04, 0.05).

The magneto-crystalline anisotropy, caused by the spin-orbit interaction, is attributed to the valence band holes since the total angular momentum of the local Mn moments is solely due to spins. The anisotropy gives certain preferred directions for the spins to be aligned in crystals, so that the easy direction of magnetization is determined. We estimate the anisotropy field, which is proportional to the difference of hole free energies normalized by magnetization in [001] and [100] directions [34], for different

nominal Mn fractions under tensile strain. The magnetic easy axis changes from [100] to [001] depending on the hole density as shown in Fig. 2-10 with the data set of Table II-1, in which for all hole densities the magnetic easy axis falls into the out-of-plane ([001]) because they are all larger than the critical hole density for each Mn fraction. The out-of-plane easy axis is further confirmed by the single domain like-behavior in the hysteresis loops of the measured remanent Kerr angles for the applied out-of-plane external magnetic field shown in Fig. 2-3.

Table II-1: Hole densities that are calculated with various Mn fractions based on the 6-band k • p method and the mean-field Zener model for the measured Curie temperatures of our samples.

T_C (K)	Mn (%)	Hole Density, *p* ($10^{20}cm^{-3}$)
45 (S-2)	3	2.35
	4	1.6
	5	1.2
70 (S-3)	3	5
	4	3.05
	5	2.2
30 (S-1)	2	2.4
	3	1.39
	4	0.97

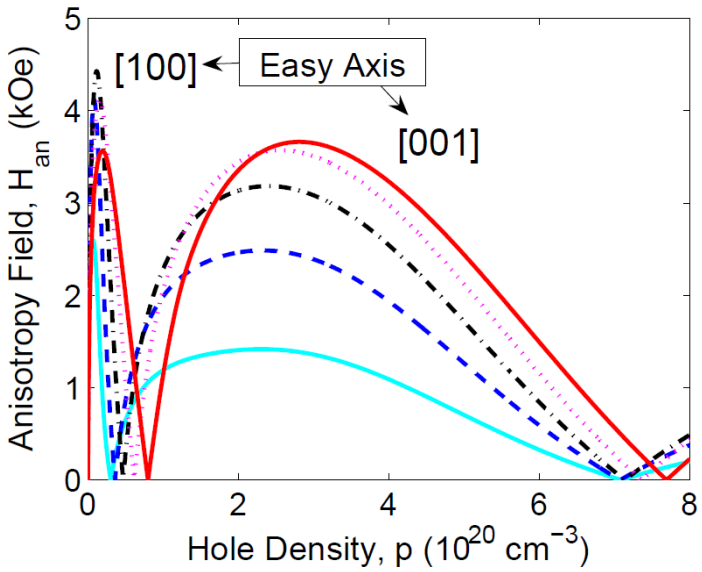

Fig. 2-10. Anisotropy field H_{an}, Calculated by the 8-band k • p model, as a function of hole density under tensile strain $\varepsilon_{xx}^{strain}$ = (0.63, 0.57, 0.52, 0.46, 0.4)% for Mn fraction x=(0.01, 0.02, 0.03, 0.04, 0.05) respectively. The magnetic easy axes of our samples are out-of plane ([001]) according to the pre-calculated hole densities that give the measured Curie temperatures, T_C = 30K, 45K, and 70K, as shown in Table II-1. Mn fraction x=0.01 (bottom solid), 0.02 (dashed), 0.03(dash-dotted), 0.04 (dotted), 0.05 (upper solid).

2.4 Frequency-Dependent Anisotropic Dielectric Tensor and Kerr Angle Spectra in the Interband Range

With the estimated hole densities and magnetic easy axis directions, calculations of the dielectric tensor are performed based on the linear response theory (or the Kubo formula [41-43]) shown in (2.8) for several different hole densities (shown in Table II-2

from the range of the hole densities and Mn fractions calculated for our samples in the previous section (see Table II-1)):

$$\varepsilon_{\alpha\beta}(\omega) = \delta_{\alpha\beta} + \frac{e^2\hbar^2}{m_0^2\varepsilon_0}\frac{1}{(2\pi)^3}\sum_{\substack{a,b\\a\neq b}}\iiint_{BZ} f_a\left[\frac{p_{ab}^{\alpha}p_{ba}^{\beta}}{(E_{ba}-i\hbar\gamma-\hbar\omega)(E_{ba})^2}+\frac{p_{ba}^{\alpha}p_{ab}^{\beta}}{(E_{ba}+i\hbar\gamma+\hbar\omega)(E_{ba})^2}\right]dk_x dk_y dk_z \tag{2.8}$$

where α and β denote coordinates, and a and b represent valence bands and conduction bands respectively. Only interband transitions are included in calculations; f_a is the Fermi-Dirac distribution and p_{ab}^{α} are components of the momentum matrix element (see APPENDIX D for the derivation). The integration is extended over the first Brillouin zone using full band structure calculated by the 30-band k • p method described in the section 1.1 and 2.2. An example of the calculated dielectric tensor is shown in Fig. 2-11.

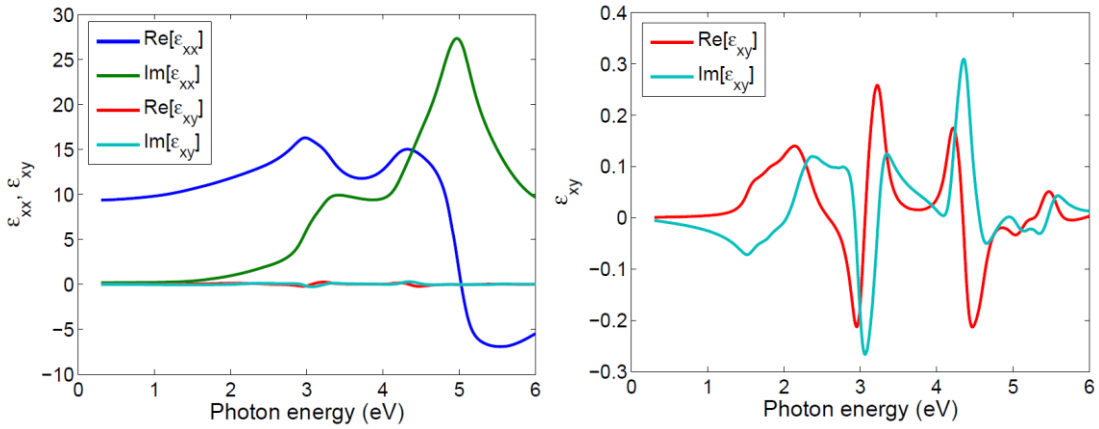

Fig. 2-11. Diagonal and off-diagonal dielectric tensor components are shown for 4% Mn, 0.5% tensile strain, T_C = 45K, and hole density p = 10^{20}cm^{-3}.

Note that the above approach is based on momentum matrix elements determined for a clean GaAs material. An important and still open question is whether and how one could modify the k • p matrix elements in a meaningful way to provide a more adequate description of heavily disordered systems.

Once frequency-dependent dielectric functions are obtained, Kerr angle spectra (θ_K vs. $\hbar\omega$) are straightforwardly simulated [68], taking into account multiple reflections [134, 135] in a thin GaMnAs layer and the buffer layer right below the GaMnAs layer. Note that GaInAs and air are isotropic materials, so that there is no right or left circular polarization dependence with $\varepsilon_{xy} = 0$. For the frequency dependent dielectric function of the GaInAs buffer layer, the linear interpolation of the experimental data [44] for GaAs and InAs are used.

The calculated Kerr angle results are shown in Fig. 2-12 (a,b,c) for the GaMnAs samples S-1, S-2, and S-3 respectively. Note that in Fig. 2-12 for a fixed Mn fraction, the Kerr angle peak magnitude decreases with increasing hole density. This happens because at these densities the Fermi level is already located below the lowest band edge of the spin-split Γ_{8V}. With increasing hole density, the Fermi level is shifted further downward, which reduces the number of states that contribute to interband optical transitions. On the other hand, if the Fermi level were initially positioned in the middle of the spin-split Γ_{8V}, increasing the hole density would not necessarily decrease the Kerr angle amplitude.

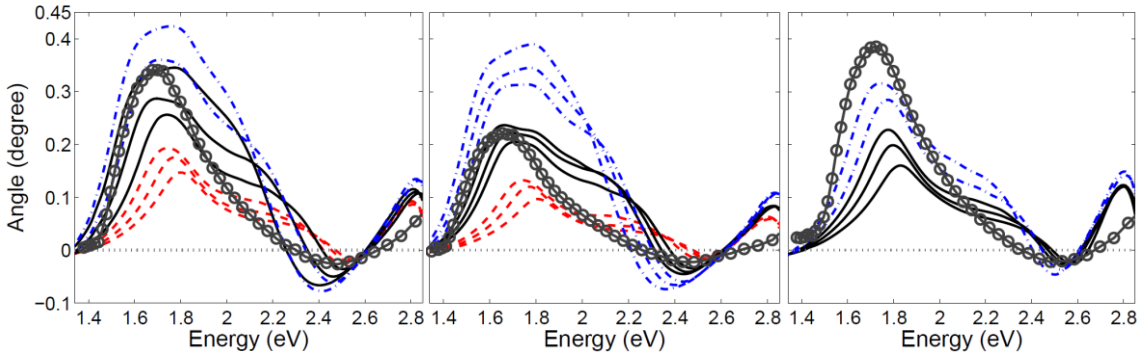

Fig. 2-12. Calculated frequency-dependent magneto-optical Kerr angles under the tensile strain by the 30-band k • p method in the interband transition range for GaMnAs samples (*a*) S-2, (*b*) S-1, and (*c*) S-3. For each case, hole densities and Mn fractions are changed as summarized in Table II-2. Hole densities were chosen with the range of $\sim\pm5\times10^{19}$cm^{-3} from the estimated hole densities in Table II-1; (*a*) Mn fractions x=0.03(red dashed), 0.04(black solid), 0.05(blue dash-dotted); (b) x=0.02(red dashed), 0.03(black solid), 0.04(blue dash-dotted); (c) x =0.04(black solid), 0.05(blue dash-dotted). For each Mn fraction, corresponding hole densities are smaller from the top graph. Here GaMnAs epilayer thickness is assumed to be 70nm. Circles indicate experimentally measured Kerr spectra provided by Kono's group in Rice University.

Table II-2: Mn fractions and corresponding hole densities chosen for the dielectric function and Kerr angle calculations (Fig. 2-12) by the 30-band k • p method. Best matching conditions with experimental Kerr angle measurement are underlined.

T_C (K)	Mn (%)	p (10^{20}cm^{-3})	T_C (K)	Mn (%)	p (10^{20}cm^{-3})	T_C (K)	Mn (%)	p (10^{20}cm^{-3})
45 (S-2)	3 (red)	2 2.5 3	30 (S-1)	2 (red)	2 2.5 3	70 (S-3)	4 (black)	2.5 3 3.5
	4 (black)	**1** 1.5 2		3 (black)	1.2 **1.4** 1.6			
	5 (blue)	1 **1.5**		4 (blue)	0.8 1 2.5		5 (blue)	**2** 2.5

Kerr angle calculation results for 4% Mn give the best agreement with the experimental MOKE spectra of S-2, as shown in Fig. 2-12(a). The first positive peak that can be attributed to the interband transitions around the E_0 critical point is red-shifted due to phenomenological band gap narrowing of 0.121 and 0.138 eV, respectively, for each case. Note that the above Mn fractions are 1.5-2 times larger than the experimental nominal value, 2.4% for S-2. We discuss it in the following section.

For sample S-1, the calculated result for Kerr angles is closest to the experimental MOKE spectra for 3% Mn, as shown in Fig. 2-12(b) and Table II-2. This Mn fraction is also larger than the experimental value of 1.5% for sample S-1.

In Table II-1, the hole densities that are predicted for T_C = 70 K based on the 8-band k • p model are over-estimated since at large hole densities the hole free energy calculated with the 8-band k • p model becomes non-negligibly smaller than the one calculated with the full-band model. This originates from the difference between the valence band structures calculated with these two models at large k. Therefore, it is expected that the 30-band structure calculation yields the hole densities lower than those listed in Table II-1. Also since with 4% or 5% Mn fraction, the Kerr angle calculation better agrees with the experimental Kerr spectra for T_C = 45K (S-2) as shown in Fig. 2-12(a), cases with 4% and 5% Mn fractions are only performed for the annealed case of T_C = 70K. The results are shown in Fig. 2-12(c), and their corresponding hole densities are listed in Table II-2.

2.5 Discussion

Our calculated MOKE spectra of ferromagnetic GaMnAs samples in the interband transition range reveal a general pattern of a large-amplitude positive peak around 1.4-2.3 eV followed by negative and positive peaks with lower-amplitudes at higher photon energies, similar to the experimental data. At the same time, the quantitative spectral shapes and the positions of the peaks sensitively depend on the amount of substitutional Mn, the hole density, and the layer thickness. We determined the range of Mn fractions and corresponding hole densities for which the calculated Curie temperatures were equal to the experimentally measured ferromagnetic transition temperatures. Then the parameters from this range providing the best fit to the measured MOKE spectra were found. The resulting Mn fractions turned out to be larger than the experimental nominal doping values for all samples. If we assume that the experimental Mn concentrations are quite accurate, this result could indicate that antiferromagnetic *p-d* exchange coupling strengths are 1.5-2 times stronger than the value of J_{ij} adopted in the calculations. This is because, in the mean-field approximation, the exchange coupling energy is linearly proportional to the nominal Mn fraction as well as J_{ij}, as shown in Eq. (2.3).

Unlike magnetic circular dichroism, which has a clear physical interpretation as the difference of absorption coefficients between the σ- and σ+ polarizations, it is difficult to extract a single physical parameter that determines the characteristics of the Kerr angle spectra in a thin layer limit [18] since the contribution of the GaMnAs layer

thickness, diagonal and off-diagonal components of dielectric functions, and the dielectric function of the buffer layer should be explicitly considered. However, the first positive peak can still be attributed to the interband transitions around the E_0 critical point. The position of this peak and those of subsequent peaks are affected by the layer thickness. Figure 2-13 shows a set of calculated MOKE spectra for a fixed Mn fraction (4%) and hole density ($p = 1\times10^{20}$cm^{-3}) but different thicknesses of the GaMnAs epilayer. The Kerr angle peaks red-shift as the thickness increases. The best match to the spectrum of sample S-2 is obtained when the layer thickness is about 70nm, which is somewhat higher than our nominal value of 50nm.

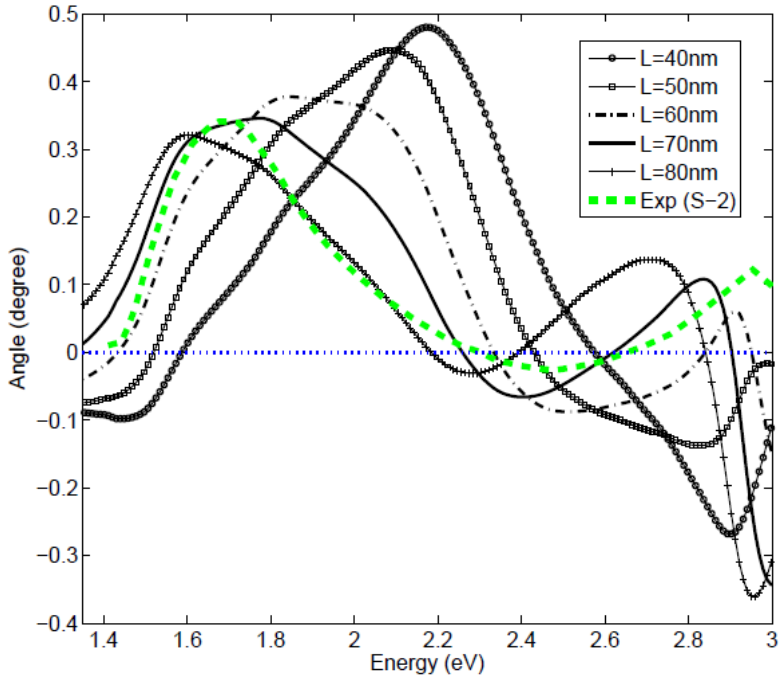

Fig. 2-13. Calculated MOKE spectra for ferromagnetic GaMnAs with different layer thicknesses for 4% Mn fraction and hole density of 1×10^{20} cm^{-3}. The dotted (green) line shows the experimental spectrum for sample S-2.

For the annealed sample (S-3) the main peak in the measured MOKE spectrum shows a slightly increased amplitude as well as a slight blue-shift as compared to that before annealing (S-2). If we assume that the only effect of annealing is an increased hole density for a given Mn fraction, our simulations predict an opposite trend: a decrease in the amplitude of the Kerr angle peak with increasing hole density. Within the mean field approximation, the observed effect of annealing indicates that the annealing also leads to an increase in the exchange interaction energy through an increase in the Mn fraction or/and J_{ij}.

3. NEW METHODOLOGIES FOR FINDING EIGEN SOLUTIONS IN LOW DIMENSIONAL SEMICONDUCTOR NANOSTRUCTURES

3.1 New Real Space Approaches to Heterostructure Hamiltonian in One Band Model

3.1.1 A 2-D Heterostructure Hamiltonian Based on the Fourier Grid Hamiltonian Method

A simple empirical way to determine band offsets at a heterojunction between two different bulk semiconductors is to assume that the vacuum energy levels for these materials coincide and the valence band position is the same as in the bulk materials. This determines the valence band (VB) offset between the two materials at the top of the VB. InSb provides the zero reference of the VB offset, from which those for the other materials are determined [20]. The resulting band edge profiles in a heterojunction look step-function-like and therefore acquire the coordinate dependence. This is true not only for the band edges but also for other band parameters such as the Luttinger parameters, the Kane parameter, and strain parameters because band parameters used in heterostructure problems are assumed to be the same as the parameters of bulk materials in the EFA.

In the parabolic one band model, the band edge effective masses for quasi-particles also show abrupt jumps and coordinate-dependence at heterojunctions.

Therefore, in the Schrödinger equation for the one band model (Eq. (3.1)), one needs to decide how to write the kinetic energy term, which contains the inverse coordinate-dependent mass and the momentum which becomes a differential operator in the coordinate representation. The usual choice is to write the kinetic term in the symmetrized way that keeps the Hamiltonian Hermitian[136]:

$$\hat{H} = \frac{\hbar^2 \hat{k}_z^2}{2m^*(\hat{z})} + V(\hat{z}) = \hat{k}B(\hat{z})\hat{k} + V(\hat{z}) \tag{3.1}$$

where the confinement direction is assumed to be the z-direction, $B(\hat{z}) = \hbar^2 / 2m^*(\hat{z})$, $\hbar\hat{k}_z$ is the momentum operator, the notation for $\hat{k}_z$ is simplified to $\hat{k}$, and $V(\hat{z})$ is a quantum well potential in a single band,.

We first adopt the machinery of the Fourier grid Hamiltonian (FGH) method[96] to derive the Hamiltonian for semiconductor heterostructures. In (3.1), $B(\hat{z})$ and $V(\hat{z})$ are represented in the coordinate basis, and $\hat{k}_z$ in the momentum basis. These are most natural choices because of the immediate diagonalization of eigenvalues in each representation. Then, (3.1) can be expressed as

$$\langle z|\hat{H}|z'\rangle = \langle z|\hat{k}B(\hat{z})\hat{k} + V(\hat{z})|z'\rangle \tag{3.2}$$

$$= \int_{-\infty}^{\infty}\int_{-\infty}^{\infty}\int_{-\infty}^{\infty}\int_{-\infty}^{\infty}\int_{-\infty}^{\infty}\langle z|k\rangle\langle k|\hat{k}|k'\rangle\langle k'|z''\rangle\langle z''|B(\hat{z})|z'''\rangle\langle z'''|k''\rangle\langle k''|\hat{k}|k'''\rangle\langle k'''|z'\rangle dk dk' dk'' dk''' dz'' dz''' + \langle z|V(\hat{z})|z'\rangle \tag{3.3}$$

where the completeness relations for coordinate and momentum bases were used, i.e.,

$$\hat{I}_z = \int_{-\infty}^{\infty}|z\rangle\langle z|dz \ , \ \hat{I}_k = \int_{-\infty}^{\infty}|k\rangle\langle k|dk$$

Assuming the plane wave basis when projecting the momentum space on the coordinate space

$$\langle z | k \rangle = \frac{1}{\sqrt{2\pi}} e^{ikz}$$

and using the orthogonality of the basis along with eigenvalue equations such that

$$\hat{k}|k'\rangle = k'|k'\rangle \ , \ B(\hat{z})|z'''\rangle = B(z''')|z'''\rangle$$

(3.3) can be simplified to (3.4) leaving only three integrals in the kinetic energy term:

$$\langle z|\hat{H}|z'\rangle = \frac{1}{(2\pi)^2}\int_{-\infty}^{\infty}\int_{-\infty}^{\infty}\int_{-\infty}^{\infty} ke^{ik(z-z'')}B(z'')e^{ik'(z''-z')}k'\,dkdk'\,dz'' + V(z)\delta(z-z') \qquad (3.4)$$

Note that as a result of the coordinate dependent band parameter, i.e., $B(z)$, integrations in terms of two different quasi-particle momenta appear as the symmetric form in (3.4). Since the bases are spanning over the coordinates of a whole quantum well system, the explicit treatment of boundary conditions are not required. Instead they are implicitly included and automatically fulfilled. This is also true when the band parameter is not dependent of coordinates. Starting from (3.4), three different approaches depending on approximations of integrals in (3.4) will be shown through this section and section 3.1.2 ~ 3.1.3.

For the numerical treatment in the FGH method, the integration in Eq. (4) is straightforwardly done by the discretization with an equal grid length, $\Delta z = L/(N-1)$, which has the Fourier reciprocal relation with momentum as $\Delta k = 2\pi/(N\Delta z)$. Here, L and N are the total system length in the coordinate space and the total odd number of grid points, respectively. Then, we change integral variables and coordinate bases to

discrete forms in (3.4) such that $k = \alpha\Delta k$, $k' = \beta\Delta k$, $z = (p-1)\Delta z$, $z' = (q-1)\Delta z$, and $z'' = (s-1)\Delta z$, where $-m \le \alpha, \beta \le m$ (=(*N-1*)/2), and p, q, and s are 1, 2, 3,…, N. Integrals are now replaced by summations. Then, the kinetic energy term in (3.4) becomes the following expression:

$$\frac{1}{(2\pi)^2}\sum_{s=1}^{N}\left[B((s-1)\Delta z)\Delta z\sum_{\beta=-m}^{m}(\beta\Delta k)(\Delta k)e^{i(\beta\Delta k)(p-s)\Delta z}\sum_{\alpha=-m}^{m}e^{i(\alpha\Delta k)(s-q)\Delta z}(\alpha\Delta k)(\Delta k)\right]$$

$$=\frac{1}{\Delta z}\frac{4(\Delta k)^2}{N^2}\sum_{s=1}^{N}\left[B((s-1)\Delta z)\left(\sum_{\beta=1}^{m}\beta\cos\left[\frac{2\pi\beta(p-s)}{N}\right]\right)\left(\sum_{\alpha=1}^{m}\alpha\cos\left[\frac{2\pi\alpha(s-q)}{N}\right]\right)\right] \qquad (3.5)$$

where we have used that $\alpha, \beta = 0$ do not contribute to the summations. The potential energy term in (3.4) can be discretized in the same way as the kinetic energy term, and resulting equation can be written as

$$V((p-1)\Delta z)\delta((p-q)\Delta z)$$

$$\approx \frac{1}{\Delta z}V((p-1)\Delta z)\delta_{pq} \qquad (3.6)$$

where the following property of the delta function[137] was used:

$$\delta(\Delta z(p-q)) = \frac{1}{\Delta z}\delta(p-q) \approx \frac{1}{\Delta z}\delta_{pq}, \quad (\Delta z > 0) \qquad (3.7)$$

By putting (3.5) and (3.6) together and applying the variational method,[96] which cancels the 1/Δz factor in (3.5) and (3.6), we finally obtain the Hamiltonian matrix elements for quantum well heterostructures in the one band model based on the Fourier grid Hamiltonian method:

$$H(p,q)=\frac{4(\Delta k)^2}{N^2}\sum_{s=1}^{N}\left[B((s-1)\Delta z)\left(\sum_{\beta=1}^{m}\beta\cos\left[\frac{2\pi\beta(p-s)}{N}\right]\right)\left(\sum_{\alpha=1}^{m}\alpha\cos\left[\frac{2\pi\alpha(s-q)}{N}\right]\right)\right]+V((p-1)\Delta z)\delta_{pq} \tag{3.8}$$

Note that the Hamiltonian matrix is real and symmetric upon exchanging grid indices p and q, ensuring that it is Hermitian. The two summations in terms of α and β are independent of each other. However, the summation over s is connected with the other summations.

Using a standard eigenvalue equation solver, the eigenvalues (E_n) (or subband energy levels) and the eigenfunctions (f_n) (or envelope functions) are readily obtained by solving $Hf_n = E_n f_n$. But it is necessary for each eigenfunction to be normalized by fulfilling the following condition:

$$\Delta z\sum_{m=1}^{N} f_n((m-1)\Delta z)=1$$

3.1.2 Modified Formalism with Improved Accuracy

In the previous section, the final form of a heterostructure Hamiltonian (3.8) in the one band model has been obtained by directly discretizing (3.4), following the original strategy of the Fourier grid Hamiltonian method. All three integrals in (3.4) have been approximated by the discretization, which inevitably generates errors in determining the subband energy levels. In this section we show how the method can be improved by the analytical evaluation of the quasi-particle momentum integrals. It is possible since the

infinite integral range is practically cut off to be finite, determined by the Fourier reciprocal relation as was done in (3.5).

Therefore, in (3.4) the integral over k can be rewritten as

$$\int_{-k_m}^{k_m} k e^{ik(z-z")}\, dk = -2ik_m \frac{\partial}{\partial z}\left[\text{sinc}\left(k_m(z-z")\right)\right] \tag{3.9}$$

$$= \begin{cases} -2i\left[\dfrac{k_m \cos\left(k_m(z-z")\right)}{(z-z")} - \dfrac{\sin\left(k_m(z-z")\right)}{(z-z")^2}\right] & when\ z \neq z'' \\ 0 & when\ z = z'' \end{cases} \tag{3.10}$$

Here *sinc* is an unnormalized sinc function, $k_m = m\Delta k$, where *m* and *Δk* are defined as in (3.5). The integral over *k'* can be calculated similarly. Consequently, the kinetic energy part of (3.4) becomes

$$\frac{4}{(2\pi)^2}\int_0^L B(z")\left[\frac{k_m \cos\left(k_m(z-z")\right)}{(z-z")} - \frac{\sin\left(k_m(z-z")\right)}{(z-z")^2}\right]\left[\frac{k_m \cos\left(k_m(z'-z")\right)}{(z'-z")} - \frac{\sin\left(k_m(z'-z")\right)}{(z'-z")^2}\right]dz" \tag{3.11}$$

where $z \neq z"$ and $z' \neq z"$. Now only a single integral exists as compared to (3.4). By the discretization as in (3.5) and the variational method used in (3.8), the modified heterostructure Hamiltonian of (3.8) with improved accuracy is given by

$$H(p,q) = \frac{4}{(2\pi)^2}(\Delta z)^2 \sum_{s=1}^{N}\left[B\left((s-1)\Delta z\right)\left(\frac{k_m \cos\left(\frac{2\pi}{N}m(p-s)\right)}{(p-s)\Delta z} - \frac{\sin\left(\frac{2\pi}{N}m(p-s)\right)}{(p-s)^2(\Delta z)^2}\right)\right.$$

$$\left.\times\left(\frac{k_m \cos\left(\frac{2\pi}{N}m(q-s)\right)}{(q-s)\Delta z} - \frac{\sin\left(\frac{2\pi}{N}m(q-s)\right)}{(q-s)^2(\Delta z)^2}\right)\right] + V\left((p-1)\Delta z\right)\delta_{pq} \tag{3.12}$$

where the notations are same as above, and the Hamiltonian matrix is real and Hermitian again. Note that when $p = s$ or $q = s$, the kinetic energy part in (3.12) is zero.

3.1.3 Delta Function Method (DFM)

In this section we rewrite Eq. (3.4) in terms of the delta functions in the real space and then discretize them. Starting from (3.4), in which no approximation has been used, the exponential terms are expressed as

$$ke^{ik(z-z")} = \begin{cases} -i\dfrac{\partial}{\partial z}e^{ik(z-z")} & (3.13) \\ i\dfrac{\partial}{\partial z"}e^{ik(z-z")} & (3.14) \end{cases} \qquad k'e^{ik'(z"-z')} = \begin{cases} i\dfrac{\partial}{\partial z'}e^{ik'(z"-z')} & (3.15) \\ -i\dfrac{\partial}{\partial z"}e^{ik'(z"-z')} & (3.16) \end{cases}$$

Here, one might think that there could be several choices to replace the exponential terms since there are two possible derivatives for each. However, it is not true for the following reasons. First of all, we need to make sure that the Hamiltonian is still symmetric upon exchanging z and z' in the final form. Second, we like to eliminate the integral with respect to z'' in (3.4), eventually removing all integrals. The way to do this is that each of the exponential terms should contain a z'' derivative only once. The only possible choice which fulfills the above two conditions is to combine [(3.13) and (3.16)] and [(3.14) and (3.15)]. This is uniquely determined with excluding any other combinations. This becomes more transparent through the following derivation.

Using the above combinations, Eq. (3.4) can be now rewritten as

$$\left\langle z\left|\hat{H}\right|z'\right\rangle = \frac{-1}{2(2\pi)^2}\int_{-\infty}^{\infty}\left[\left(\frac{\partial}{\partial z}\int_{-\infty}^{\infty}e^{ik(z-z")}dk\right)B(z")\left(\frac{\partial}{\partial z"}\int_{-\infty}^{\infty}e^{ik'(z"-z')}dk'\right)\right.$$

$$\left.+\left(\frac{\partial}{\partial z"}\int_{-\infty}^{\infty}e^{ik(z-z")}dk\right)B(z")\left(\frac{\partial}{\partial z'}\int_{-\infty}^{\infty}e^{ik'(z"-z')}dk'\right)\right]dz"+V(z)\delta(z-z') \qquad (3.17)$$

Note that the derivatives do not act on *B* (*z"*). The integrals in terms of quasi-particle momenta *k* and *k'* can be exactly evaluated using the integral form of the delta function,[137] i.e.,

$$\delta(z-z') = \frac{1}{2\pi}\int_{-\infty}^{\infty}e^{ik(z-z')}dk$$

Then, the kinetic energy term in (3.17) becomes

$$\frac{-1}{2}\int_{-\infty}^{\infty}\left[\left(\frac{\partial}{\partial z}\delta(z-z")\right)\left(\frac{\partial}{\partial z"}\delta(z"-z')\right)B(z")+\left(\frac{\partial}{\partial z"}\delta(z-z")\right)\left(\frac{\partial}{\partial z'}\delta(z"-z')\right)B(z")\right]dz" \qquad (3.18)$$

Using the relation for the derivative of the delta function,

$$-\frac{\partial f(z')}{\partial z'} = \int_{-\infty}^{\infty}\frac{\partial\delta(z-z')}{\partial z}f(z)dz$$

the formula (3.18) can be further simplified by explicitly evaluating the integral with respect to *z"*, i.e.,

$$\frac{1}{2}\left[\frac{\partial}{\partial z'}\left[\left(\frac{\partial}{\partial z}\delta(z-z')\right)B(z')\right]+\frac{\partial}{\partial z}\left[\left(\frac{\partial}{\partial z'}\delta(z-z')\right)B(z)\right]\right] \qquad (3.19)$$

By putting the kinetic energy together with the potential energy term, (3.17) can be now read as

$$\left\langle z\left|H\right|z'\right\rangle = \frac{1}{2}\left[\frac{\partial}{\partial z'}\left[\left(\frac{\partial}{\partial z}\delta(z-z')\right)B(z')\right]+\frac{\partial}{\partial z}\left[\left(\frac{\partial}{\partial z'}\delta(z-z')\right)B(z)\right]\right]+V(z)\delta(z-z') \qquad (3.20)$$

This is the core equation of the delta function approach for layered heterostructure problems in the one band model. Eq. (3.20) can be compared to Eq. (3.4). Now all integrals have disappeared, and instead the Hamiltonian consists of derivatives of the delta functions and solely depends on the band parameters in the real space. It should be noted that Eq. (3.20) has been obtained without any approximation starting from (3.1) and the integrals for k and k' have been evaluated out in the infinite range rather than within the effective cut-off values as in (3.8) and (3.12). This difference plays an important role in investigating the spurious solutions in later sections. Note that Eq. (3.20) is real and symmetric with respect to the coordinates z and z'. This ensures that the symmetrization which has been discussed above is critical due to the basis-dependent band parameter $B(z)$ as well as non-zero off-diagonal elements in the kinetic energy matrix. However, such additional symmetrization was not necessary in (3.12) since the argument of the band parameter $B(z'')$ is for summation but not for Hamiltonian basis.

When $B(z)$ is constant, $B(z) = B$, (3.20) is reduced to

$$\left\langle z\left|\hat{H}\right|z'\right\rangle = B\frac{\partial}{\partial z'}\left[\left(\frac{\partial}{\partial z}\delta(z-z')\right)\right] + V(z)\delta(z-z') \tag{3.21}$$

The readers can intuitively consider (3.21) as the original Schrödinger equation in which the envelope function has been replaced by the delta function with a minus sign in the kinetic energy term, associating two coordinate bases, not just one.

Before discretizing (3.20) for the numerical treatment, we replace the derivative of the delta function by the alternative definition based on the finite difference form:

$$\frac{\partial}{\partial z}\delta(z-z') = \lim_{h\to 0}\frac{\delta(z+h-z')-\delta(z-z')}{h} \tag{3.22}$$

Then, the kinetic energy term in (3.16) becomes

$$\frac{1}{2}\lim_{h\to 0}\left\{\frac{B(z'+h)\left(\frac{\delta(z+h-z'-h)-\delta(z-z'-h)}{h}\right)-B(z')\left(\frac{\delta(z+h-z')-\delta(z-z')}{h}\right)}{h}\right.$$

$$\left.+\frac{B(z+h)\left(\frac{\delta(z+h-z'-h)-\delta(z+h-z')}{h}\right)-B(z)\left(\frac{\delta(z-z'-h)-\delta(z-z')}{h}\right)}{h}\right\}$$

$$=\frac{1}{2}\lim_{h\to 0}\left[\frac{1}{h^2}(\delta(z-z')[B(z'+h)+B(z')+B(z+h)+B(z)]\right.$$
$$\left.-\delta(z-z'-h)[B(z'+h)+B(z)]-\delta(z-z'+h)[B(z+h)+B(z')]\right] \tag{3.23}$$

Note that (3.19) is still an exact expression without any approximation as long as h infinitesimally goes to zero.

Now we discretize and approximate (3.23) by the equal grid length in the coordinate space, similarly to Eq. (3.5). By substituting $z=(p-1)\Delta z$, $z'=(q-1)\Delta z$, $h=\Delta z = L/(N-1)$, where p and q are 1, 2, 3,..., N, and N is the total number of coordinate grid points, formula (3.23) becomes

$$\frac{1}{2(\Delta z)^2}(\delta((p-q)\Delta z)[B(q\Delta z)+B((q-1)\Delta z)+B(p\Delta z)+B((p-1)\Delta z)]$$
$$-\delta((p-q-1)\Delta z)[B(q\Delta z)+B((p-1)\Delta z)]-\delta((p-q+1)\Delta z)[B(p\Delta z)+B((q-1)\Delta z)])$$

Using the delta function property of Eq. (3.7), we obtain the discretized form of kinetic energy term:

$$\frac{1}{2(\Delta z)^2}\left(\frac{1}{\Delta z}\delta_{pq}\left[B(q\Delta z)+B((q-1)\Delta z)+B(p\Delta z)+B((p-1)\Delta z)\right]\right.$$
$$\left.-\frac{1}{\Delta z}\delta_{p,q+1}\left[B(q\Delta z)+B((p-1)\Delta z)\right]-\frac{1}{\Delta z}\delta_{p,q-1}\left[B(p\Delta z)+B((q-1)\Delta z)\right]\right)$$

$$=\frac{1}{2(\Delta z)^2}\frac{1}{\Delta z}\left(\delta_{pq}\left[B(q\Delta z)+B((q-1)\Delta z)+B(p\Delta z)+B((p-1)\Delta z)\right]\right.$$
$$\left.-\delta_{p,q+1}\left[B(q\Delta z)+B((p-1)\Delta z)\right]-\delta_{p,q-1}\left[B(p\Delta z)+B((q-1)\Delta z)\right]\right)$$

(3.24)

The potential term in (3.20) is also discretized to the same form as in (3.7). Putting it together with (3.24) and using the variational method as in (3.5), (3.6) and (3.8), we obtain the final form of the heterostructure Hamiltonian in the delta function approach:

$$H(p,q)=\frac{1}{2(\Delta z)^2}\left(\delta_{pq}\left[B(q\Delta z)+B((q-1)\Delta z)+B(p\Delta z)+B((p-1)\Delta z)\right]\right.$$
$$\left.-\delta_{p,q+1}\left[B(q\Delta z)+B((p-1)\Delta z)\right]-\delta_{p,q-1}\left[B(p\Delta z)+B((q-1)\Delta z)\right]\right)+V((p-1)\Delta z)\delta_{pq}$$

(3.25)

The eigen solutions of (3.25) can be obtained in the same way as described in section 3.1.1. Compared to the previous formalism in Eqs. (3.8) and (3.12), the kinetic energy part has been dramatically simplified. It is only necessary to know tridiagonal terms, originated from the finite difference form of the derivative of the delta function without any summations. The total number of grid points N does not have to be odd, contrary to (3.8).

When $B(z)$ is a constant in (3.25), i.e., $B(z) = B$, the symmetric form for $B(z)$ is no longer necessary, leading to a much simpler form of the Hamiltonian:

$$H(p,q)=\frac{B}{(\Delta z)^2}\left[2\delta_{pq}-\delta_{p,q+1}-\delta_{p,q-1}\right]+V((p-1)\Delta z)\delta_{pq} \tag{3.26}$$

Note that Eq. (3.26) can be used for any quantum systems with one-dimensional confinement potential and a constant mass. The compactness and simplicity of the Hamiltonian (3.25) and (3.26) differentiate it from the other methods. The superior calculation speed is obvious due to the sparse Hamiltonian matrix elements, which can be immediately defined without any calculus.

The delta function method should not be confused with the finite difference method (FDM)[75] which also employs the tridiagonal matrix. Nevertheless, they are different methods for the following obvious reasons: In the FDM, (i) boundary conditions should be explicitly taken into account upon constructing system equations. (ii) the tridiagonal matrix is not a Hamiltonian matrix. In fact, it comes from the recurrence relation of envelope functions directly discretized at the very beginning from the Schrödinger equation along with boundary conditions at heterojunctions; (iii) the tridiagonal matrix includes the eigenvalues, which have to be solved for. (iv) the matrix inversion is required to obtain envelope functions.

In the following section, we extend the formalism of our method to general multiband **k • p** models based on the EFA.

3.2 Extension of Heterostructure Hamiltonian Formalism Based on Generalized *n*-Band k • p Models

Compared to a parabolic energy dispersion as in (3.1), the actual band structure of semiconductors is much more complicated since each band is highly coupled with the others, leading to the non-parabolicity and the anisotropy. Therefore, except very near the high symmetry points at the band extrema, the parabolic approximation with a constant band-edge effective mass is generally not adequate. There is an approximate recipe to include the non-parabolic correction[138, 139] within a one band model through the energy-dependent effective mass or an additional term to the kinetic energy which is of the fourth order in k_z. However, its use should be still limited by the close vicinity of the band extrema by definition.

Including band-to-band interactions for an accurate band structure by explicitly solving the coupled high order partial differential equations is essential especially when dealing with low-dimensional confinement, electronic states with high in-plane momenta or large free carrier densities.

For the transition from bulk to heterostructure problems, each basis of the N coordinate space is acted on a general n-band bulk Hamiltonian $H_{n\times n}$. The resulting matrix is a $nN\times nN$ heterostructure Hamiltonian shown in (3.27).

$$\begin{pmatrix} \langle 1|H_{n\times n}|1\rangle & \langle 1|H_{n\times n}|2\rangle & \cdots & \langle 1|H_{n\times n}|N\rangle \\ \langle 2|H_{n\times n}|1\rangle & \langle 2|H_{n\times n}|2\rangle & \cdots & \langle 2|H_{n\times n}|N\rangle \\ \vdots & \vdots & \ddots & \vdots \\ \langle N|H_{n\times n}|1\rangle & \langle N|H_{n\times n}|2\rangle & \cdots & \langle N|H_{n\times n}|N\rangle \end{pmatrix} \begin{pmatrix} \overline{F}_{1n} \\ \overline{F}_{2n} \\ \vdots \\ \overline{F}_{Nn} \end{pmatrix} = E \begin{pmatrix} \overline{F}_{1n} \\ \overline{F}_{2n} \\ \vdots \\ \overline{F}_{Nn} \end{pmatrix} \tag{3.27}$$

where

$$\overline{F}_{in} = \begin{pmatrix} f_i^{\,1} \\ f_i^{\,2} \\ \vdots \\ f_i^{\,n} \end{pmatrix}$$

and E is a real constant eigenvalue. For whole eigenvalues for a system, eigenvalues and eigenfunctions are also $nN \times nN$ matrices. $\overline{F}_{in}$ is a column vector of length n for ith coordinate basis.

However, Eq. (3.27) is not a convenient form to directly apply the formalism obtained in the previous sections. Therefore, using linear algebra, we rewrite (3.27) as

$$\begin{pmatrix} \langle i|H_{11}|j\rangle & \langle i|H_{12}|j\rangle & \cdots & \langle i|H_{1n}|j\rangle \\ \langle i|H_{21}|j\rangle & \langle i|H_{22}|j\rangle & \cdots & \langle i|H_{2n}|j\rangle \\ \vdots & \vdots & \ddots & \vdots \\ \langle i|H_{n1}|j\rangle & \langle i|H_{n2}|j\rangle & \cdots & \langle i|H_{nn}|j\rangle \end{pmatrix} \begin{pmatrix} F_{1N} \\ F_{2N} \\ \vdots \\ F_{nN} \end{pmatrix} = E \begin{pmatrix} F_{1N} \\ F_{2N} \\ \vdots \\ F_{nN} \end{pmatrix} \tag{3.28}$$

where

$$F_{nN} = \begin{pmatrix} f_1^{\,n} \\ f_2^{\,n} \\ \vdots \\ f_N^{\,n} \end{pmatrix}$$

Here i and j run over 1 to N, $\langle i|H_{\alpha\beta}|j\rangle$ is an $N \times N$ square matrix, n is a bulk band index , and F_{nN} is a column vector of length N, representing the envelope function for n^{th} band. Eq. (3.28) shows that a heterostructure Hamiltonian is constructed such that each bulk Hamiltonian matrix element $H_{\alpha\beta}$ is transformed to an $N \times N$ square block matrix, $\langle i|H_{\alpha\beta}|j\rangle$.

In this paper, we restrict the highest order of momentum to the second order in bulk Hamiltonian matrix elements. A usual 8-band k • p model (see APPENDIX A) conforms to this category. Therefore, the bulk Hamiltonian matrix elements contain zeroth order, linear, and quadratic terms with respect to the confined wave number k_z. In the one band case, we have already shown how the second order term with respect to k_z is transformed to the heterostructure case with N grid points in the coordinate space for three different approaches. Therefore, each of them can be readily applied to the conversion of bulk multi-band Hamiltonian matrix elements to the heterostructure case. They are explicitly rewritten again from section 3.1.1 ~ 3.1.3 as

$$H_{\alpha\beta}\left(k_z^2\right) \Rightarrow \frac{4(\Delta k)^2}{N^2}\sum_{s=1}^{N}\left[B_{\alpha\beta}\left((s-1)\Delta z\right)\left(\sum_{a=1}^{m} a\cos\left[\frac{2\pi a(p-s)}{N}\right]\right)\left(\sum_{b=1}^{m} b\cos\left[\frac{2\pi b(s-q)}{N}\right]\right)\right] \tag{3.29}$$

$$H_{\alpha\beta}\left(k_z^2\right) \Rightarrow \frac{4}{(2\pi)^2}(\Delta z)^2\sum_{s=1}^{N}\left[B_{\alpha\beta}\left((s-1)\Delta z\right)\left(\frac{k_m\cos\left(\frac{2\pi}{N}m(p-s)\right)}{(p-s)\Delta z}-\frac{\sin\left(\frac{2\pi}{N}m(p-s)\right)}{(p-s)^2(\Delta z)^2}\right)\right.$$
$$\left.\times\left(\frac{k_m\cos\left(\frac{2\pi}{N}m(q-s)\right)}{(q-s)\Delta z}-\frac{\sin\left(\frac{2\pi}{N}m(q-s)\right)}{(q-s)^2(\Delta z)^2}\right)\right] \tag{3.30}$$

$$H_{\alpha\beta}\left(k_z^2\right) \Rightarrow \frac{1}{2(\Delta z)^2}\left(\delta_{pq}\left[B_{\alpha\beta}(q\Delta z)+B_{\alpha\beta}\left((q-1)\Delta z\right)+B_{\alpha\beta}(p\Delta z)+B_{\alpha\beta}\left((p-1)\Delta z\right)\right]\right.$$
$$\left.-\delta_{p,q+1}\left[B_{\alpha\beta}(q\Delta z)+B_{\alpha\beta}\left((p-1)\Delta z\right)\right]-\delta_{p,q-1}\left[B_{\alpha\beta}(p\Delta z)+B_{\alpha\beta}\left((q-1)\Delta z\right)\right]\right) \tag{3.31}$$

where $H_{\alpha\beta}$ is a bulk **k • p** Hamiltonian matrix element, $B_{\alpha\beta}$ is the corresponding bulk band parameter, and the rest of the notations is the same as in the previous sections.

It remains to derive the linear terms, $B_{\alpha\beta}(\hat{z})\hat{k}_z$ and zeroth order terms to represent a complete heterostructure Hamiltonian in the multiband case. Basically, the procedure of the derivation for the linear term is same as shown above for the quadratic term. In the coordinate space, $B_{\alpha\beta}(\hat{z})\hat{k}_z$ can be expressed as

$$\frac{1}{2}\left\langle z\left|B_{\alpha\beta}(\hat{z})\hat{k}+\hat{k}B_{\alpha\beta}(\hat{z})\right|z'\right\rangle \tag{3.32}$$

where $\hat{k}_z$ is simplified to $\hat{k}$, and $B_{\alpha\beta}(\hat{z})\hat{k}_z$ has been symmetrized to be Hermitian. Following the procedure of going from (3.2) to (3.4), formula (3.32) becomes

$$\frac{1}{4\pi}\left[\left(B_{\alpha\beta}(z)+B_{\alpha\beta}(z')\right)\int_{-\infty}^{\infty}e^{ik(z-z')}kdk\right] \tag{3.33}$$

In the quadratic term, two exponential terms were associated with two quasi-particle momenta, *k* and *k'*. However, in the linear term, only single exponential term appears instead. Following the section 3.1.1 ~ 3.1.3, the discretized forms of linear terms for the three approaches become

$$H_{\alpha\beta}(k_z)\Rightarrow\left(\frac{1}{N}\right)\Delta k\left[B_{\alpha\beta}\left((p-1)\Delta x\right)+B_{\alpha\beta}\left((q-1)\Delta x\right)\right]\sum_{a=1}^{m}a\cos\left[\frac{2a\pi(p-q)}{N}\right] \tag{3.34}$$

$$H_{\alpha\beta}(k_z)\Rightarrow-\frac{i}{2\pi}(\Delta z)\left[B_{\alpha\beta}\left((p-1)\Delta z\right)+B_{\alpha\beta}\left((q-1)\Delta z\right)\right]\left[\frac{k_m\cos\left(\frac{2\pi}{N}m(p-q)\right)}{(p-q)\Delta z}-\frac{\sin\left(\frac{2\pi}{N}m(p-q)\right)}{(p-q)^2(\Delta z)^2}\right] \tag{3.35}$$

$$(p\neq q)$$

$$H_{\alpha\beta}(k_z) \Rightarrow \frac{i}{4(\Delta z)}\left[B_{\alpha\beta}((p-1)\Delta z) + B_{\alpha\beta}((q-1)\Delta z)\right]\left(\delta_{p,q+1} - \delta_{p,q-1}\right) \tag{3.36}$$

where notations are the same as before. Contrary to the quadratic case, diagonal elements for linear terms are zeros in the block square matrix in Eqs. (3.35) and (3.36). In the delta function approach given by formula (3.36) one additional symmetrization has been performed by the linear combination of the two possible derivatives for $ke^{ik(x-x')}$ as shown in (3.9) and (3.10) to make the Hamiltonian Hermitian.

All terms that do not depend on k_z or zeroth order terms with respect to k_z in a bulk Hamiltonian matrix are transformed to an $N \times N$ diagonal matrix in the coordinate space regardless of the three different approaches in section 3.1.1 ~ 3.1.3, i.e,

$$H_{\alpha\beta}\left((k_z)^0\right) \Rightarrow B_{\alpha\beta}\delta_{pq} \tag{3.37}$$

For example, in-plane momentum $\mathbf{k}_{||}$-dependent terms and the potential energy terms correspond to this classification.

As we have shown above, the extension from the one band heterostructure problem to the multiband case is straightforward within our method once bulk k • p models are known. This extreme simplicity is the unique feature of the heterostructure Hamiltonian method.

In the next section, we show the numerical results of eigen solutions obtained by the heterostructure Hamiltonian method in the one band, the 6-valence band, and the 8-band k • p models. Particularly, in the case of the one band model, subband levels are compared to analytical results in single quantum well heterostructures.

3.3 Numerical Results and Spurious Solutions

3.3.1 One-Band Case

The numerical results in the one band model are shown in Table III-1 and Fig. 3-1~3.3 for single quantum wells of $Ga_{0.47}In_{0.53}As$ surrounded by $Al_{0.48}In_{0.52}As$ barriers with 1 Å grid length and various quantum well widths. They are obtained by the three different methods derived in section 3.1.1~3.1.3 and compared to the analytical solutions [16]. The formalism that produces the most accurate result is the modified Fourier grid Hamiltonian method (MFGHM) based on the approach shown in the section 3.1.2. The results obtained by the delta function method (DFM) in section 3.1.3 show nearly the same accuracy as those by the MFGHM. With the same grid length, both the MFGHM and the DFM are superior in the accuracy of eigen solutions to that of the shooting method, (for example, see Ref. [136]) which is widely used but limited to the one band model. The MFGHM provides an extreme accuracy along with simplicity. The formalism based on the original Fourier grid Hamiltonian method (FGHM) in section 3.1.1 shows the worst accuracy among the three approaches.

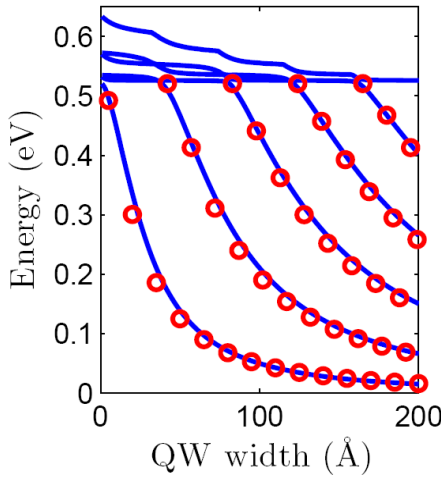

Fig. 3-1. The confined subband energies obtained by the Fourier grid Hamiltonian method (blue solid lines) based on the section 3.1.1 are compared with the analytical results (red circle) in $Ga_{0.47}In_{0.53}As$ / $Al_{0.48}In_{0.52}As$ single quantum wells as a function of the well width. Numerical values are shown in Table III-1. The discrepancy between the two cases is noticeable.

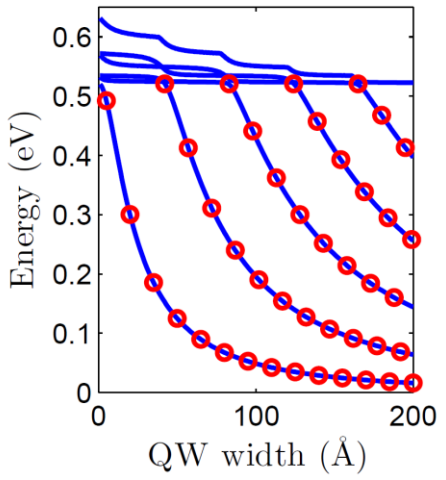

Fig. 3-2. The confined subband energies obtained by the modified Fourier grid Hamiltonian method (blue solid line) based on the section 3.1.2 are compared with the analytic results (red circle) in $Ga_{0.47}In_{0.53}As$ / $Al_{0.48}In_{0.52}As$ single quantum wells as a function of the well width. Numerical values are shown in Table III-1. The numerical and analytic solutions coincide for all eigenstates and well widths.

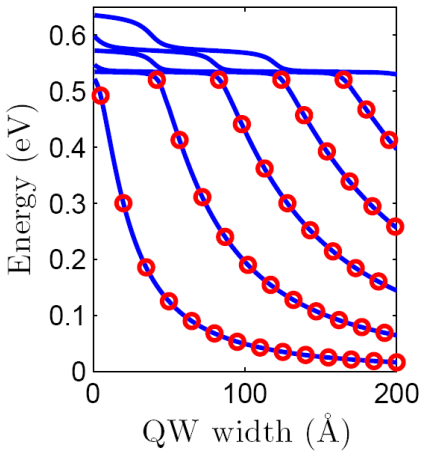

Fig. 3-3. The confined subband energies obtained by the delta function method (blue solid lines) based on the section 3.1.3 are compared with the analytic results (red circle) in $Ga_{0.47}In_{0.53}As$ / $Al_{0.48}In_{0.52}As$ single quantum wells as a function of well width. Numerical values are provided in Table III-1.

The accuracy of confined subband levels can be further improved by decreasing grid lengths, eventually approaching the analytic solution as shown in Table III-2, calculated for a 20 Å single $Ga_{0.47}In_{0.53}As/Al_{0.48}In_{0.52}As$ quantum well .

Table III-1: Energies of confined eigenstates in a single $Ga_{0.47}In_{0.53}As$ quantum well surrounded by a 200 Å $Al_{0.48}In_{0.52}As$ barrier. The numerical results obtained by the Fourier grid Hamiltonian method (FGHM), the modified Fourier grid Hamiltonian method (MFGHM), and the delta function method (DFM) in the one band model for grid length of 1 Å are compared with the analytic solutions for various well widths. The band parameters from Ref. [20] are used. The MFGHM shows the most accurate subband energies.

Well width (Å)		40	80	120	160	200
E_1 (meV)	Analytical	161.25985	67.554882	36.934941	23.253849	15.977027
	FGHM	182.43827	70.902619	36.626685	22.196255	14.839734
	MFGHM	161.20016	67.536622	36.927318	23.249987	15.974811
	DFM	161.14823	67.513335	36.916341	23.244135	15.971368
E_2 (meV)	Analytical	-	269.97003	148.17194	93.21242	63.997522
	FGHM	-	288.67084	158.37179	97.914199	66.157427
	MFGHM	-	269.91372	148.14388	93.197475	63.988762
	DFM	-	269.85384	148.11024	93.177495	63.976236
E_3 (meV)	Analytical	-	-	331.18192	209.81867	144.16398
	FGHM	-	-	343.66261	219.86289	150.21993
	MFGHM	-	-	331.14028	209.79109	144.14664
	DFM	-	-	331.05605	209.74429	144.11765

Table III-2: Energy of the ground subband in a 20Å $Ga_{0.47}In_{0.53}As/Al_{0.48}In_{0.52}As$ single quantum well, calculated with the MFGM and the delta function method, and compared with the analytical solution. As grid length decreases, the numerical solutions approach the analytical solution.

Grid length (Å)	Analytical solution (meV)	MFGH method (meV)	Delta function method (meV)
1	300.3039163	300.192223	300.1365936
0.5		300.2756513	300.2620914
0.2		300.2993678	300.2972307
0.1		300.3027823	300.3022506

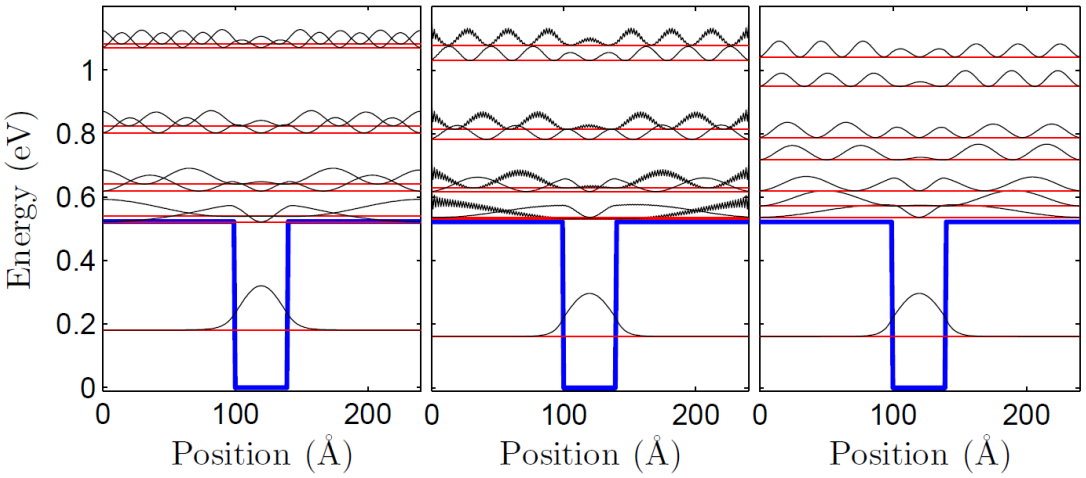

Fig. 3-4. The eigen solutions in a 40 Å $Ga_{0.47}In_{0.53}As$ / $Al_{0.48}In_{0.52}As$ single quantum well are compared for three different approaches described in section 3.1 based on the one band model. Left panel: the Fourier grid Hamiltonian method (FGHM), middle panel: the modified Fourier grid Hamiltonian method (MFGHM), right panel: the delta function method (DFM). In the FGHM and the DFM, spurious solutions do not appear. However, the MFGHM produces them in the continuum as fast oscillating envelope functions. The spurious solutions are responsible for the difference of continuum states between the MFGHM and the DFM.

However, as shown in Fig. 3-4 (middle panel), the MFGHM generates fast oscillating continuum states i.e., the spurious solutions, which are the only subbands that are different from those in the DFM. Note that all confined electron states in Fig. 3-4 are free from spurious solutions and are not affected by the presence of the latter, as indicated in Table III-1 and Fig. 3-2.

Since the FGHM does not produce the unphysical solutions, we were able to figure out their origin and remove them by comparing with the MFGHM. The only difference between the two methods lies in the manner how the quasi-particle wave number integrals are dealt with. The FGHM treats them by the discretization with equal lengths as in Eq. (3.38), while the MFGHM exactly evaluates them analytically as in Eq. (3.39).

$$\frac{2\pi}{N}(\Delta k)\sum_{\beta=1}^{m}\beta\cos\left[\frac{2\pi\beta(p-s)}{N}\right] \tag{3.38}$$

$$\frac{k_m\cos\left(\frac{2\pi}{N}m(p-s)\right)}{(p-s)}-\frac{\sin\left(\frac{2\pi}{N}m(p-s)\right)}{(p-s)^2\Delta z} \tag{3.39}$$

where Δz is taken to be 1 Å for simplicity. In (3.39), the first cosine term is dominant due to the factor k_m.

For a 40 Å GaInAs/AlInAs well, expressions (3.38) and (3.39) are plotted in Fig. 3-5 as a function of the index s (see Eq. (3.29, 3.30)) for a given p = 120, which corresponds to the center of the quantum well. Each of (3.38) and (3.39) is an even or an odd function, which shows a peak or a zero point at $|p - s| = 0$ respectively, and the parity becomes opposite at that point. Also, as the absolute value $|p - s|$ increases, the

amplitudes of (3.38) are much more quickly suppressed than those of (3.39). It is important to notice that their different behavior is not related to the cut-off value of wave vector k since the latter is determined by the reciprocal length of a heterostructure in both cases.

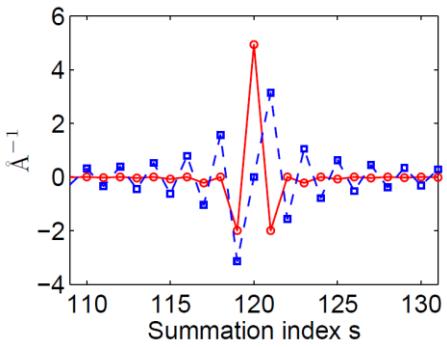

Fig. 3-5. The wave number integrals, expression (3.38) (circle solid line) and (3.39) (square, dashed line) that appear in the Fourier grid Hamiltonian method (FGHM) (see (3.8)) and the modified Fourier grid Hamiltonian method (MFGHM) (see (3.12)) respectively are plotted as a function of the summation coordinate index s for a given real space basis p = 120, which corresponds to the center of the quantum well shown in Fig. 3-4 with the grid length of 1 Å. The parity between the two cases becomes opposite at s = 121 and higher.

To remove the spurious solutions in the MFGHM, we try to achieve the characteristics of the wave number integral in the FGHM by introducing a certain shift factor α, i.e., with replacing s to s-α in (3.39). Any small shift factor can lead to a non-zero wave number integral at $|p - s| = 0$ (or $|q - s| = 0$). Also, the shift of $\Delta z/2$ makes the wave number integral decay much more quickly as $|p - s|$ (or $|q - s|$) increases. Such behavior originates from the destructive interference of the wave number integral due to the shift. Figure 3-6 shows expression (3.39) before and after applying the shift factor.

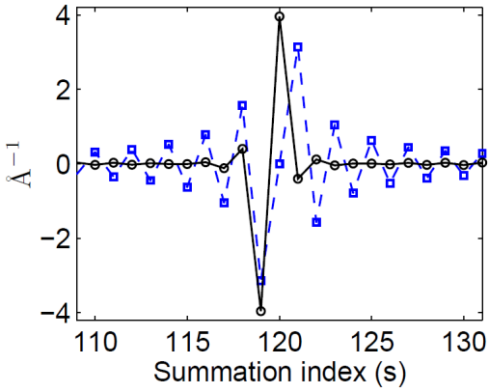

Fig. 3-6. The wave number integral, expression (3.39), before (square, dashed line) and after (circle, solid line) adding a shift factor $+\Delta z/2$ to s in (3.39) calculated by the MFGHM for a given $p = 120$. Such a shift factor removes the fast oscillating spurious solutions in the continuum in the MFGHM as shown in Fig. 3-7, which can be compared to Fig. 3-4 (middle panel) before the removal of fast oscillating spurious solutions.

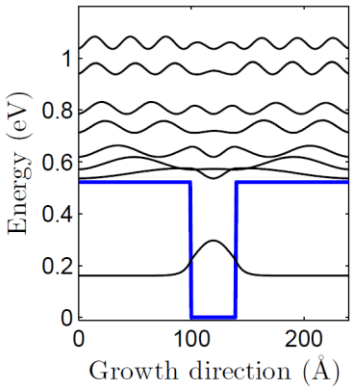

Fig. 3-7. The eigenstates (envelope functions) obtained by the MFGHN after introducing the shift factor of $\pm\Delta z/2$ in (3.39). The fast oscillating envelope functions in the continuum present in Fig. 3-4 (middle panel) are now disappeared. The average of Hamiltonians for each positive and negative shift is used to preserve the symmetry of envelope functions based on the one-band model. The subband levels now resemble those obtained by the DFM (see Fig. 3-4 (right panel)). Their numerical values are compared in Table III-3 for the same grid length of 1 Å. A small shift factor weakly affects confined energy levels.

Table III-3: Energies of confined states in a single 40Å $Ga_{0.47}In_{0.53}As$ quantum well surrounded by a 100 Å $Al_{0.48}In_{0.52}As$ barrier, after spurious solution have been removed by introducing the shift factor $\pm\Delta z/2$ in wave number integrals (see the text) in the MFGHM are compared to eigen solutions obtained in the DFM.

	Spurious-solution-free MFGHM (meV)	DFM (meV)
CB 1	161.63119	161.1482357
CB 2	536.397413	536.5257855
CB 3	571.43349	572.1300149
CB 4	618.887341	620.10291
CB 5	714.70258	717.2621885
CB 6	784.423103	787.7672658

In addition, to keep the symmetry of envelope functions even after introducing the shift factor, the average of two Hamiltonians obtained by the positive and negative shifts is used. The resulting eigen solutions are now free from the spurious solutions as shown in Fig. 3-7 with the shift factor $\alpha = \pm\Delta z/2$, and they resemble those obtained by the DFM in Fig. 3-4 (right panel) rather than those by the FGHM (Fig. 3-4 (left panel)). The spurious solution-free eigenvalues after the shift factor is introduced in the MFGHM are compared with those obtained by the DFM in Table III-3 for the same quantum well structure as shown in Fig. 3-4 with the same grid length of 1 Å. Subband levels in the DFM are more accurate now. Since the larger shifts diminish away the accuracy of eigen solutions, the minimal shift to just remove the spurious solutions will be optimal. The removal of fast oscillating envelope functions in the above comes at the price of approximating the exact wave number integral. Note that we exclude the possibility that

the removal of spurious solutions may be attributed to the implicit change of interface boundary conditions due to the shift factor. We will extend the discussion on the spurious solutions for the multiband case in the next section.

3.3.2 Heterostructure Eigen Solutions in the 8-band k • p Model

The Hamiltonians constructed in section 3.2 for heterostructure problems with one dimensional confinement based on multiband k • p models (see the APPENDIX A for the bulk Hamiltonian of a 8-band k • p model) can be easily solved for eigen solutions by a standard eigenvalue solver. The numerical results for confined subband energy levels in a single GaAs/AlGaAs quantum well by the 6-valence band and the 8-band k • p models are shown in Table III-4 for the in-plane wave vector $k_{||} = 0$. First of all, in the 6-valence band case, the subband positions obtained by the FGHM significantly deviate from those obtained by the other two methods, i.e., the MFGHM and the DFM. The discrepancy becomes larger with increasing $k_{||}$ as shown in Fig. 3-8 and 3-9. On the other hand, the MFGHM and the DFM give nearly the same subband positions. Figure 3-8 shows such an agreement in the in-plane subband dispersion. Note that the DFM and the FGHM do not produce any kind of spurious solutions within the 6-valence band model. On the other hand, in the MFGHM they occur in the continuum again and can be removed just like in its one band model case. The general trend of

eigen solutions obtained by the three methods in the 6-valence k • p band model is consistent with that in the one band model.

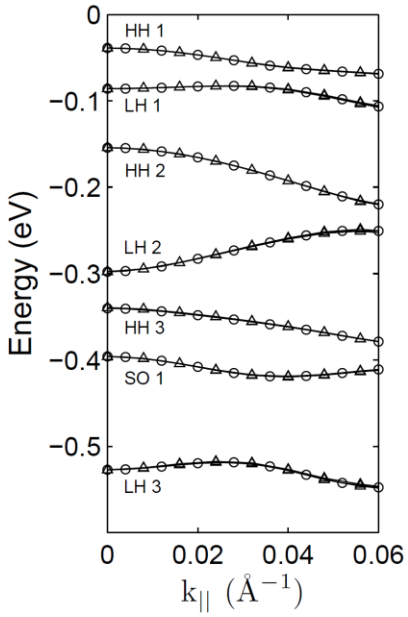

Fig. 3-8. The in-plane dispersion of subbands in the valence band of a 42 Å GaAs/AlAs single quantum well obtained by the MFGHM (circle) and the DFM (triangle) based on the 6-valence band k • p model. Energies are measured from the top of the valence band. Results can be compared to Fig. 5 in Ref. [76].

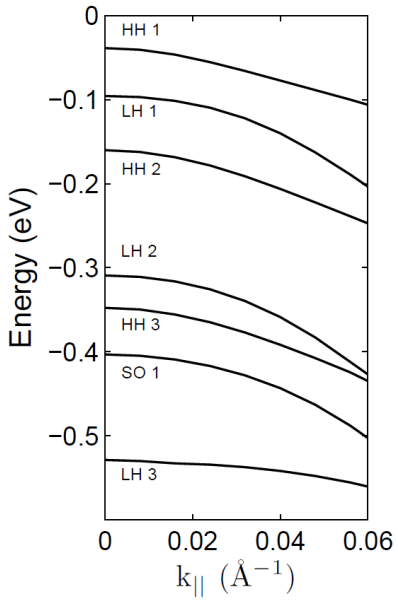

Fig. 3-9. The in-plane dispersion of subbands in the valence band of a 42 Å GaAs/AlAs single quantum well heterostructure obtained by the FGHM based on the 6-valence band k • p model. Energies are measured from the top of the valence band. This plot shows a severe discrepancy with Fig. 3-8 as $k_{||}$ becomes large.

Upon including the conduction band to the 6-valence band, i.e., in the 8-band model, subband levels at $k_{||} = 0$, calculated by the FGHM, the MFGHM, and the DFM, are compared in Table III-4. The general pattern in terms of accuracy of eigen solutions is the same as in both the one-band and the 6-valence band cases. However, in the transition from the 6-band to the 8-band model, unphysical solutions of another kind appear in the band gap in the DFM as shown in Fig. 3-10 (right). Also, the fast oscillating envelope functions can occur in very high continuum states even within the DFM although they are not shown in the chosen quantum well heterostructure in Fig. 3-10~12. The tendency of spurious solutions in a heterostructure calculated by the MFGHM under the 8-band k • p model is more or less the same as in both the one- band

and the 6-valence band models, showing the fast oscillating continuum states and no spurious solutions in confined states. The eigen solutions obtained by the FGHM are still completely free from any kind of spurious solutions even if they are not so accurate. The above features of the three different approaches in the real space heterostructure Hamiltonian methods are summarized in Table III-5.

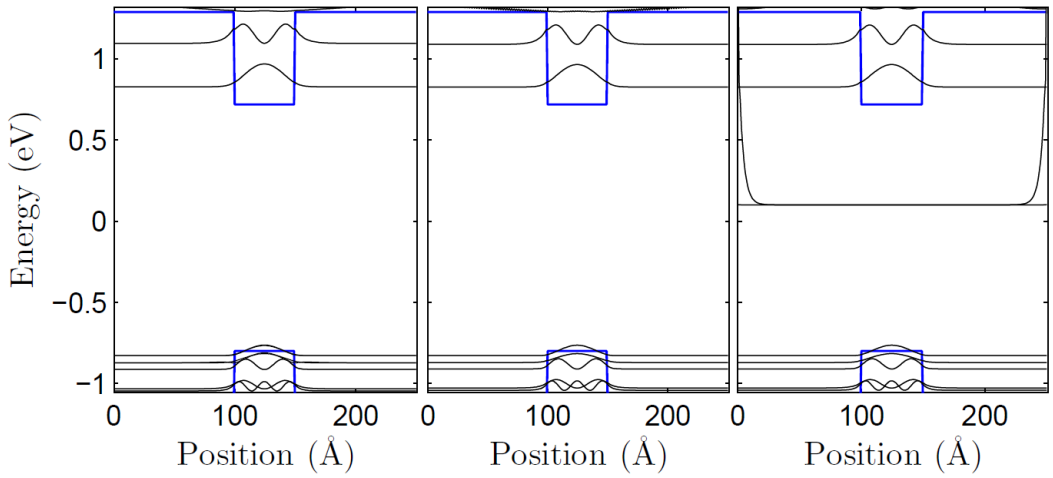

Fig. 3-10. Eigen solutions in a single quantum well GaAs/$Al_{0.7}Ga_{0.3}As$ heterostructure of well width 50 Å, obtained by the FGHM (left), the MFGHM (middle), and the DFM (right) based on the 8-band k • p model are shown near the band gap region. The first two heterostructure Hamiltonian methods do not produce any spurious solutions in the band gap, but the DFM does.

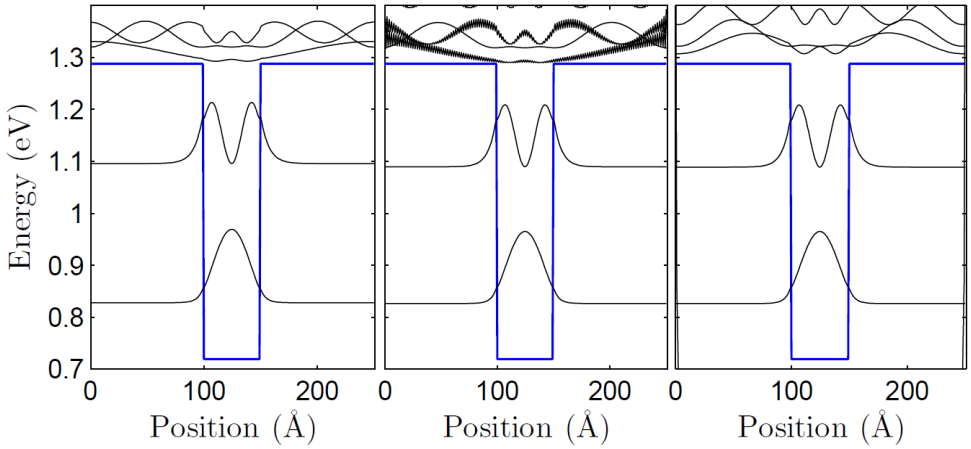

Fig. 3-11. Eigen solutions in the conduction band of a single quantum well GaAs/$Al_{0.7}Ga_{0.3}As$ heterostructure of well width 50 Å, obtained by the FGHM (left), the MFGHM (middle), and the DFM (right) at the Γ point based on the 8-band k • p model. Only the MFGHM produces fast oscillating envelope functions in the continuum. However, such spurious solutions do not occur in the confined states. The amplitudes of envelope functions have been enhanced for better visualization.

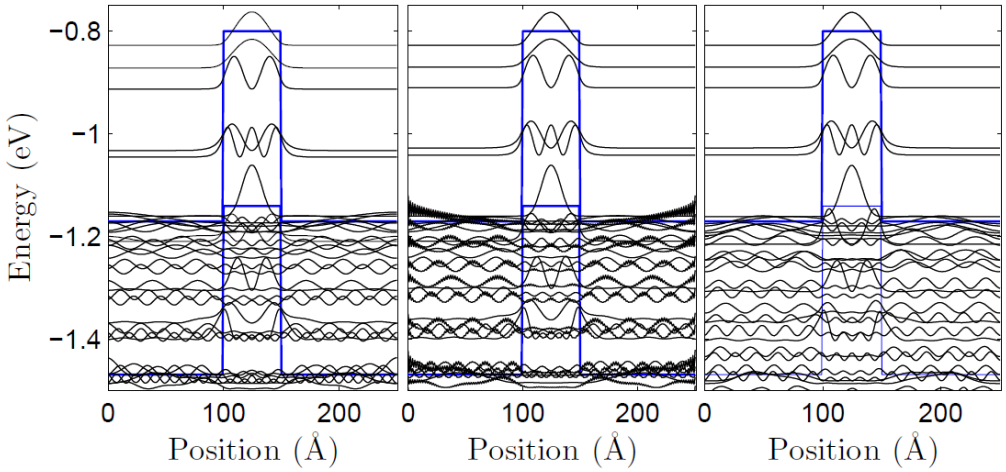

Fig. 3-12. Eigen solutions in the valence band of a single quantum well GaAs/$Al_{0.7}Ga_{0.3}As$ heterostructure of well width 50 Å, obtained by the FGHM (left), the MFGHM (middle), and the DFM (right) at the Γ point based on the 8-band k • p model. Only the MFGHM produces the fast oscillating envelope functions in the continuum. However, such spurious solutions do not occur for the confined states. The amplitudes of envelope functions have been enhanced for better visualization.

Table III-4: The subband levels obtained by the three heterostructure Hamiltonian methods are compared within the 6-valence band model and the 8-band k • p model for a single 50 Å GaAs/$Ga_{0.3}Al_{0.7}As$ quantum well at $k_{||} = 0$. The differences in the subband levels between the MFGHM and the DFM are less than 1 meV in both models. As with the one band model, the eigen solutions obtained by the FGHM are significantly different from those obtained by the other two methods. Here a grid length of 1 Å has been used.

	FGHM (meV)	MFGHM (meV)	DFM (meV)
	8-band k • p model		
CB1	108.64504	107.24964	107.15618
CB2	376.82667	370.37231	369.78052
HH1	-27.69696	-27.88907	-27.86137
LH1	-72.15378	-70.37055	-70.32858
HH2	-113.0806	-110.4117	-110.2825
LH2	-232.8446	-227.8996	-227.6626
HH3	-245.3835	-241.8397	-241.4504
SO1	-360.5566	-360.6551	-361.2818
	6-valence band k • p model		
HH1	-27.69696	-27.88907	-27.86137
LH1	-70.431	-66.44799	-66.4151
HH2	-113.0806	-110.4117	-110.2825
LH2	-237.2404	-231.095	-230.9851
HH3	-245.3835	-241.8397	-241.4504
SO1	-360.7283	-360.8921	-361.5259

Table III-5: The characteristics of the three approaches in the heterostructure Hamiltonian method are compared regarding the generation of spurious solutions and the accuracy of eigen solutions in the one-band, the 6-valence band, and the 8-band k • p models.

	A one-band model		A 6-VB k • p model		A 8-band k • p model	
	Spurious solutions	Accuracy of confined states	Spurious solutions	Accuracy of confined states	Spurious solutions	Accuracy of confined states
FGHM	No	No	No	No	No	No
MFGHM	Only in the continuum	Yes	Only in the continuum in VB	Yes	Only in the continuum in CB & VB	Yes
DFM	No	Yes	No	Yes	In the high continuum of CB or/and in BG	Yes

By comparing the eigen solutions obtained by the 6- and 8-band models in Table III-4, it is important to recognize that the occurrence of spurious solutions in the middle of the band gap does not affect the true confined eigen states.

In the case of the 8-band model, we apply the same strategy which has been used for eliminating the fast oscillating continuum states in the one-band and the 6-valence band model by introducing the shift factor $\pm\Delta z/2$ in the wave number integral in the MFGHM followed by averaging heterostructure Hamiltonians at positive and negative shifts. As a result, most of the fast oscillating envelope functions in the valence band continuum are removed, but those in the conduction band continuum still reside nearly without change. However, note that there are no unphysical solutions in the band gap as in the one- and 6-valence band cases.

To summarize the behavior of the spurious solutions, the unphysical eigen solutions in the middle of the band gap are originated from the contribution of large wave number values in the wave number integrals in sections II.2 and II.3. In the MFGHM, upon evaluating the integrals, k values have been cut off by the Fourier reciprocal relation. On the other hand, in the DFM, those integrals have been analytically integrated over the infinite range without any truncation of k, and the final formalism solely depends on the band parameters in the real space. For the other type of spurious solutions, i.e., the fast oscillating envelope functions, their removal is related to sacrificing the accuracy of the eigen solutions as can be seen in the comparison of the FGHM and the MFGHM.

The in-plane subband dispersion in the valence band, obtained by the MFGHM, are compared for the 6-and 8-band cases in Fig. 3-13, i.e., with and without an explicit inclusion of the conduction band, which is done by modifying the Luttinger parameters. It shows that the change of the valence band interaction with remote bands in bulk materials influence the valence band in-plane dispersion in heterostructures. Figure 3-13 can be compared to Fig. 3-5 in Ref. [76].

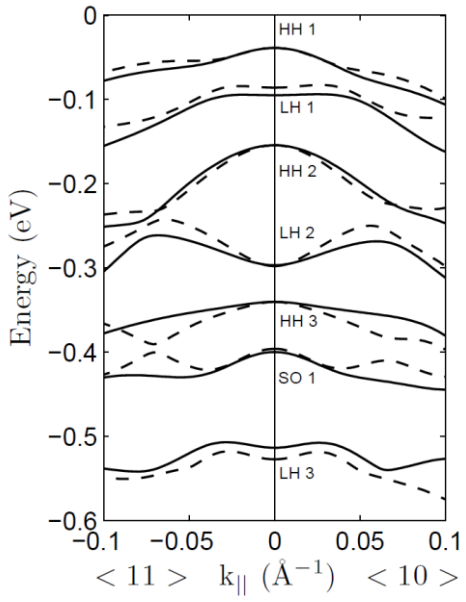

Fig. 3-13. The in-plane dispersion of subbands in the valence band of a 42 Å GaAs/AlAs single quantum well heterostructure obtained by the MFGHM based on the 6-valence band (dashed) and the 8-band (solid) k • p model. At large $k_{||}$, the disagreement becomes obvious. This indicates that the modification of the valence band interaction parameters (Luttinger parameters) due to the explicit inclusion of the conduction band has non-negligible influences on subband positions. The crossing of subband dispersions is sharper in the 6-band model.

We also investigated the effect of square wave-like abrupt hetero-interfaces of bulk band parameters on spurious solutions by the Fourier series expansion [137] as in expression (3.40). The abruptness of the band parameters at interfaces is effectively controlled by the upper limit, n_{max}, of the summation in (3.40). Figure 3-14 shows that such replacement only improves the smoothness of envelope functions at the interface boundary, and it rarely affects both types of spurious solutions.

$$B(z) \approx \frac{a_0}{2} + \sum_{n=1}^{n_{\max}} a_n \cos\left(nk_L z\right) + \sum_{n=1}^{n_{\max}} a_n \sin\left(nk_L z\right) \tag{3.40}$$

where $k_L = 2\pi/L$, L is a system length, and

$$a_0 = \frac{2}{L}\sum_{s=1}^{N_{ly}} B_s\left(L_{s+1} - L_s\right)$$

$$a_n = \frac{1}{n\pi}\sum_{s=1}^{N_{ly}} B_s\left[\sin\left(nk_L L_{s+1}\right) - \sin\left(nk_L L_s\right)\right]$$

$$b_n = -\frac{1}{n\pi}\sum_{s=1}^{N_{ly}} B_s\left[\cos\left(nk_L L_{s+1}\right) - \cos\left(nk_L L_s\right)\right]$$

where N_{ly} is the number of layers, $L_1 = 0$, and $L_{N_{ly}+1} = L$.

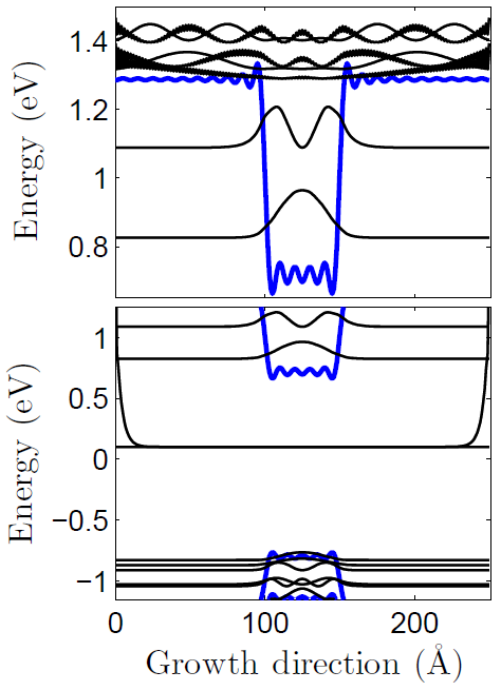

Fig. 3-14. The same quantum well as in Fig. 3-13 but with square wave-like abrupt interfaces of band parameters replaced by the smooth ones using the Fourier expansion of the coordinate dependent band parameters, Eq. (3.40), calculated by the MFGHM (top) and the DFM (bottom). Smoothness of interfaces does not affect the spurious solutions in both cases, only the envelope functions at interfaces become smoother. There are nine interface grid points with $n_{max} = 25$ in Eq. (3.40).

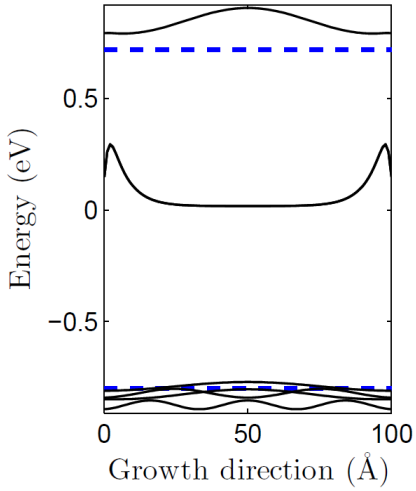

Fig. 3-15. Eigen solutions obtained by the DFM with the 8-band k • p model in a 100 Å GaAs single layer. The unphysical eigen solutions inside the band gap (dashed) can be observed. The band parameters in Ref. [20] are used; the band parameters recommended in Ref. [82] cannot remove the solution in the middle of the band gap.

Figure 3-15 shows the eigen solutions in a single GaAs layer calculated by the DFM, in which band parameters in Ref. [20] are used, and a spurious solution is observed. As long as such spurious solutions appear in a single GaAs layer, it is generally impossible to completely remove them in GaAs-based heterostructures even if some of heterostructures can be free from spurious solutions due to certain destructive interferences. The way to modify the Luttinger parameters to prevent spurious solutions in the band gap has been reported based on the finite difference method [82]. However, this prescription fails in the general case. The universal method which can remove the existing spurious solutions within the EFA is currently absent.

4. PASSIVE THz DFG BASED ON INTERSUBBAND NONLINEARITY IN SEMICONDUCTOR MQW STRUCTURES

4.1 Invalidity of Non-Pump depletion Approximation (NPDA) in Passive Devices

The use of NDPA mentioned in section 1.5 should be restricted to a lossless medium for pump fields since it is obtained under the approximation in which pump fields are not decaying at all, and linear and nonlinear (NL) optical susceptibilities are assumed to be constant when dealing with propagating coupled electromagnetic fields. This approximation is not adequate for the passive THz DFG in the current work. As a matter of fact, pump intensities vary in a complicated way depending on doping densities in the nonlinear section, detunings, and incident pump powers.

In addition, the conventional approach to nonlinear mixing problems [112-114] based on Eq. (1.1) or coupled field equations does not take into account the variation of subband populations, electronic states of multiple quantum well structures and matrix elements of intersubband transitions affected by initial pumping powers, detunings, and the propagation of coupled fields. In this dissertation, we present the results of a fully self-consistent approach which incorporates all these effects by solving the Schrödinger equation, the Poisson equation, the density matrix equations, and the coupled field equations.

4.2 Self-Consistent Calculations of the Coupled Field Propagation and Electronic States of MQW Heterostructure

We consider the DFG in a GaInAs/AlInAs multiple quantum well structure as an example, although our approach can be applied to any heterostructures. A schematic picture of the energy levels (E_1, E_2, E_3), propagating pump fields (e_1, e_2) or the Rabi frequencies ($\Omega_1 = d_{12}e_1/\hbar$, $\Omega_2 = d_{13}e_1/\hbar$), and detunings ($\Delta_1 = E_{21} - \hbar\omega_1$, $\Delta_2 = E_{31} - \hbar\omega_2$) are shown in Fig. 1-4. The difference ($\omega_3 = \omega_2 - \omega_1$) between the frequencies of the two pump fields corresponds to the THz frequency.

Two external pump fields and generated THz difference frequency field are interacting with each other as they are propagating through a waveguide structure. The pump fields are decaying due to the free carrier absorption and the resonant absorption. Their contributions to the total absorption depend on the initial pump intensity and confinement factors of pump fields in specific waveguide structures. For qualitative understanding, one can derive an analytic expression for the THz power as shown in APPENDIX E; very weak and very strong pump power regimes. The former corresponds to the system which all populations are located in the ground subband. Since the population difference between the ground state and excited states is maximal in this case, the resonant absorption contributes dominantly than the free carrier absorption for pump fields. On the other hand, in the latter case, electrons are equally distributed over subbands, and it results in negligible resonant absorptions. Then, the major contribution to the total absorption comes from the free carrier absorption. In both

cases, the resonant absorption of THz field becomes negligible because of nearly zero population difference between E_2 and E_3, and the linear susceptibility becomes nearly zero.

In reality, the initial intensities of the pump fields and their varying amplitudes upon propagation modify the strength to excite electrons to upper states. A stronger dipole moment and pump intensity between two states and longer relaxation time in the upper state better push up electrons to the excited state. If the pumping frequency is off-resonant with some detunings, then pumping strength is diminished. In this way, free electrons supplied by doping are redistributed over the subband levels, modifying the band edge profiles at the same time. Consequently, the electronic states of a multiple quantum well structure are modified along with dipole moments and relaxation rates. These changes influence back to the subband electron density. This response of the medium to the external pump fields can be represented by optical susceptibilities. Particularly, the imaginary part of the linear susceptibility is proportional to the resonant absorption of propagating fields. Then, the intensity of pump fields is reduced by the absorption, and subsequently the above process is circulated (see Fig. 4-1). Externally pumped THz DFG system inherently possesses such extreme complication, and the problem is highly nonlinear. Therefore, to correctly predict the performance of THz DFG devices, the system should be dealt by the self-consistent approach in a rigorous way.

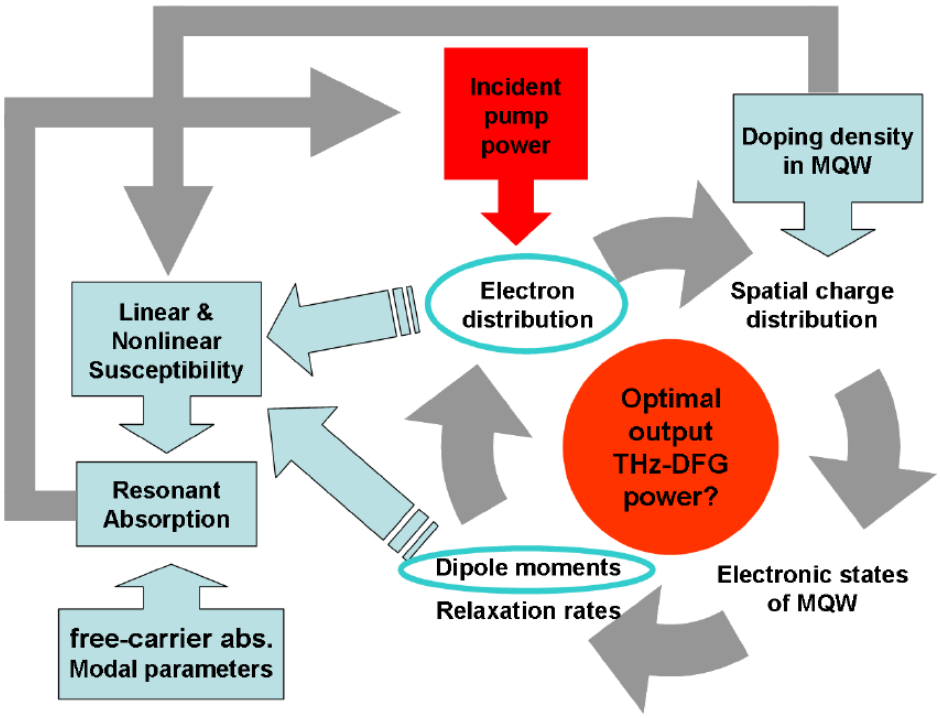

Fig. 4-1. The complexity of THz DFG system. Multiple quantum well (MQW) electronic states respond to external pump fields in a complicated way. The responses are represented by the optical susceptibilities, which provide the source of pump power depletion as well as THz field generation.

As shown in Fig. 4-2, the procedure of the self-consistent calculation for THz DFG is the following: first, electronic states are found in the flat one band model with nonparabolicity described by Eq. (4.1), which provides a good approximation near the Γ-point of the conduction band structure.

$$\frac{1}{m^*(E,z)} = 1 + 2F + \frac{E_p(z)}{3}\left(\frac{2}{E_g(z)+E-LH_s(z)-\phi_E} + \frac{1}{E_g(z)+\Delta_0(z)+E-SO_s(z)-\phi_E}\right)$$

$$+\frac{E_p(z)}{3}\left(\frac{4Q_\varepsilon(z)}{\left(E_g(z)+E-LH_s(z)-\phi_E\right)\left(E_g(z)+E+\Delta_0(z)-SO_s(z)-\phi_E\right)}\right) \qquad (4.1)$$

where

$$Q_{\varepsilon} = -\frac{b}{2}\left(e_{xx} + e_{yy} - 2e_{zz}\right)$$

$$e_{xx} = \frac{a_c(bottom) - a_c(top)}{a_c(top)}$$

$$e_{zz} = -\frac{2C_{12}}{C_{11}}\varepsilon_{xx}$$

and E_p is the interband matrix element between the conduction band and the valence band, F is the Kane parameter, E_g is the band gap, LH_s and SO_s are the light hole and the spin-orbit band edge shifts due to strain respectively, ϵ_{ij} is the strain tensor, a_c is the hydrostatic deformation potentials, C_{ij} is the elastic constant, and E is the subband eigen-energies in a heterostructure. (2) has been derived from the 8-band k • p model [15] based on the second order perturbation theory with the spin degeneracy and the in-plane momentum $k_{||} = 0$.

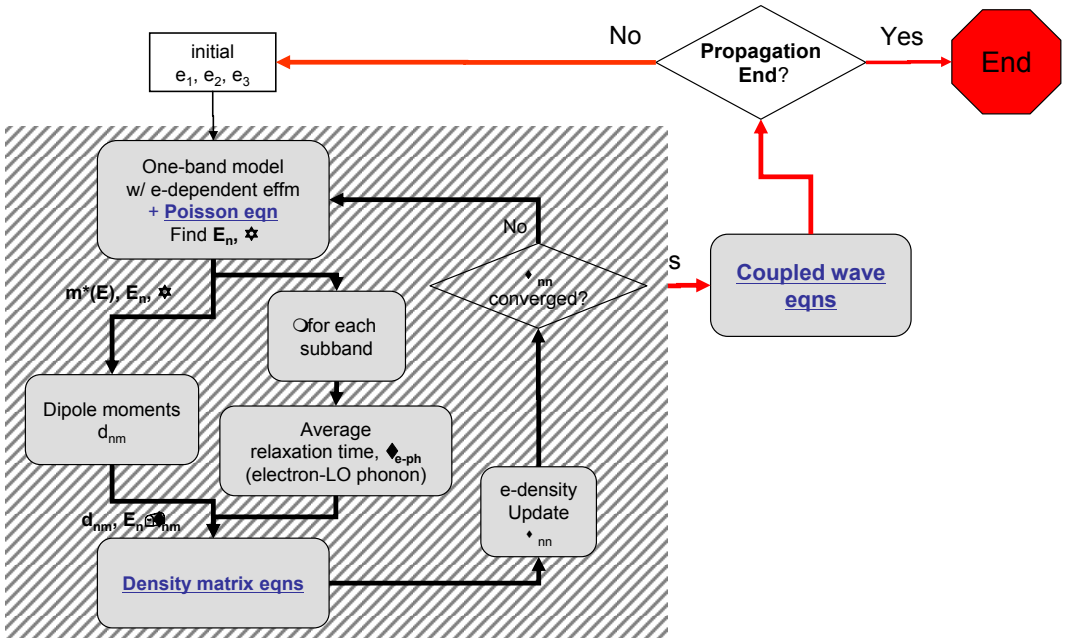

Fig. 4-2. The flow diagram of the self-consistent calculation for THz DFG. It incorporates the Poisson equation, the density matrix equation, and the coupled wave equation in a unified way. The updated field amplitudes affect subband populations. Sequentially optical susceptibilities, band edge profiles, dipole moments, and relaxation times are updated.

Then, the free carriers in a ground state are spatially redistributed by fulfilling the charge neutrality through solving the Poisson equation [136] until reaching the equilibrium of subband level positions. It modifies the band edge profiles over the sample growth direction or the confinement direction. Next, the subband levels and envelope functions are utilized to obtain dipole moments and relaxation rates [140, 141], which depend on the separation of energy levels, the overlap of envelope functions, and electron distributions. Particularly, the latter is obtained by averaging over occupied and unoccupied momentum vectors between subbands with the Fermi-Dirac distribution. After that, they become input parameters together with given initial amplitudes of

coupled fields in the density matrix equation (APPENDIX E) [142, 143], and all subband populations are obtained in the effective three level medium. The above sequence over the Poisson equation and the density matrix equation is repeated until the subband electron densities are reached to equilibrium. Once it is done, the three coupled first order differential equations for the fields (A. 37) ~ (A. 39) are solved for the next propagating coordinate, resulting in updated amplitude of the coupled fields. All of the above procedures are continuously repeated until the last propagating coordinate is reached.

The populations in the three subband levels correspond to the diagonal components of a 3×3 density matrix, found by solving nine algebraic coupled density matrix equations (see APPENDIX E). The off-diagonal components are related to the polarization field as shown in (E.9). However, they can not be directly used since the polarization fields are affected by the confinement factors and the nonlinear overlap integral of coupled fields for specific waveguide structures. Accordingly, each off-diagonal element should be re-expressed by expanding the polarization field in terms of susceptibilities, as shown in (E.11).

All non-zero propagating coordinate-dependent linear and nonlinear susceptibilities, affected by the variation of subband populations averaged over the sample growth direction, have been derived in (E.20) ~ (E.33). They are proportional to the doping density in the nonlinear region, assuming that all donor impurities are ionized and produce free carriers. The linear susceptibility is responsible for varying resonant absorptions of the fields in the propagation direction, and the second order term among

the non-zero nonlinear susceptibilities has the major contribution to the conversion of pump fields to THz DFG field. The linear and the second order optical responses are actual sources of the variation of propagating coupled fields amplitudes. The susceptibilities higher than the second order have negligible effects on both pump laser fields and THz DFG. Also, the band edge profile is influenced by the variation of subband populations upon the propagation of pump fields, and the modification of dipole moments and relaxation rates are accompanied due to the change of electronic states. But they are weak enough to be neglected.

4.3 Waveguides

We consider a simple ridge waveguide structure, and the stacked layer sequence is shown in Fig. 4-3. The nonlinear region, consisting of $GaIn_{0.52}As_{0.48}/AlIn_{0.53}As_{0.47}$ multiple quantum well, is sandwiched between 0.4 μm-thick highly doped InP contact layer ($N = 2\times 10^{18}$ cm^{-3}) on the top and 1.2 μm-thick InP cladding layer on the bottom. The cladding layer is located right above InP substrate. The gold is used for the metal contact, and Si_3N_4 is used for coating material.

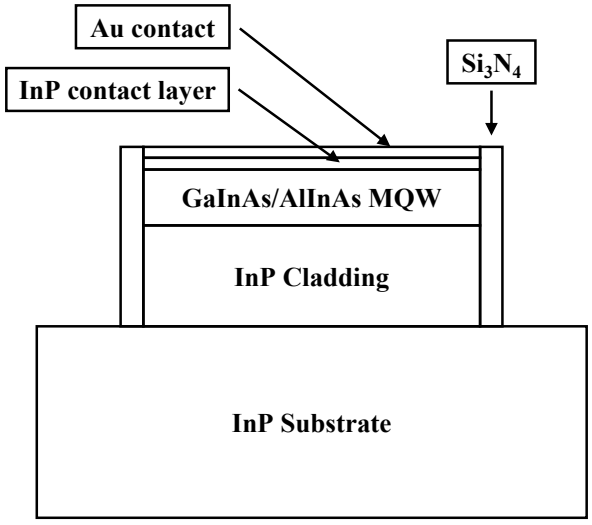

Fig. 4-3. The cross section of a schematic ridge waveguide structure for passive THz DFG with 60 μm-width. The nonlinear region, which consists of multiple periods of GaInAs/AlInAs double quantum wells shown in Fig. 4-4, is followed on the lightly doped InP cladding which is positioned on the top of substrate. Highly doped 0.4 μm-thick InP contact layer and Au contact are sequentially stacked above the nonlinear region. Si_3N_4 is the coating material.

To accommodate the confined fundamental THz DFG mode in the nonlinear region with smooth mode profiles and to avoid its leakage into the substrate, the material refractive indices are required to satisfy the following inequality based on COMSOL simulations for modes.

$$n\ (\text{NL region}) > n\ (\text{substrate}) > n\ (\text{contact layer})$$

By varying doping densities on each layer, this condition can be easily achieved. But it is ideal to minimize the doping density in the substrate [144] to prevent large absorptions of THz DFG mode.

Here, we vary the doping density as well as the thickness in the nonlinear region to investigate the various aspects of THz DFG conversion efficiency. Roughly speaking, when a doping density in a semiconductor becomes higher, the refractive index goes smaller based on the Drude model. Therefore, upon the variation of a doping density in the nonlinear region, one needs to properly modify the refractive index in the substrate by changing the doping density to make sure that a THz DFG mode is a surface-plasmon guiding mode [144] in the nonlinear section, not in the substrate. Here doping densities are changed from 0.7×10^{17} to 3×10^{17} cm^{-3} in the substrate depending on doping densities in the nonlinear region while approximately keeping the same level of refractive index difference among the highly doped InP contact layer, the GaInAs/AlInAs nonlinear region, and the InP substrate. The modal parameters of a 60 μm-wide and 4 μm-thick ridge waveguide, schematically shown in Fig. 4-3, are given in Table IV-1 with changing the average doping density in the nonlinear region.

The lightly doped cladding layer in the waveguide structure is critical for reducing the free carrier absorption of THz DFG mode, particularly when the thickness of the nonlinear region is reduced. Without the cladding layer, a THz DFG mode is extended into the substrate, and most of the mode resides in the substrate, in which the lower bound of the doping density is determined by the refractive index of the nonlinear region. This results in a huge free carrier absorption. Even in the waveguide structure which has a nonlinear region thick enough to encompass most of THz DFG mode, it is better to put a cladding layer since it also plays a role of reducing the free carrier

absorption although the reduction is not as dramatic as for the waveguide with a thin nonlinear region.

Table IV-1: Modal parameters of the ridge waveguide in Fig. 4-3 with varying average modulation-doping densities in the nonlinear region. For the confinement of fundamental THz DFG mode, the doping density in the substrate has been also changed to keep the same level of refractive index differences between the InP contact layer, the nonlinear region, and the substrate while keeping the inequality; n (NL region) > n (substrate) > n (contact layer).

	Average doping density (10^{17}cm^{-3})		
	0.25	0.5	1
Γ_{pump}	0.828	0.829	0.821
$\Gamma_{THz\ DFG}$	0.544	0.524	0.391
Γ	0.325	0.309	0.266
fca_{pump} (cm^{-1})	26.4	30.8	37.5
$fca_{THz\ DFG}$ (cm^{-1})	168	325	461
THz DFG mode cross section (μm^2)	150	180	270
Pump mode cross section (μm^2)	120	120	120

The free carrier absorption (fca) of THz radiation always gives a important contribution [115] to the total absorption of a field. It is generally true that as free carrier densities become larger in the regions where a mode is located, the free carrier absorption increases at the same time. Therefore, if the nonlinear region is highly doped

and thick, then the larger mode confinement leads to a larger free carrier absorption. The resonant absorption in the nonlinear region also has a similar dependence on the modal confinement.

The modal parameters with varying the thickness of the nonlinear region are given in Table IV-2. They are obtained by COMSOL for the 60 μm-wide ridge waveguide structure in Fig. 4-3 and a fixed average doping density N = 10^{17} cm^{-3} in the nonlinear region. Also, the doping densities in the cladding and the substrate are N = 7×10^{16} , and 1.8×10^{17} cm^{-3} respectively.

In the next section, we show the effect of resonant pump fields on electronic states of a quantum well heterostructure and a general trend of THz DFG output intensities in terms of incident pump intensities based on freely varying modal parameters regardless of specific waveguide structures and doping densities in the nonlinear region. Also, we investigate the dependence of THz DFG output powers from detunings, incident pump powers, and doping densities based on several specific waveguide structure parameters.

4.4 THz DFG Conversion Efficiency

The effects of incident pump fields on electronic states of a double quantum well (DQW) heterostructure (Fig. 4-4) are shown in Fig. 4-5 with neglecting the propagation of coupled fields. The subband energy levels are compared between two cases; with and

without pumping by varying the modulation-doping density. The discrepancy between those two cases becomes larger when the average doping density increases. Both the doping density in the nonlinear region and the intensity of pump fields affect the electronic states of quantum well heterostructures. It is originated from the excitation of electrons to upper subbands. However, the variation of intersubband transition energies, caused by varying incident intensities of pump fields for given doping densities, can be neglected within the available power range of current mid-infrared quantum cascade laser sources. The dipole moments and relaxation rates of the DQW structure in Fig. 4-4 are given in Table IV-3.

Table IV-2: Modal parameters, obtained by COMSOL, for the 60 μm-wide ridge waveguide in Fig. 4-3 with a fixed average doping density N = 10^{17} cm^{-3} and varying the thickness of the nonlinear region. The doping densities in InP contact layer, cladding, and substrate are N = 2×10^{18}, 7×10^{16} , and 1.8×10^{17} cm^{-3} respectively. Throughout the paper, we assume that a quasi-phase matching between pump and THz DFG modes is achieved by proper choice of the waveguide dimensions or the grating structure of nonlinear region.

	Nonlinear section thickness (μm)		
	1	4	12
Γ_{pump}	0.12	0.821	0.982
$\Gamma_{THz\ DFG}$	0.146	0.391	0.643
Γ	0.054	0.266	0.229
fca_{pump} (cm^{-1})	29.5	37.5	19.5
$fca_{THz\ DFG}$ (cm^{-1})	393	461	530
THz-DFG cross section (μm^2)	210	270	350
Pump mode cross section (μm^2)	180	120	210

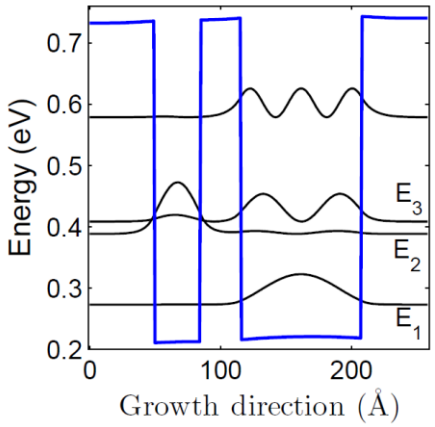

Fig. 4-4. $Ga_{0.47}In_{0.53}As/Al_{0.48}In_{0.52}As$ DQW structure for THz DFG. The resonant frequency of THz field corresponds to $E_{32} = E_3 - E_2$. The average modulation doping density is $N = 10^{17}$ cm^{-3}, and the intensity of pump fields is 2.3 MW/cm^2 with assuming a modal refractive index 3.2. The DQW layer sequence is 50/35/31/92/50, in which doping layers are underlined. The excitation of electrons due to pump fields has been taken into account.

Table IV-3: The dipole moments and relaxation rates of the DQW heterostructure shown in Fig. 4-4 obtained by the self-consistent calculation over the Poisson equation and the density matrix equation with using the average doping density $N = 10^{17}$ cm^{-3}.

	(ps^{-1})		(Å)
r_{12}	0	z_{12}	9.2
r_{13}	0	z_{13}	18.7
r_{21}	0.132	z_{23}	32.3
r_{31}	0.919		
r_{23}	0.01		
r_{32}	0.032		

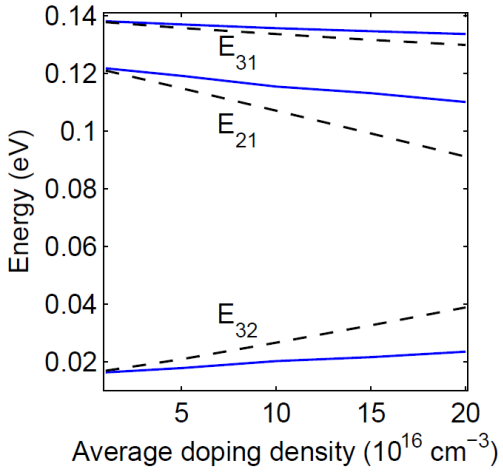

Fig. 4-5. The intersubband transition energies are varied as a function of average modulation-doping densities in the DQW structure shown in Fig. 4-4, and they are compared for two cases: (1) all electrons are located in the ground state (dashed). (2) electrons are distributed over excited states by pumping fields of intensity 2.3 MW/cm^2 and frequencies 120 and 140 meV, which are equal to E_{21} and E_{31} respectively. The discrepancy between those two cases becomes larger when the doping density becomes larger. No propagation effects are included.

Now we include the propagation of the coupled fields in the nonlinear medium which possesses the non-zero second order susceptibility. As the two incident pump fields, which have modified the electronic states of the DQW heterostructure, propagate along the waveguide with depletions, a THz-difference frequency field is generated and varies together with subband populations and the second order optical susceptibility as shown in Fig. 4-6, in which the average doping density in the nonlinear region is 10^{17}cm^{-3}, and the corresponding modal parameters used are shown in Table IV-1. The optimal waveguide length can be recognized to be about 27 μm for the specific waveguide structure and the doping density. The stronger depletion of the pump field resonant with E_{31} is occurred due to a stronger resonant absorption, originated from the nearly two

times larger dipole moment z_{31} than z_{21}, as well as a larger population difference N_{31} (= N_3 - N_1) than N_{21}. (see APPENDIX E) As a result of the pump field depletion upon propagation, the electron populations in the excited states are reduced, and this further increases the resonant absorption.

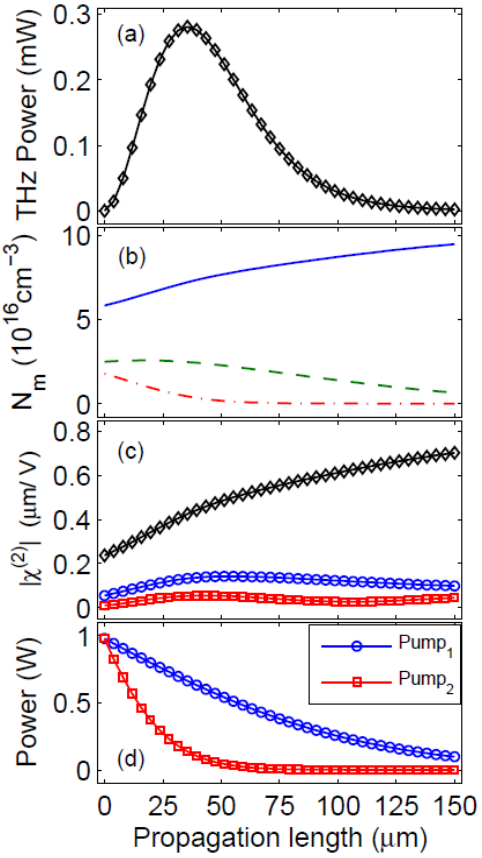

Fig. 4-6. As a function of propagation coordinate, (a) THz DFG output power, (b) subband populations (solid: ground, dashed: second, dash-dot: third subband level), (c) the second order optical susceptibility, and (d) two pump powers are shown. Here diamond, circle, and square indicate THz DFG field, and pump fields resonant with E_{21} and E_{31} respectively. The doping density in the nonlinear region is 10^{17}cm^{-3}, and the corresponding modal parameters are shown in Table IV-1.

THz DFG output powers also depend on incident pump powers as shown in Fig. 4-7, in which analytic solutions are compared with that obtained by the fully self-consistent calculation. The derivation for the former is given in APPENDIX E, and the THz DFG power can be expressed as (E.42) and (E.43). It is clear that THz DFG powers are quadratically increasing with respect to incident pump powers in the very weak pump power regime. On the other hand, in the very strong pump power regime, the analytic solution predicts that THz DFG powers decrease proportionally to the inverse square of incident pump powers.

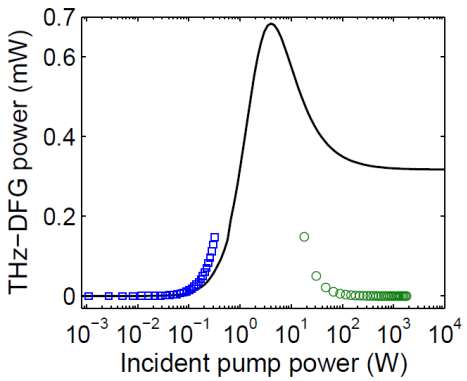

Fig. 4-7. Using the modal parameters corresponding to the average doping density of 10^{17} cm^{-3} in Table IV-1 and the waveguide length of 30 μm, THz DFG output powers obtained by two analytical limiting cases; very weak (square) and very strong (circle) pump fields, are compared with that by the fully self-consistent calculation (solid line).

THz DFG output powers can be affected by the variation of the doping density in the nonlinear region as shown in Fig. 4-8, in which all other parameters are fixed except for doping density. For incident pump powers less than 2 W, the THz DFG conversion efficiency is worst for the highest average doping density, $N=1 \times 10^{17}$ cm^{-3}, among the

three cases. However, the situation becomes opposite when the incident pump power becomes larger than 4 W. One should be aware that the optimal doping density in the nonlinear region is also affected by the modal parameters of waveguides. As shown in Fig. 4-9, in which the change of parameters such as the confinement factors and the overlap integrals affected by the doping density variation in the nonlinear region have been taken into account, the optimal average doping density is now $N = 0.25 \times 10^{17}$ cm^{-3} rather than $N = 0.5 \times 10^{17}$ cm^{-3} (see Fig. 4-8) at the input pump power of 1W. It can be mostly attributable to the lower free carrier absorption of the THz field.

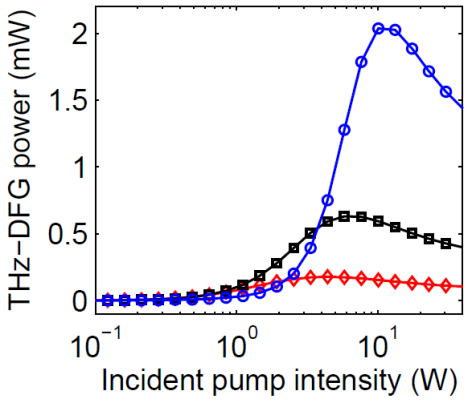

Fig. 4-8. THz DFG output power as a function of incident pump power for three different average doping densities (N) in the nonlinear region; N = 0.25 (diamond), 0.5 (square), and 1×10^{17} cm^{-3} (circle). All other parameters have been fixed, and modal parameters from Table IV-1, corresponding to average doping density 1×10^{17} cm^{-3} in the nonlinear region, are used. The ridge waveguide structure is assumed to be 100 μm-long. The conversion efficiencies at the peaks are 0.93, 1.87, and 2×10^{-5} W^{-1} for average doping densities N = 0.25 (diamond), 0.5 (square), and 1×10^{17} cm^{-3} (circle) respectively. In the simulation, the variation of other parameters which may occur due to the change of the doping density in the nonlinear region has not been taken into account. Figure 4-8 can be compared to Fig. 4-9, in which such approximation is not assumed.

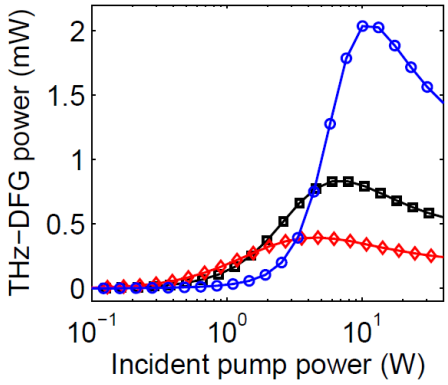

Fig. 4-9. THz DFG output power as a function of incident pump power for three different average doping densities (N) in the nonlinear region; N = 0.25 (diamond), 0.5 (square), and 1×10^{17} cm^{-3} (circle). The 4 μm-thick, 60 μm-wide, and 100 μm-long ridge waveguide structure is used. Contrary to Fig. 4-8, the change of modal parameters, affected by varying average doping density, has been taken into account. The modal parameters for each doping density are shown in Table IV-1.

The introduction of detunings in pump frequencies can increase the THz DFG output power when incident pump power is larger than a certain value, which is slightly larger than the power at saturation, as shown in Fig. 4-10. For the incident pump powers of 10.1 W (circle), the THz DFG output power is increased by ~ 18% or from 0.61 to 0.72 W at ~ 15 meV detuning, compared to zero detunings. However, for intermediate incident pump powers, zero detunings are the optimal condition for maximal THz DFG output power.

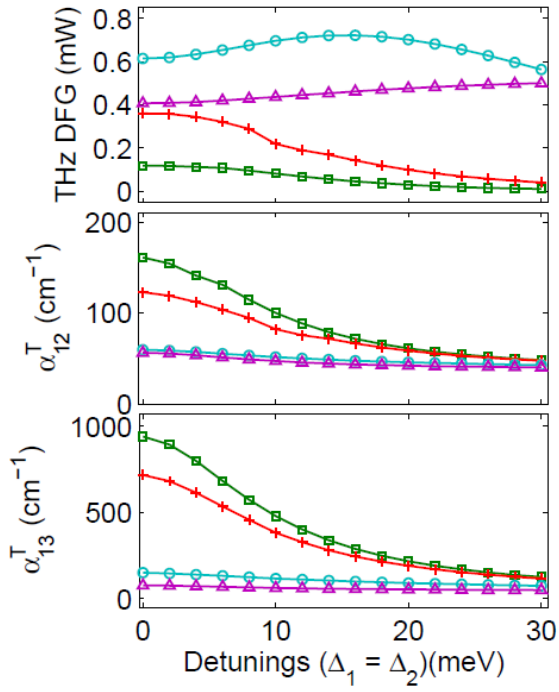

Fig. 4-10. THz power and the total absorptions of pump fields as a function of detunings are shown with four different incident pump powers; 0.5 (square), 1.1 (cross), 10.1 (circle), and 50 W (triangle). The 60 μm-wide and 30 μm-long ridge waveguide is used with the 4 μm-thick nonlinear region doped by N = 10^{17} cm^{-3} in average. The modal parameters are given in Table IV- 1.

Also, optimal waveguide lengths should be chosen depending on incident pump powers. In Fig. 4-11, the THz output power is shown for four different waveguide lengths with the fixed width of 60 μm, the nonlinear region thickness of 4 μm, and the average doping density of N = 10^{17} cm^{-3}. Its modal parameters are given in Table IV-1. When incident pump power becomes smaller, shorter waveguides perform better because the pump field experiences stronger absorption in longer waveguides.

For a given incident pump intensity, THz DFG output power as a function of waveguide length is shown in Fig. 4- 12 for two different doping densities in the nonlinear region.

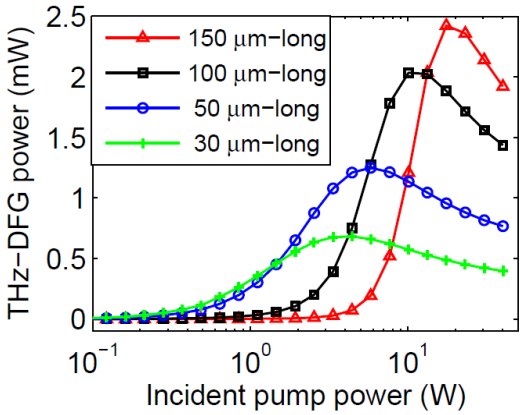

Fig. 4-11. THz DFG output power as a function of incident pump power is shown for four different waveguide lengths. The waveguide has the 4 μm-thick and 60 μm-wide nonlinear region doped with N = 10^{17} cm^{-3}, and the modal parameters are given in Table IV-1. When incident pump powers are smaller, shorter waveguides yield higher conversion efficiency.

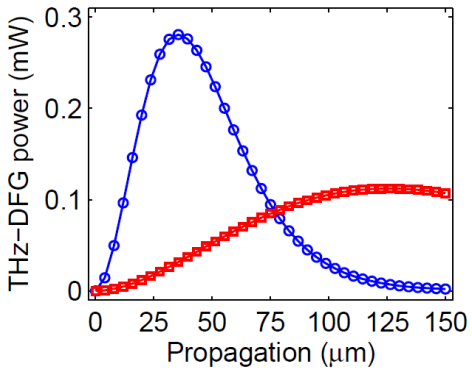

Fig. 4-12. THz DFG output power as a function of waveguide length for average doping densities N = 0.25 × 10^{17} cm^{-3} (square) and 1 × 10^{17} cm^{-3} (circle) in the 4 μm-thick nonlinear region. The incident pump power is ~ 1 W.

To see the general dependence of THz DFG output intensity as a function of incident pump intensity with varying modal parameters such as the confinement factors of coupled fields and the nonlinear overlap integral, we vary each of those parameters with all the other parameters fixed. Figure 4-13 (a, b) shows the dependence of the output THz DFG intensity and resonant absorption of the pump field Ω_2 (see Fig. 4-1) on incident pump intensities for three different confinement factors of pump fields in a 40 μm-long waveguide. For smaller confinement factors, input pump intensities are smaller to reach the same THz DFG intensity before the maximal peaks, which correspond to the values slightly larger than saturation intensity.

Figure 4-14 is obtained by using the same set of parameters as in Fig. 4-13 but with a 100 μm-long waveguide. The peak positions are shifted to higher incident pump intensities for the longer waveguide structure, compared to those in Fig. 4-13. According to Fig. 4-13 and Fig. 4-14, larger resonant absorptions of pump fields do not always mean smaller absolute output THz powers. The optimal confinement factors of pump fields depend on incident pump powers.

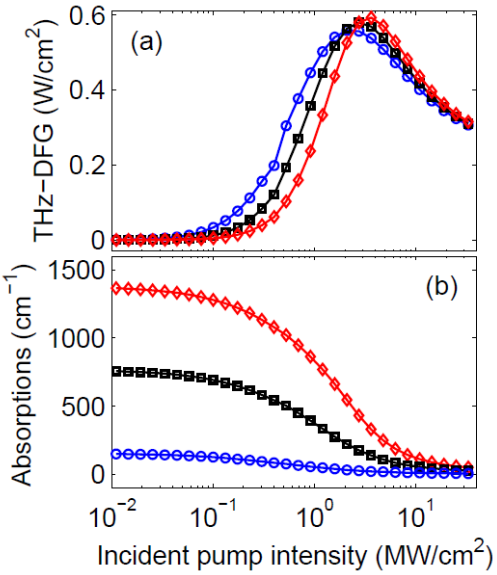

Fig. 4-13. (a) THz DFG output intensity as a function of incident pump intensity, (b) Resonant absorption of the pump field, which are nearly resonant with subband level difference E_{31} (= E_3 - E_1) in Fig. 4-4. For the constant confinement factor (Γ_{THz} = 0.1) of the THz DFG field and the nonlinear overlap integral equal to 0.01, the confinement factor (Γ_{pump}) of the pump fields is varied; Γ_{pump} = 0.1 (circle), Γ_{pump} = 0.5 (square), and Γ_{pump} = 0.9 (diamond), for a 40 μm-long waveguide with the average doping density of 10^{17}cm^{-3} in the nonlinear region. Here the constant free carrier absorptions of 30 and 460 cm^{-1} for pumps and THz DFG field are used respectively.

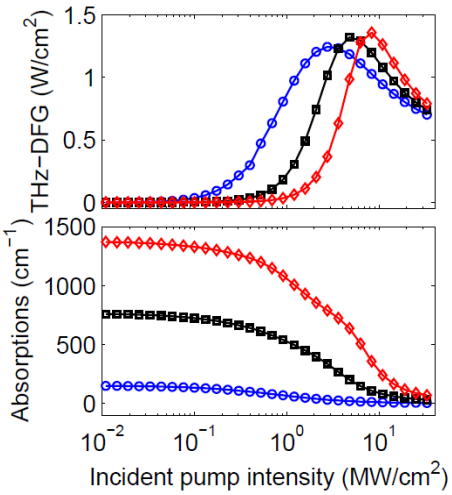

Fig. 4-14. THz DFG intensities and the resonant absorptions of Ω_2 as a function of incident pump intensity for three different confinement factors of the pump field Ω_2 with the same set of parameters except the waveguide length of 100 μm (see Fig. 4-13 for parameters).

The dependence of THz DFG output intensity on the nonlinear overlap integral is shown in Fig. 4-15. For larger values of the overlap integral, the THz DFG output intensity becomes stronger. This is the result well anticipated.

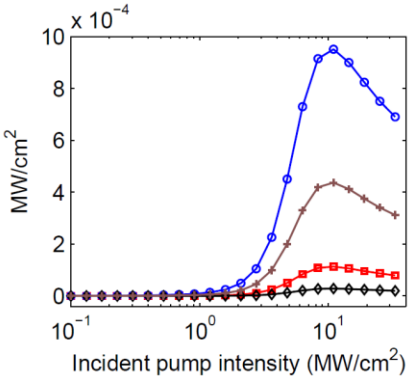

Fig. 4-15. THz DFG output intensity as a function of incident pump intensity for different values of the nonlinear overlap integral: 0.05 (diamond), 0.1 (square), 0.2 (cross), and 0.3 (circle). The other parameters are the same as in Fig. 4-11 for average doping density N = 10^{17}cm^{-3}.

An obvious way to obtain a large nonlinear overlap integral is to increase the thickness of the nonlinear region. Unfortunately it leads to increasing the confinement factors of all modes at the same time, which increases their absorptions. Also, a thicker nonlinear region requires using higher incident pump power to reach the same intensity. Therefore, there must be an optimal waveguide thickness. Figure 4-16 shows THz DFG powers in a 100-μm long waveguide for three different thicknesses of the nonlinear region. The conversion efficiencies for 1, 4, and 12 μm-thick nonlinear regions are 3×10^{-6}, 2×10^{-5}, and 3×10^{-6} W^{-1} respectively as shown in Fig. 4-16. The waveguide with the 4 μm-thick nonlinear region is best performing.

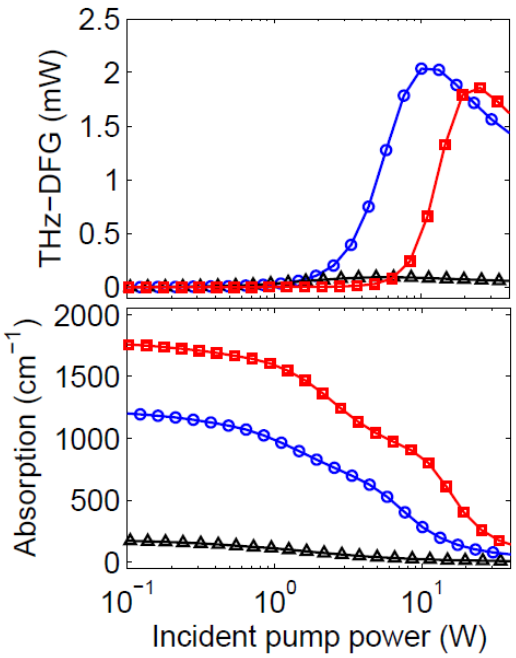

Fig. 4-16. THz DFG output powers and resonant absorptions as a function of incident pump intensity are shown for three different thicknesses (triangle: 1 μm, circle: 4 μm, square: 12 μm) of the nonlinear region in the 60 μm-wide and 100 μm-long ridge waveguide structure shown in Fig. 4-3. Their modal parameters are given in Table IV-2.

5. SUMMARY AND CONCLUSIONS[‡]

We presented a theoretical modeling of electronic, magnetic and optical properties of ferromagnetic GaMnAs using the mean-field Zener model and the 30- and 8-band k • p methods. Particularly, the 30-band k • p model allows us to simultaneously incorporate the modification of the valence band interaction with remote bands upon including the spin exchange interaction, epitaxial strain, the phenomenological Coulomb interaction, and disorder effect since the Luttinger parameters are not required. Also, the dielectric response tensor in the interband transition region is calculated over the whole first Brillouin zone. Our calculation of MOKE spectra of thin-film ferromagnetic GaMnAs samples in the metallic regime is in good qualitative agreement with the experimental spectra.

In the two dimensional heterostructure quantum system based on III-V binary and ternary compound semiconductors, new methodologies for finding eigensolutions has been proposed in the real space with three different approaches, so called, the delta function method (DFM), the Fourier grid Hamiltonian method (FGHM), and the modified version of the FGHM (MFGHM). They have been tested in the one-band, the 6-valence band, and the 8-band k • p models. The application of the methods can be extended to general *n*-band k • p models within the envelope function approximation.

[‡]Part of this section is reprinted from "Above-bandgap magneto-optical Kerr effect in ferromagnetic $Ga_{1-x}Mn_xAs$" by C. Sun, J. Kono, Y.-H. Cho, A. K. Wojcik, A. Belyanin, and H. Munekata, (2011), Physical Review B, 83, 125206, Copyright © 2011 by American Physical Society (APS).

The inherent advantages of the method include the treatment of the boundary conditions that are automatically satisfied, an extreme simplicity, transparency, the high accuracy of true eigen solutions, and the unified explanation and removal of spurious solutions.

Based on our self-consistent calculation incorporating electronic states of semiconductor multiple quantum well heterostructures and the propagation of coupled fields, we systematically characterized the THz DFG output power in passive devices, taking into account the variation of subband populations, incident pump powers, detunings, doping densities in the nonlinear region, dipole moments, waveguide geometry, and modal parameters. Once an incident pump power is chosen for a given device, all other parameters can be optimized to yield the highest THz power. Generally, the pump power of 1-3 W is enough to reach the highest conversion efficiency. We obtained approximately $\sim 10^{-3}$ W^{-1} in conversion efficiency and the milliwatt level of THz DFG output power at the incident pump power of ~ 1W.

REFERENCES

[1] H. Hellmann, J. Chem. Phys. **3**, 61 (1935).

[2] J. C. Phillips, Phys. Rev. **1**, 685 (1958).

[3] P. Lloyd, Proc. Phys. Soc. London **86**, 825 (1965).

[4] U. von Barth, and C. D. Gelatt, Phys. Rev. B **21**, 2222 (1980).

[5] Z. G. Zhu, T. Low, M. F. Li, W. J. Fan, P. Bai, D. L. Kwong, and G. Samudra, Semicond. Sci. Tech. **23** (2008).

[6] N. W. Ashcroft, and N. D. Mermin, *Solid State Physics* (Harcourt, Orlando, FL 1976).

[7] P. Y. Yu, and M. Cardona, *Fundamentals of Semiconductors* (Springer-Verlag, Berlin, 2001).

[8] G. B. Bachelet, D. R. Hamann, and M. Schlüter, Phys. Rev. B **26**, 4199 (1982).

[9] O. A. von Lilienfeld, I. Tavernelli, U. Rothlisberger, and D. Sebastiani, Phys. Rev. Lett. **93**, 153004 (2004).

[10] E. Fermi, Ricerca Scientifica 7, 13 (1936).

[11] D. M. Ceperley, and B. J. Alder, Phys. Rev. Lett. **45**, 566 (1980).

[12] P. Hohenberg, and W. Kohn, Phys. Rev. B **136**, B864 (1964).

[13] W. Kohn, and L. J. Sham, Phys. Rev. **140**, 1133 (1965).

[14] J. C. Slater, and G. F. Koster, Phys. Rev. **94**, 1498 (1954).

[15] G. L. Bir, and G. E. Pikus, *Symmetry and Strain-Induced Effects in Semiconductors* (John Wiley & Sons, Inc, New York, 1974).

[16] S. L. Chuang, *Physics of Optoelectronic Devices* (John Wiley & Sons, Inc., New York, 1995).

[17] J. M. Luttinger, and W. Kohn, Phys. Rev. **97**, 869 (1955).

[18] J. M. Luttinger, Phys. Rev. **102**, 1030 (1956).

[19] E. O. Kane, J. Phys. Chem. Solids **1**, 249 (1957).

[20] I. Vurgaftman, J. R. Meyer, and L. R. Ram-Mohan, J. Appl. Phys. **89**, 5815 (2001).

[21] C. Hermann, and C. Weisbuch, Phys. Rev. B **15**, 823 (1977).

[22] U. Rossler, Solid State Commun. **49**, 943 (1984).

[23] P. Pfeffer, and W. Zawadzki, Phys. Rev. B **41**, 1561 (1990).

[24] P. Pfeffer, and W. Zawadzki, Phys. Rev. B **53**, 12813 (1996).

[25] M. Cardona, P. Mcelroy, F. H. Pollak, and K. L. Shaklee, Solid State Commun. **4**, 319 (1966).

[26] M. Cardona, and F. H. Pollak, Phys. Rev. **142**, 530 (1966).

[27] F. H. Pollak, and M. Cardona, J. Phys. Chem. Solids **27**, 423 (1966).

[28] F. H. Pollak, C. W. Higginbotham, and M. Cardona, J. Phys. Soc. Japan **S 21**, 20 (1966).

[29] M. Cardona, N. E. Christensen, and G. Fasol, Phys. Rev. B **38**, 1806 (1988).

[30] N. Cavassilas, F. Aniel, eacute, ric, K. Boujdaria, and G. Fishman, Phys. Rev. B **64**, 115207 (2001).

[31] S. B. Radhia, S. Ridene, K. Boujdaria, H. Bouchriha, and G. Fishman, J. Appl. Phys. **92**, 4422 (2002).

[32] S. Ben Radhia, K. Boujdaria, S. Ridene, H. Bouchriha, and G. Fishman, J. Appl. Phys. **94**, 5726 (2003).

[33] O. Zitouni, K. Boujdariaa, and H. Bouchriha, Semicond. Sci. Tech. **20**, 908 (2005).

[34] S. Richard, F. Aniel, and G. Fishman, Phys. Rev. B **70**, 235204 (2004).

[35] S. Ben Radhia, N. Fraj, I. Saidi, and K. Boujdaria, Semicond. Sci. Tech. **22**, 427 (2007).

[36] N. Fraj, S. Ben Radhia, and K. Boujdaria, Solid State Commun. **142**, 342 (2007).

[37] N. Fraj, I. Saidi, S. Ben Radhia, and K. Boujdaria, J. Appl. Phys. **102**, 053703 (2007).

[38] N. Fraj, I. Saidi, S. Ben Radhia, and K. Boujdaria, Semicond. Sci. Tech. **23**, 085006 (2008).

[39] I. Saidi, S. Ben Radhia, and K. Boujdariaa, J. Appl. Phys. **104**, 023706 (2008).

[40] K. M. Yu, T. Wojtowicz, W. Walukiewicz, X. Liu, and J. K. Furdyna, in *Spintronics*, edited by T. Dietl *et al.* (Academic Press, New York, 2008).

[41] W. W. Chow, and S. W. Koch, *Semiconductor-Laser Fundamentals: Physics of the Gain Materials* (Springer, Berlin, 1999).

[42] R. Shankar, *Principles of Quantum Mechanics* (Springer, New York, 1994).

[43] H. Ohno, A. Shen, F. Matsukura, A. Oiwa, A. Endo, S. Katsumoto, and Y. Iye, Appl. Phys. Lett. **69**, 363 (1996).

[44] H. Munekata, H. Ohno, S. von Molnar, A. Segmüller, L. L. Chang, and L. Esaki, Phys. Rev. Lett. **63**, 1849 (1989).

[45] T. Dietl, H. Ohno, F. Matsukura, J. Cibert, and D. Ferrand, Science **287**, 1019 (2000).

[46] T. Dietl, H. Ohno, and F. Matsukura, Phys. Rev. B **6319**, 195205 (2001).

[47] T. Jungwirth, J. Sinova, A. H. MacDonald, B. L. Gallagher, V. Novak, K. W. Edmonds, A. W. Rushforth, R. P. Campion, C. T. Foxon, L. Eaves, E. Olejnik, J. Masek, S. R. E. Yang, J. Wunderlich, C. Gould, L. W. Molenkamp, T. Dietl, and H. Ohno, Phys. Rev. B **76**, 125206 (2007).

[48] J. Masek, F. Maca, J. Kudrnovsky, O. Makarovsky, L. Eaves, R. P. Campion, K. W. Edmonds, A. W. Rushforth, C. T. Foxon, B. L. Gallagher, V. Novak, J. Sinova, and T. Jungwirth, Phys. Rev. Lett. **105**, 227202 (2010).

[49] K. S. Burch, D. B. Shrekenhamer, E. J. Singley, J. Stephens, B. L. Sheu, R. K. Kawakami, P. Schiffer, N. Samarth, D. D. Awschalom, and D. N. Basov, Phys. Rev. Lett. **97**, 087208 (2006).

[50] P. R. Stone, K. Alberi, S. K. Z. Tardif, J. W. Beeman, K. M. Yu, W. Walukiewicz, and O. D. Dubon, Phys. Rev. Lett. **101**, 087203 (2008).

[51] K. Ando, H. Saito, K. C. Agarwal, M. C. Debnath, and V. Zayets, Phys. Rev. Lett. **100**, 067204 (2008).

[52] J.-M. Tang and M. E. Flatte, Phys. Rev. Lett. **101**, 157203 (2008).

[53] K. S. Burch, D. D. Awschalom, and D. N. Basov, J. Magn. Magn. Mater. **320**, 3207 (2008).

[54] J. K. Furdyna, and J. Kossut, *Diluted Magnetic Semiconductors* (Academic Press, Inc., San Diego, CA, 1988).

[55] K. T. Nam, S. Kuroda, T. Kumekawa, N. Ozaki, and K. Takita, Phys. Status Solidi B **241**, 668 (2004).

[56] M. Wang, R. P. Campion, A. W. Rushforth, K. W. Edmonds, C. T. Foxon, and B. L. Gallagher, Appl. Phys. Lett. **93**, 132103 (2008).

[57] K. W. Edmonds, P. Boguslawski, K. Y. Wang, R. P. Campion, S. N. Novikov, N. R. S. Farley, B. L. Gallagher, C. T. Foxon, M. Sawicki, T. Dietl, M. B. Nardelli, and J. Bernholc, Phys. Rev. Lett. **92**, 037201 (2004).

[58] L. X. Zhao, C. R. Staddon, K. Y. Wang, K. W. Edmonds, R. P. Campion, B. L. Gallagher, and C. T. Foxon, Appl. Phys. Lett. **86**, 071902 (2005).

[59] T. Jungwirth, J. Konig, J. Sinova, J. Kucera, and A. H. MacDonald, Phys. Rev. B **66**, 012402 (2002).

[60] J. Sinova, T. Jungwirth, S. R. E. Yang, J. Kucera, and A. H. MacDonald, Phys. Rev. B **66**, 041202 (2002).

[61] T. Jungwirth, J. Masek, J. Sinova, and A. H. MacDonald, Phys. Rev. B **68**, 041308(R) (2003).

[62] J. Sinova, T. Jungwirth, J. Kucera, and A. H. MacDonald, Phys. Rev. B **67**, 161202 (2003).

[63] S. R. E. Yang, J. Sinova, T. Jungwirth, Y. P. Shim, and A. H. MacDonald, Phys. Rev. B **67**, 045205 (2003).

[64] E. M. Hankiewicz, T. Jungwirth, T. Dietl, C. Timm, and J. Sinova, Phys. Rev. B **70**, 245211 (2004).

[65] J. Sinova, T. Jungwirth, X. Liu, Y. Sasaki, J. K. Furdyna, W. A. Atkinson, and A. H. MacDonald, Phys. Rev. B **69**, 085209 (2004).

[66] G. Acbas, M. H. Kim, M. Cukr, V. Novak, M. A. Scarpulla, O. D. Dubon, T. Jungwirth, J. Sinova, and J. Cerne, Phys. Rev. Lett. **103**, 137201 (2009).

[67] C. Zener, Phys. Rev. **81**, 440 (1951).

[68] K. Shinagawa, in *Magneto-Optics*, edited by S. Sugano, and N. Kojima (Springer, New York, 2000).

[69] W. R. Mason, *A Practical Guide to Magnetic Circular Dichroism Spectroscopy* (Wiley-Interscience, Hoboken, N.J., 2007).

[70] A. Y. Cho, and J. R. Arthur, Prog. Solid State Chem. **10**, 157 (1975).

[71] G. B. Stringfellow, *Organometallic vapor-phase epitaxy : theory and practice* (Academic Press, San Diego, CA, 1999).

[72] D. L. Smith, and C. Mailhiot, Phys. Rev. B **33**, 8345 (1986).

[73] R. Eppenga, M. F. H. Schuurmans, and S. Colak, Phys. Rev. B **36**, 1554 (1987).

[74] L. R. Ram-Mohan, K. H. Yoo, and R. L. Aggarwal, Phys. Rev. B **38**, 6151 (1988).

[75] Y. X. Liu, D. Z. Y. Ting, and T. C. McGill, Phys. Rev. B **54**, 5675 (1996).

[76] R. Winkler and U. Rössler, Phys. Rev. B **48**, 8918 (1993).

[77] W. Yang, and K. Chang, Phys. Rev. B **72**, 233309 (2005).

[78] T. Mei, J. Appl. Phys. **102**, 053708 (2007).

[79] A. T. Meney, B. Gonul, and E. P. O'Reilly, Phys. Rev. B **50**, 10893 (1994).

[80] F. Szmulowicz, Phys. Rev. B **54**, 11539 (1996).

[81] B. A. Foreman, Phys. Rev. B **56**, R12748 (1997).

[82] X. Cartoixa, D. Z. Y. Ting, and T. C. McGill, J. Appl. Phys. **93**, 3974 (2003).

[83] K. I. Kolokolov, J. Li, and C. Z. Ning, Phys. Rev. B **68**, 161308 (2003).

[84] F. Szmulowicz, Phys. Rev. B **71**, 245117 (2005).

[85] S. v Alfthan, F. Boxberg, K. Kaski, A. Kuronen, R. Tereshonkov, J. Tulkki, and H. Sakaki, Phys. Rev. B **72**, 045329 (2005).

[86] B. A. Foreman, Phys. Rev. B **75**, 235331 (2007).

[87] T. Ono, and K. Hirose, Phys. Rev. B **72**, 085115 (2005).

[88] P. Huang, and E. A. Carter, Annu. Rev. Phys. Chem. **59**, 261 (2008).

[89] S. R. White, and L. J. Sham, Phys. Rev. Lett. **47**, 879 (1981).

[90] W. Trzeciakowski, Phys. Rev. B **38**, 12493 (1988).

[91] D. L. Smith, and C. Mailhiot, Rev. Mod. Phys. **62**, 173 (1990).

[92] M. J. Godfrey, and A. M. Malik, Phys. Rev. B **53**, 16504 (1996).

[93] M. V. Kisin, B. L. Gelmont, and S. Luryi, Phys. Rev. B **58**, 4605 (1998).

[94] M. E. Pistol, J. Phys. Soc. Japan **71**, 1325 (2002).

[95] A. V. Rodina, A. Y. Alekseev, A. L. Efros, M. Rosen, and B. K. Meyer, Phys. Rev. B **65**, 125302 (2002).

[96] C. C. Marston, and G. G. Balint-Kurti, J. Chem. Phys. **91**, 3571 (1989).

[97] S.-I. Chu, Chem. Phys. Lett. **167**, 155 (1990).

[98] S. Adhikari, P. Dutta, and S. P. Bhattacharyya, Chem. Phys. Lett. **199**, 574 (1992).

[99] G. Yao, and S.-I. Chu, Phys. Rev. A **48**, 485 (1993).

[100] E. Fattal, R. Baer, and R. Kosloff, Phys. Rev. E **53**, 1217 (1996).

[101] F. Brau, and C. Semay, J. Comput. Phys. **139**, 127 (1998).

[102] J. Stare, and G. G. Balint-Kurti, J. Phys. Chem. A **107**, 7204 (2003).

[103] G. L. Carr, M. C. Martin, W. R. McKinney, K. Jordan, G. R. Neil, and G. P. Williams, Nature **420**, 153 (2002).

[104] M. A. Belkin, F. Capasso, A. Belyanin, D. L. Sivco, A. Y. Cho, D. C. Oakley, C. J. Vineis, and G. W. Turner, Nature Photonics **1**, 288 (2007).

[105] M. A. Belkin, F. Capasso, F. Xie, A. Belyanin, M. Fischer, A. Wittmann, and J. Faist, Appl. Phys. Lett. **92**, 201101 (2008).

[106] C. Pflügl, M. A. Belkin, Q. J. Wang, M. Geiser, A. Belyanin, M. Fischer, A. Wittmann, J. Faist, and F. Capasso, Appl. Phys. Lett. **93**, 161110 (2008).

[107] M. A. Belkin, Q. J. Wang, C. Pflugl, A. Belyanin, S. P. Khanna, A. G. Davies, E. H. Linfield, and F. Capasso, IEEE J. Sel. Top. Quantum Electron. **15**, 952 (2009).

[108] K. Kawase, T. Hatanaka, H. Takahashi, K. Nakamura, T. Taniuchi, and H. Ito, Opt. Lett. **25**, 1714 (2000).

[109] W. Shi, Y. J. Ding, N. Fernelius, and K. Vodopyanov, Opt. Lett. **27**, 1454 (2002).

[110] W. Shi, Y. J. Ding, and P. G. Schunemann, Opt. Commun. **233**, 183 (2004).

[111] C. Staus, T. Kuech, and L. McCaughan, Opt. Express **16**, 13296 (2008).

[112] C. Sirtori, F. Capasso, J. Faist, L. N. Pfeiffer, and K. W. West, Appl. Phys. Lett. **65**, 445 (1994).

[113] A. Liu, and C. Z. Ning, Appl. Phys. Lett. **75**, 1207 (1999).

[114] E. Dupont, Z. R. Wasilewski, and H. C. Liu, IEEE J. Quantum Electron., **42**, 1157 (2006).

[115] R. Köhler, A. Tredicucci, F. Beltram, H. E. Beere, E. H. Linfield, A. G. Davies, D. A. Ritchie, R. C. Iotti, and F. Rossi, Nature **417**, 156 (2002).

[116] L. Ajili, G. Scalari, N. Hoyler, M. Giovannini, and J. Faist, Appl. Phys. Lett. **87**, 141107 (2005).

[117] H. C. Liu, M. Wächter, D. Ban, Z. R. Wasilewski, M. Buchanan, G. C. Aers, J. C. Cao, S. L. Feng, B. S. Williams, and Q. Hu, Appl. Phys. Lett. **87**, 141102 (2005).

[118] A. Tredicucci, L. Mahler, T. Losco, J. Xu, C. Mauro, R. Köhler, H. E. Beere, D. A. Ritchie, and E. H. Linfield, Proc. SPIE Int. Soc. Opt. Eng. **5738**, 146 (2005).

[119] C. Walther, G. Scalari, J. Faist, H. Beere, and D. A. Ritchie, Appl. Phys. Lett. **89**, 231121 (2006).

[120] S. Kumar, B. S. Williams, Q. Qin, A. W. Lee, Q. Hu, and J. L. Reno, Opt. Express **15**, 113 (2007).

[121] C. Walther, M. Fischer, G. Scalari, R. Terazzi, N. Hoyler, and J. Faist, Appl. Phys. Lett. **91**, 131122 (2007).

[122] B. S. Williams, Nature **1**, 517 (2007).

[123] M. A. Belkin, J. A. Fan, S. Hormoz, F. Capasso, S. P. Khanna, M. Lachab, A. G. Davies, and E. H. Linfield, Opt. Express **16**, 3242 (2008).

[124] R. W. Boyd, *Nonlinear Optics* (Academic Press, San Diego, CA, 2003).

[125] M. Geiser, C. Pflugl, A. Belyanin, Q. J. Wang, N. F. Yu, T. Edamura, M. Yamanishi, H. Kan, M. Fischer, A. Wittmann, J. Faist, and F. Capasso, Optics Express **18**, 9900 (2010).

[126] J. R. Freeman, J. Madéo, A. Brewer, S. Dhillon, O. P. Marshall, N. Jukam, D. Oustinov, J. Tignon, H. E. Beere, and D. A. Ritchie, Appl. Phys. Lett. **96**, 051120 (2006).

[127] G. Scalari, C. Walther, J. Faist, H. Beere, and D. Ritchie, Appl. Phys. Lett. **88**, 141102 (2006).

[128] C. Gmachl, A. Belyanin, D. L. Sivco, M. L. Peabody, N. Owschimikow, A. M. Sergent, F. Capasso, and A. Y. Cho, IEEE J. Quantum Electron. **39**, 1345 (2003).

[129] Y.-H. Cho, and A. Belyanin, J. Appl. Phys **107**, 107 (2010).

[130] J. Okabayashi, A. Kimura, O. Rader, T. Mizokawa, A. Fujimori, T. Hayashi, and M. Tanaka, Phys. Rev. B **58**, R4211 (1998).

[131] J. Szczytko, W. Bardyszewski, and A. Twardowski, Phys. Rev. B **64**, 075306 (2001).

[132] S. C. Jain, J. M. Mcgregor, and D. J. Roulston, J. Appl. Phys. **68**, 3747 (1990).

[133] A. Aharoni, *Introduction to the Theory of Ferromagnetism* (Oxford University Press, New York, 1996).

[134] F. L. Pedrotti, and L. S. Pedrotti, *Introduction to Optics* (Prentice Hall, New York, 1993).

[135] R. Lang, A. Winter, H. Pascher, H. Krenn, X. Liu, and J. K. Furdyna, Phys. Rev. B **72**, 024430(2005).

[136] P. Harrison, *Quantum Wells, Wires and Dots* (John Wiley & Sons Ltd, West Sussex, U.K., 2005).

[137] G. B. Arfken, and H. J. Weber, *Mathematical Methods for Physicists* (Academic Press, San Diego, CA, 1995).

[138] U. Ekenberg, Phys. Rev. B **40**, 7714 (1989).

[139] K. H. Yoo, L. R. Ram-Mohan, and D. F. Nelson, Phys. Rev. B **39**, 12808 (1989).

[140] R. Ferreira, and G. Bastard, Phys. Rev. B **40**, 1074 (1989).

[141] C. Jacoboni, and P. Lugli, *The Monte Carlo Method for Semiconductor Device Simulation* (Spinger-Verlag, Wien, Austria, 1989).

[142] Y. I. Khanin, *Principles of Laser Dynamics* (Elsevier, New York, 1995).

[143] A. Belyanin, M. Troccoli, and F. Capasso, in *Intersubband Transitions in Quantum Structures*, edited by P. Roberto (McGraw-Hill, Blacklick, OH, 2006).

[144] S. Kohen, B. S. Williams, and Q. Hu, J. Appl. Phys. **97**, 053106 (2005).

APPENDIX A

THE 8×8 K • P HAMILTONIAN MATRIX [15]

In the non-relativistic limit, the Hamiltonian has the form as shown in (A.1), in which the spin-orbit interaction term is added to the Schrödinger equation and with bare electron mass *m*. The effect of the spin-orbit interaction becomes more pronounced for heavier semiconductors.

$$H_0 = \frac{\mathbf{p}^2}{2m} + V(x) + \frac{\hbar}{4m^2c^2}(\boldsymbol{\sigma} \times \nabla V) \bullet \mathbf{p} \tag{A.1}$$

After applying the Bloch wavefunction $\psi_{n\mathbf{k}} = \frac{1}{\sqrt{V}} e^{i\mathbf{k}\bullet\mathbf{r}} u_{n\mathbf{k}}$ on (A.1), only the periodic part of the Bloch function is left, cancelling the plane wave part in $H_0\psi_{n\mathbf{k}} = E_{n\mathbf{k}}\psi_{n\mathbf{k}}$. Consequently, it gives the *k*-dependent Hamiltonian as in (A.2) and $H_{\mathbf{k}}u_{n\mathbf{k}} = E_{n\mathbf{k}}u_{n\mathbf{k}}$.

$$H_{\mathbf{k}} = \frac{\mathbf{p}^2}{2m} + V(x) + \frac{\hbar^2k^2}{2m} + \frac{\hbar}{m}\mathbf{k} \bullet \mathbf{p} + \frac{\hbar}{4m^2c^2}(\boldsymbol{\sigma} \times \nabla V) \bullet \mathbf{p} + \frac{\hbar^2}{4m^2c^2}(\boldsymbol{\sigma} \times \nabla V) \bullet \mathbf{k} \tag{A.2}$$

$$= \frac{\mathbf{p}^2}{2m} + V(x) + \frac{\hbar}{4m^2c^2}(\boldsymbol{\sigma} \times \nabla V) \bullet \mathbf{p} + \frac{\hbar^2k^2}{2m} + \frac{\hbar}{m}\mathbf{k} \bullet \left[\mathbf{p} + \frac{\hbar^2}{4m^2c^2}(\boldsymbol{\sigma} \times \nabla V)\right] \tag{A.3}$$

Using the definition of $\boldsymbol{\pi} \equiv \mathbf{p} + \frac{\hbar^2}{4m^2c^2}(\boldsymbol{\sigma} \times \nabla V)$ and (A.1), then (A.3) is simplified as

$$H_{\mathbf{k}} = H_0 + \frac{\hbar^2k^2}{2m} + \frac{\hbar}{m}\mathbf{k} \bullet \boldsymbol{\pi} \tag{A.4}$$

Using the perturbation theory, $E_{n\mathbf{k}}$ and the periodic part of the Bloch function $u_{n\mathbf{k}}$ can be expanded up to the second order and the first order respectively with respect to small **k**. Using the zeroth order of the eight periodic parts (A.5) of the Bloch function that are determined by the symmetry of orbitals, corresponding to Γ_{6C}(CB), Γ_{8V}(HH, LH) and Γ_{7V}(SO) (the double point group notation) in the Γ symmetry point, in which the Kramer's degeneracy is taken into account, the resulting Hermitian Hamiltonian becomes the 8×8 **k** • **p** Hamiltonian as shown in (A.6). The higher bands that are cut off in this band model are effectively included in the second order terms through the Luttinger parameters $\gamma_{1,2,3}$ and the Kane parameter *F*.

$$\left|1/2,1/2\right\rangle_c = \left|S\uparrow\right\rangle,\ \left|1/2,-1/2\right\rangle_c = \left|S\downarrow\right\rangle,$$

$$\left|3/2,3/2\right\rangle = \frac{-i}{\sqrt{2}}\left|(X+iY)\uparrow\right\rangle,\ \left|3/2,-3/2\right\rangle = \frac{i}{\sqrt{2}}\left|(X-iY)\downarrow\right\rangle,$$

$$\left|3/2,1/2\right\rangle = \frac{i}{\sqrt{6}}\left[-\left|(X+iY)\downarrow\right\rangle + 2\left|Z\uparrow\right\rangle\right],\ \left|3/2,-1/2\right\rangle = i\left[\frac{1}{\sqrt{6}}\left|(X-iY)\uparrow\right\rangle + \sqrt{\frac{2}{3}}\left|Z\downarrow\right\rangle\right],$$

$$\left|1/2,1/2\right\rangle = i\left[\frac{1}{\sqrt{3}}\left|(X+iY)\downarrow\right\rangle + \sqrt{\frac{1}{3}}\left|Z\uparrow\right\rangle\right],\ \left|1/2,-1/2\right\rangle = \frac{i}{\sqrt{3}}\left[\left|(X-iY)\uparrow\right\rangle - \left|Z\downarrow\right\rangle\right]$$

(A.5)

$$H_{8\times8}=\begin{array}{c}\begin{matrix}\quad & (1/2,1/2) & (1/2,-1/2) & (3/2,3/2) & (3/2,1/2) & (3/2,-1/2) & (3/2,-3/2) & (1/2,1/2) & (1/2,-1/2)\end{matrix}\\ \begin{matrix}(1/2,1/2)\\(1/2,-1/2)\\(3/2,3/2)\\(3/2,1/2)\\(3/2,-1/2)\\(3/2,-3/2)\\(1/2,1/2)\\(1/2,-1/2)\end{matrix}\begin{pmatrix} E_g+\frac{\hbar^2k^2}{2m_0}(1+2F)+\phi_E & 0 & -Pk_+ & \sqrt{\frac{2}{3}}Pk_z & \frac{1}{\sqrt{3}}Pk_- & 0 & \frac{1}{\sqrt{3}}Pk_z & \sqrt{\frac{2}{3}}Pk_- \\ 0 & E_g+\frac{\hbar^2k^2}{2m_0}(1+2F)+\phi_E & 0 & \frac{-1}{\sqrt{3}}Pk_+ & \sqrt{\frac{2}{3}}Pk_z & Pk_- & \sqrt{\frac{2}{3}}Pk_+ & \frac{-1}{\sqrt{3}}Pk_z \\ -Pk_- & 0 & F'+\phi_E & H' & I' & 0 & \frac{H'}{\sqrt{2}} & \sqrt{2}I' \\ \sqrt{\frac{2}{3}}Pk_z & \frac{-1}{\sqrt{3}}Pk_- & H'^* & G'+\phi_E & 0 & I' & \frac{1}{\sqrt{2}}(G'-F') & -\sqrt{\frac{3}{2}}H' \\ \frac{1}{\sqrt{3}}Pk_+ & \sqrt{\frac{2}{3}}Pk_z & I'^* & 0 & G'+\phi_E & -H' & -\sqrt{\frac{3}{2}}H'^* & \frac{-1}{\sqrt{2}}(G'-F') \\ 0 & Pk_+ & 0 & I'^* & -H'^* & F'+\phi_E & -\sqrt{2}I'^* & \frac{1}{\sqrt{2}}H'^* \\ \frac{1}{\sqrt{3}}Pk_z & \sqrt{\frac{2}{3}}Pk_- & \frac{H'^*}{\sqrt{2}} & \frac{1}{\sqrt{2}}(G'^*-F'^*) & -\sqrt{\frac{3}{2}}H' & -\sqrt{2}I' & -\Delta+\frac{F'+G'}{2}+\phi_E & 0 \\ \sqrt{\frac{2}{3}}Pk_+ & \frac{-1}{\sqrt{3}}Pk_z & \sqrt{2}I'^* & -\sqrt{\frac{3}{2}}H'^* & -\frac{1}{\sqrt{2}}(G'^*-F'^*) & \frac{1}{\sqrt{2}}H' & 0 & -\Delta+\frac{F'+G'}{2}+\phi_E \end{pmatrix}\end{array} \tag{A.6}$$

where E_g is the band gap and Δ is the spin orbit split-off energy, ϕ_E is the potential energy due to an external electric field, $k_\pm=\left(1/\sqrt{2}\right)\left(k_x\pm ik_y\right)$, and other parameters are defined as follows;

$$F'=-\frac{\hbar^2}{2m_0}\left[(\gamma_1+\gamma_2)k_{||}^2+(\gamma_1-2\gamma_2)k_z^2\right],\quad G'=-\frac{\hbar^2}{2m_0}\left[(\gamma_1-\gamma_2)k_{||}^2+(\gamma_1+2\gamma_2)k_z^2\right],$$

$$H'=\frac{\hbar^2}{m_0}\sqrt{3}\gamma_3k_z\left(k_x-ik_y\right)=\frac{\hbar^2}{2m_0}2\sqrt{6}\gamma_3k_zk_-,\ I'=\frac{\hbar^2}{2m_0}\left[\sqrt{3}\gamma_2\left(k_x^2-k_y^2\right)-i2\sqrt{3}\gamma_3k_xk_y\right]$$

$$P=\frac{i\hbar}{m_0}\left\langle S\left|p_x\right|X\right\rangle\equiv\frac{i\hbar}{m_0}p_{SX}^x$$

$$\gamma_1=\gamma_1^L-\frac{2m_0}{3\hbar^2}\frac{P^2}{E_g},\ \gamma_{2,3}=\gamma_{2,3}^L-\frac{m_0}{3\hbar^2}\frac{P^2}{E_g},$$

where m_0 is the bare electron mass, $\hbar$ is the Plank constant, p_α is the α-component of the momentum, $k_{||}^2=k_x^2+k_y^2$, ε_0 is the band edge energy for corresponding band, originated from H_0 in (A.4), S is the *s*-like orbital and the linear combination of X, Y, and Z is the *p*-like orbital, ε_{rc} and ε_r represent all CB edge energies higher than the first CB and all remote band edge energies respectively.

In the Luttinger parameters $\gamma_{1,2,3}^{L}$, the free carrier energy term $\hbar^2 k^2 / 2m_0$ in (A.4) is already included. Since the CB is explicitly included in the band model, its contributions are subtracted from the Luttinger parameters $\gamma_{1,2,3}^{L}$, giving the modified Luttinger parameters $\gamma_{1,2,3}$.

$$\gamma_1^L = -1 - \frac{2}{3m_0}\sum_r \frac{p_{Xr}^x p_{rX}^x}{\varepsilon_0 - \varepsilon_r} - \frac{4}{3m_0}\sum_r \frac{p_{Xr}^y p_{rX}^y}{\varepsilon_0 - \varepsilon_r},$$

$$\gamma_2^L = -\frac{1}{3m_0}\left(\sum_r \frac{p_{Xr}^x p_{rX}^x}{\varepsilon_0 - \varepsilon_r} - \sum_r \frac{p_{Xr}^y p_{rX}^y}{\varepsilon_0 - \varepsilon_r}\right),$$

$$\gamma_3^L = -\frac{1}{3m_0}\left(\sum_r \frac{p_{Xr}^x p_{rX}^x + p_{Yr}^y p_{rY}^y}{\varepsilon_0 - \varepsilon_r}\right)$$

APPENDIX B

THE *s,p-d* SPIN EXCHANGE HAMILTONIAN MATRIX IN THE 8-BAND BASIS

Based on the virtual crystal approximation [54], the spin exchange interaction Hamiltonian can be written as (also see (2.3)).

$$H_{ex}^{s,p-d} = \sum_n J(\mathbf{r}-\mathbf{R}_n)\mathbf{S}_n \cdot \mathbf{s} \approx J_{s,p-d} N_0 x(\mathbf{s}\cdot\mathbf{S}) = \frac{J_{s,p-d}}{g_{Mn}\mu_B}(\mathbf{s}\cdot\mathbf{M}) = \frac{J_{s,p-d}}{g_{Mn}\mu_B}\left(\hat{s}_x M_x + \hat{s}_y M_y + \hat{s}_z M_z\right) \tag{B.1}$$

where n denotes Mn sites, $J_{s,p-d}$ is *s,p-d* spin exchange coupling constant, N_0 is Ga concentration, $\mathbf{M} = N_0 x g_{Mn}\mu_B \mathbf{S}$ [54], μ_B is Bohr magneton, g_{Mn} is 2, , S is 5/2 in III-Mn-V, **s** is free carrier spin vector, and x is Mn nominal fraction.

To obtain the Hamiltonian matrix, we take the inner product of (B.1), $\left\langle J, m_J \left| H_{ex}^{s,p-d} \right| J', m_J' \right\rangle$, by using the Bloch basis functions $\left| J, m_J \right\rangle$ of the 8-band k • p model as given in APPENDIX A and the Pauli matrix for free carrier spin, i.e.,

$$\hat{s}_x = \frac{1}{2}\hat{\sigma}_x = \frac{1}{2}\begin{pmatrix} 0 & 1 \\ 1 & 0 \end{pmatrix},\ \hat{s}_y = \frac{1}{2}\hat{\sigma}_y = \frac{1}{2}\begin{pmatrix} 0 & -i \\ i & 0 \end{pmatrix},\ \hat{s}_z = \frac{1}{2}\hat{\sigma}_z = \frac{1}{2}\begin{pmatrix} 1 & 0 \\ 0 & -1 \end{pmatrix}$$

For example, the spin operator acted on spin-up or spin down states can be calculated as

$$\left\langle \uparrow \left| \hat{s}_x \right| \uparrow \right\rangle = \frac{1}{2}\left\langle \uparrow \left| \hat{\sigma}_x \right| \uparrow \right\rangle = \frac{1}{2}\begin{pmatrix} 1 & 0 \end{pmatrix}\begin{pmatrix} 0 & 1 \\ 1 & 0 \end{pmatrix}\begin{pmatrix} 1 \\ 0 \end{pmatrix} = 0\ ,$$

$$\left\langle \downarrow \left| \hat{s}_x \right| \uparrow \right\rangle = \frac{1}{2}\left\langle \downarrow \left| \hat{\sigma}_x \right| \uparrow \right\rangle = \frac{1}{2}\begin{pmatrix} 0 & 1 \end{pmatrix}\begin{pmatrix} 0 & 1 \\ 1 & 0 \end{pmatrix}\begin{pmatrix} 1 \\ 0 \end{pmatrix} = \frac{1}{2}$$

First of all, for the projection on the *x*-direction of the magnetization, the Hamiltonian matrix becomes

$$\left\langle J, m_J \left| \hat{s}_x M_x \right| J', m_J' \right\rangle = M_x \left\langle J, m_J \left| \hat{s}_x \right| J', m_J' \right\rangle =$$

	$(1/2,1/2)$	$(1/2,-1/2)$	$(3/2,3/2)$	$(3/2,1/2)$	$(3/2,-1/2)$	$(3/2,-3/2)$	$(1/2,1/2)$	$(1/2,-1/2)$
$(1/2,1/2)$	0	$\frac{1}{2}M_x$	0	0	0	0	0	0
$(1/2,-1/2)$	$\frac{1}{2}M_x$	0	0	0	0	0	0	0
$(3/2,3/2)$	0	0	0	$\frac{i}{2\sqrt{3}}M_x$	0	0	$\frac{1}{\sqrt{6}}M_x$	0
$(3/2,1/2)$	0	0	$-\frac{i}{2\sqrt{3}}M_x$	0	$\frac{i}{3}M_x$	0	0	$-\frac{1}{3\sqrt{2}}M_x$
$(3/2,-1/2)$	0	0	0	$-\frac{i}{3}M_x$	0	$\frac{i}{2\sqrt{3}}M_x$	$\frac{1}{3\sqrt{2}}M_x$	0
$(3/2,-3/2)$	0	0	0	0	$-\frac{i}{2\sqrt{3}}M_x$	0	0	$-\frac{1}{\sqrt{6}}M_x$
$(1/2,1/2)$	0	0	$\frac{1}{\sqrt{6}}M_x$	0	$\frac{1}{3\sqrt{2}}M_x$	0	0	$\frac{i}{6}M_x$
$(1/2,-1/2)$	0	0	0	$-\frac{1}{3\sqrt{2}}M_x$	0	$-\frac{1}{\sqrt{6}}M_x$	$-\frac{i}{6}M_x$	0

In the similar fashion, the Hamiltonian matrices for the rest of projection directions can be obtained as follows:

$$M_y \left\langle J, m_J \left| \hat{s}_y \right| J', m_J' \right\rangle =$$

	$(1/2,1/2)$	$(1/2,-1/2)$	$(3/2,3/2)$	$(3/2,1/2)$	$(3/2,-1/2)$	$(3/2,-3/2)$	$(1/2,1/2)$	$(1/2,-1/2)$
$(1/2,1/2)$	0	$-\frac{i}{2}M_y$	0	0	0	0	0	0
$(1/2,-1/2)$	$\frac{i}{2}M_y$	0	0	0	0	0	0	0
$(3/2,3/2)$	0	0	0	$\frac{1}{2\sqrt{3}}M_y$	0	0	$-\frac{i}{\sqrt{6}}M_y$	0
$(3/2,1/2)$	0	0	$\frac{1}{2\sqrt{3}}M_y$	0	$\frac{1}{3}M_y$	0	0	$\frac{i}{3\sqrt{2}}M_y$
$(3/2,-1/2)$	0	0	0	$\frac{1}{3}M_y$	0	$\frac{1}{2\sqrt{3}}M_y$	$\frac{i}{3\sqrt{2}}M_y$	0
$(3/2,-3/2)$	0	0	0	0	$\frac{1}{2\sqrt{3}}M_y$	0	0	$-\frac{i}{\sqrt{6}}M_y$
$(1/2,1/2)$	0	0	$\frac{i}{\sqrt{6}}M_y$	0	$-\frac{i}{3\sqrt{2}}M_y$	0	0	$\frac{1}{6}M_y$
$(1/2,-1/2)$	0	0	0	$-\frac{i}{3\sqrt{2}}M_y$	0	$\frac{i}{\sqrt{6}}M_y$	$\frac{1}{6}M_y$	0

and

$M_z \langle J, m_J | \hat{s}_z | J', m_J' \rangle =$

	$(1/2,1/2)$	$(1/2,-1/2)$	$(3/2,3/2)$	$(3/2,1/2)$	$(3/2,-1/2)$	$(3/2,-3/2)$	$(1/2,1/2)$	$(1/2,-1/2)$
$(1/2,1/2)$	$\frac{1}{2}M_z$	0	0	0	0	0	0	0
$(1/2,-1/2)$	0	$-\frac{1}{2}M_z$	0	0	0	0	0	0
$(3/2,3/2)$	0	0	$\frac{1}{2}M_z$	0	0	0	0	0
$(3/2,1/2)$	0	0	0	$\frac{1}{6}M_z$	0	0	$\frac{i\sqrt{2}}{3}M_z$	0
$(3/2,-1/2)$	0	0	0	0	$-\frac{1}{6}M_z$	0	0	$\frac{-i\sqrt{2}}{3}M_z$
$(3/2,-3/2)$	0	0	0	0	0	$-\frac{1}{2}M_z$	0	0
$(1/2,1/2)$	0	0	0	$\frac{-i\sqrt{2}}{3}M_z$	0	0	$-\frac{1}{6}M_z$	0
$(1/2,-1/2)$	0	0	0	0	$\frac{i\sqrt{2}}{3}M_z$	0	0	$\frac{1}{6}M_z$

The above three matrices can be combined to a single compact expression by using the spherical coordinates for the magnetization direction with respect to the crystal axis, i.e.,

$$M_{\pm} = M_x \pm iM_y = M \sin\theta\, e^{\pm i\phi}$$

$$M_x = M \sin\theta \cos\phi$$

$$M_y = M \sin\theta \sin\phi$$

$$M_z = M \cos\theta$$

where θ and ϕ indicate the polar and azimuthal angles for crystal axes respectively. The resulting Hamiltonian matrix is read as

$$\frac{J_{s,p-d}}{g_{Mn}\mu_B}\langle J, m_J | \left(\hat{s}_x M_x + \hat{s}_y M_y + \hat{s}_z M_z\right) | J', m_J' \rangle =$$

$$\frac{J_{pd}}{g_{Mn}\mu_B} M \times \begin{array}{c|cccccccc} & (1/2,1/2) & (1/2,-1/2) & (3/2,3/2) & (3/2,1/2) & (3/2,-1/2) & (3/2,-3/2) & (1/2,1/2) & (1/2,-1/2) \\ (1/2,1/2) & \frac{J_{sd}}{J_{pd}}\frac{1}{2}\cos\theta & \frac{J_{sd}}{J_{pd}}\frac{1}{2}\sin\theta\, e^{-i\phi} & 0 & 0 & 0 & 0 & 0 & 0 \\ (1/2,-1/2) & \frac{J_{sd}}{J_{pd}}\frac{1}{2}\sin\theta\, e^{i\phi} & -\frac{J_{sd}}{J_{pd}}\frac{1}{2}\cos\theta & 0 & 0 & 0 & 0 & 0 & 0 \\ (3/2,3/2) & 0 & 0 & \frac{1}{2}\cos\theta & \frac{i}{2\sqrt{3}}\sin\theta\, e^{-i\phi} & 0 & 0 & \frac{1}{\sqrt{6}}\sin\theta\, e^{-i\phi} & 0 \\ (3/2,1/2) & 0 & 0 & -\frac{i}{2\sqrt{3}}\sin\theta\, e^{i\phi} & \frac{1}{6}\cos\theta & \frac{i}{3}\sin\theta\, e^{-i\phi} & 0 & \frac{i\sqrt{2}}{3}\cos\theta & -\frac{1}{3\sqrt{2}}\sin\theta\, e^{-i\phi} \\ (3/2,-1/2) & 0 & 0 & 0 & -\frac{i}{3}\sin\theta\, e^{i\phi} & -\frac{1}{6}\cos\theta & \frac{i}{2\sqrt{3}}\sin\theta\, e^{-i\phi} & \frac{1}{3\sqrt{2}}\sin\theta\, e^{i\phi} & \frac{-i\sqrt{2}}{3}\cos\theta \\ (3/2,-3/2) & 0 & 0 & 0 & 0 & -\frac{i}{2\sqrt{3}}\sin\theta\, e^{i\phi} & -\frac{1}{2}\cos\theta & 0 & -\frac{1}{\sqrt{6}}\sin\theta\, e^{i\phi} \\ (1/2,1/2) & 0 & 0 & \frac{1}{\sqrt{6}}\sin\theta\, e^{i\phi} & \frac{-i\sqrt{2}}{3}\cos\theta & \frac{1}{3\sqrt{2}}\sin\theta\, e^{-i\phi} & 0 & -\frac{1}{6}\cos\theta & \frac{i}{6}\sin\theta\, e^{-i\phi} \\ (1/2,-1/2) & 0 & 0 & 0 & -\frac{1}{3\sqrt{2}}\sin\theta\, e^{i\phi} & \frac{i\sqrt{2}}{3}\cos\theta & -\frac{1}{\sqrt{6}}\sin\theta\, e^{-i\phi} & -\frac{i}{6}\sin\theta\, e^{i\phi} & \frac{1}{6}\cos\theta \end{array}$$

APPENDIX C

DERIVATION OF THE HELMHOLTZ FREE ENERGY

In the thermal-pressure reservoir of the canonical ensemble, the Gibbs free energy is given as

$$G = U - TS + PV \tag{C.1}$$

$$\begin{cases} F = U - TS \\ G = \mu N \end{cases} \tag{C.2}$$

where G is Gibbs free energy, U is internal energy, T is temperature, S is entropy, P is pressure, V is volume, μ is Chem. potential, N is the number of particles, and F is Helmholtz free energy.

By using (C.1) and (C.2), the Helmholtz free energy F can be re-expressed as

$$F = -PV + \mu N \tag{C.3}$$

And in the canonical ensemble, the product of pressure and volume can be written as

$$PV = k_B T \sum_i \ln\left(1 + e^{-\beta(\varepsilon_i - \mu)}\right) = k_B T \int d\varepsilon \; N(\varepsilon) \ln\left(1 + e^{-\beta(\varepsilon_i - \mu)}\right) \tag{C.4}$$

where k_B is the Boltzman constant, β is $1/k_B T$. By substituting (C.4) into (C.3) and replacing the notations $\mu \to \varepsilon_F$ and $N \to p$, in which it is assumed that the temperature is low enough to be neglected, and p stands for hole density. Then, (C.3) becomes

$$F = -k_B T \int d\varepsilon \; N(\varepsilon) \ln\left(1 + e^{-\beta(\varepsilon_i - \varepsilon_F)}\right) + \varepsilon_F p \tag{C.5}$$

In the limit of strong degeneracy, i.e., $1 << e^{-\beta(\varepsilon_i - \mu)}$,

$$F = \int d\varepsilon \; N(\varepsilon)(\varepsilon - \varepsilon_F) + e_F p$$

$$= \int d\varepsilon \; N(\varepsilon)\varepsilon - p\varepsilon_F + e_F p$$

$$= \int d\varepsilon \; N(\varepsilon)\varepsilon$$

$$= \int_0^p dp' \, \varepsilon(p', M) \tag{C.6}$$

APPENDIX D

DERIVATION OF THE MOMENTUM MATRIX ELEMENT

We are interested in calculating the momentum (D.1) of a quasi-particle incorporated in the multi-band k • p band model.

$$\frac{\hbar}{m_0}\sum_{\substack{n,n'\\ \mathbf{k},\mathbf{k}'}}\left\langle \psi_{n\mathbf{k}}\left|\hat{e}_\alpha p_\alpha\right|\psi_{n'\mathbf{k}'}\right\rangle \tag{D.1}$$

where *n* and *n'* are band indices, **k** and **k'** are wave number vectors, m_0 is bare electron mass, and ψ is total wavefunction or Bloch function, i.e., $\left|\psi_{n\mathbf{k}}\right\rangle = \left(1/\sqrt{V}\right)e^{i\mathbf{k}\cdot\mathbf{r}}\left|u_{n\mathbf{k}}\right\rangle$, in which $\left|u_{n\mathbf{k}}\right\rangle$ represents the periodic part of the Bloch function. Based on the perturbation theory expanded up to second order, the k • p Hamiltonian can be expressed as

$$D^{ij}_{nn'} \equiv \frac{\hbar}{2m_0}\delta_{ij}\delta_{nn'} + \frac{\hbar}{m_0^2}\sum_{n''}{}' \frac{\text{[illegible]}}{\varepsilon_n - \varepsilon_{n''}} \tag{D.2}$$

By substituting $\left|u_{n\mathbf{k}}\right\rangle$ expanded up to first order (D.3) into the Bloch function, one obtains (D.4).

$$u_{n\mathbf{k}} = u_{n0}(\mathbf{r}) + \frac{\hbar}{m_0}\sum_{j\neq n}\frac{\left\langle u_{j0}\left|k_\beta p_\beta\right|u_{n0}\right\rangle}{\varepsilon_{n0}-\varepsilon_{j0}}u_{j0}(\mathbf{r}) \tag{D.3}$$

$$\frac{\hbar}{m_0}\hat{e}_\alpha\sum_{\substack{n,n'\\ \mathbf{k},\mathbf{k}'}}\left\langle \psi_{n\mathbf{k}}\left|p_\alpha\right|\psi_{n'\mathbf{k}'}\right\rangle = \hat{e}_\alpha\sum_{n,n',\mathbf{k}}\left[\frac{\hbar^2}{m_0}k_\alpha\left\langle u_{n\mathbf{k}}\left|u_{n'\mathbf{k}}\right\rangle + \frac{\hbar}{m_0}\left\langle u_{n\mathbf{k}}\left|p_\alpha\right|u_{n'\mathbf{k}}\right\rangle\right]\right. \tag{D.4}$$

The subsequent use of (D.3) and (D.2) on (D.4) leads to

$$\frac{\hbar}{m_0}\sum_{\mathbf{k}}\left\langle u_{n\mathbf{k}}\left|p_\alpha\right|u_{n'\mathbf{k}}\right\rangle = \left(\frac{\hbar}{m_0}\right)^2\sum_j\frac{p^\alpha_{nj}p^\beta_{jn'}}{\varepsilon_{n'0}-\varepsilon_{j0}}k_\beta + \left(\frac{\hbar}{m_0}\right)^2\sum_j\frac{p^\beta_{nj}p^\alpha_{jn'}}{\varepsilon_{n0}-\varepsilon_{j0}}k_\beta \tag{D.5}$$

and

$$\frac{\hbar}{m_0}\hat{e}_\alpha \sum_{\substack{n,n' \\ \mathbf{k},\mathbf{k}'}} \left\langle \psi_{n\mathbf{k}} \left| p_\alpha \right| \psi_{n'\mathbf{k}'} \right\rangle = \sum_\beta \left(D_{nn'}^{\alpha\beta} + D_{nn'}^{\beta\alpha} \right) \hat{e}_\alpha k_\beta \tag{D.6}$$

It is important to notice that (D.6) can be rewritten as

$$\sum_{n,n'} \left(D_{nn'}^{\alpha\beta} + D_{nn'}^{\beta\alpha} \right) \hat{e}_\alpha k_\beta = \hat{e}_\alpha \sum_{n,n'} \frac{\partial H_{nn'}}{\partial k_\alpha} \tag{D.7}$$

since

$$\frac{\partial H_{nn'}}{\partial k_\gamma} = \sum_\beta \frac{\partial}{\partial k_\gamma} \left(k_\alpha k_\beta D_{nn'}^{\alpha\beta} \right) = \sum_\beta \left[\delta_{\alpha\gamma} k_\beta D_{nn'}^{\alpha\beta} + \delta_{\beta\gamma} k_\alpha D_{nn'}^{\alpha\beta} \right] = \sum_\beta \left[k_\beta D_{nn'}^{\gamma\beta} + k_\alpha D_{nn'}^{\alpha\gamma} \right] \tag{D.8}$$

Therefore, the momentum matrix elements between occupied $\left| a \right\rangle$ and unoccupied states $\left| b \right\rangle$ become

$$\left\langle a \left| \hat{e}_\alpha p_\alpha \right| b \right\rangle = \frac{\hbar}{m_0} \sum_{n,n',\mathbf{k},\mathbf{k}'} \left\langle a \left| \psi_{n\mathbf{k}} \right. \right\rangle \left\langle \psi_{n\mathbf{k}} \left| \hat{e}_\alpha p_\alpha \right| \psi_{n'\mathbf{k}'} \right\rangle \left\langle \psi_{n'\mathbf{k}'} \left| b \right. \right\rangle \tag{D.9}$$

$$= \frac{m_0}{\hbar} \sum_{n,n',\mathbf{k},\mathbf{k}'} \left\langle a \left| \psi_{n\mathbf{k}} \right. \right\rangle \left(\hat{e}_\alpha \frac{\partial H_{nn'}}{\partial k_\alpha} \right) \left\langle \psi_{n'\mathbf{k}'} \left| b \right. \right\rangle \tag{D.10}$$

$$\approx \frac{m_0}{\hbar} \sum_{n,n'} \left\langle a \left| u_{n0} \right. \right\rangle \left(\hat{e}_\alpha \frac{\partial H_{nn'}}{\partial k_\alpha} \right) \left\langle u_{n'0} \left| b \right. \right\rangle \tag{D.11}$$

Fig. D-1. shows an example of p_{CB-HH}^{x} for the interband transition between the conduction band and the heavy hole band with magnetization direction [100], spin exchange interaction in unstrained GaMnAs.

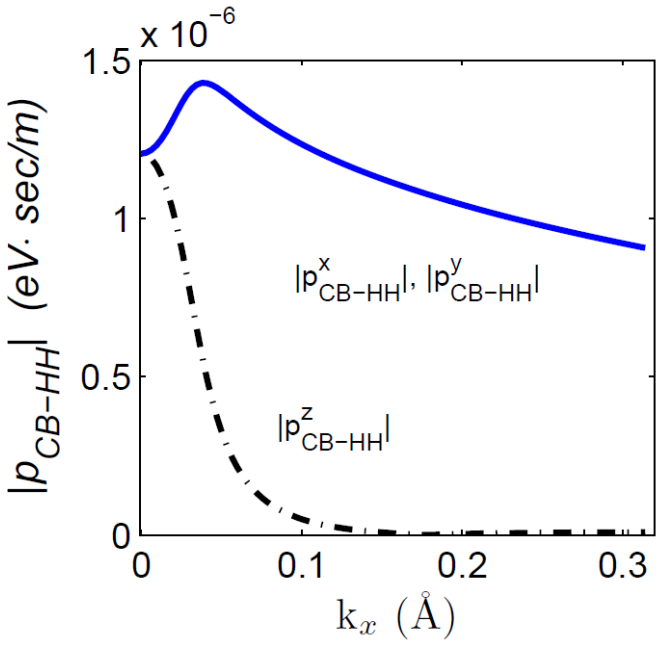

Fig. D-1. Momentum matrix elements in the interband transition between CB and HH band based on the 8-band k • p model for GaMnAs.

APPENDIX E

E.1 DERIVATIONS OF OPTICAL SUSCEPTIBILITIES AND COUPLED WAVE EQUATIONS IN A LOSSY MEDIUM

From the Maxwell equations for a single mode in non-magnetic materials with the assumption that the dielectric constant and the conductivity do not depend on time in the linear response regime, the wave equation for transverse components can be written in the SI unit as

$$-\nabla^2\widetilde{\mathbf{E}}_\perp - \mu_0\varepsilon_\perp\omega_n^2\widetilde{\mathbf{E}}_\perp = \mu\omega_n^2\widetilde{\mathbf{P}}_\perp^{NL} \tag{E.1}$$

where the time derivative $\partial/\partial t$ was replaced by $-i\omega_n t$, and the dielectric constant is $\varepsilon = \varepsilon_\perp + \varepsilon_{||}$. By using

$$\widetilde{\mathbf{E}}_\perp = F_n(y,z)e^{ik_n x - i\omega t} + c.c \tag{E.2}$$

and approximating that the nonlinear optical susceptibilities in the transverse direction are negligible, (E.1) becomes

$$\left(\frac{\partial^2}{\partial y^2} + \frac{\partial^2}{\partial z^2}\right)F_n(y,z) + \left(\mu_0\varepsilon_\perp\omega_n^2 - k_n^2\right)F_n(y,z) = 0 \tag{E.3}$$

Now we take into account the wave equation with free carrier losses, i.e.,

$$-\nabla^2\widetilde{\mathbf{E}}_n - \mu_0\varepsilon_\perp\omega_n^2\widetilde{\mathbf{E}}_n - i\mu_0\sigma_n\omega_n\widetilde{\mathbf{E}}_n = \mu\omega_n^2\widetilde{\mathbf{P}}_n \tag{E.4}$$

where we have used that $\widetilde{\mathbf{P}}_n = \varepsilon_{||}\widetilde{\mathbf{E}} + \widetilde{\mathbf{P}}^{NL}$, and the nonlinear optical susceptibilities are in a function of x. By using the electric field and polarization of

$$\widetilde{\mathbf{E}}_n = e_n(x)F_n(y,z)e^{i(k_n x - \omega_n t)} + c.c. \equiv \mathbf{E}_n e^{-i\omega_n t} + c.c. \tag{E.5}$$

$$\widetilde{\mathbf{P}}_n = \mathbf{P}_n(x,y,z)\, e^{-i\omega_n t} + c.c \tag{E.6}$$

and substituting them into (E.4) with assuming that $e_n(x)$ is slowly varying with respect to the propagating direction *x*, then neglecting the second derivative with respect to *x*, (E.4) can be written as

$$-\left[\left(2ik_n \frac{de_n(x)}{dx}\right) + \left(\frac{\partial^2}{\partial y^2} + \frac{\partial^2}{\partial z^2} + \left(\mu_0 \varepsilon_\perp \omega_n^2 - k_n^2\right)\right)\right] e^{ik_n x} F_n(y,z)$$

$$= i\mu_0 \sigma_n \omega_n e_n(x) F_n(y,z) e^{ik_n x} + \mu_0 \omega_n^2\, \mathbf{P}_n(x,y,z) \tag{E.7}$$

Note that the same exponential terms are equated in (E.7), causing to drop the other complex conjugate terms. Using (E.3), (E.7) is simplified to

$$-\left(2ik_n \frac{de_n(x)}{dx}\right) e^{ik_n x} F_n(y,z) = i\mu_0 \sigma_n \omega_n e_n(x) F_n(y,z) e^{ik_n x} + \mu_0 \omega_n^2\, \mathbf{P}_n(x,y,z) \tag{E.8}$$

where k_n is the solution of (E.3). Since now the complex conjugate terms are absent through (E.7~8), the trace is not taken, i.e.,

$$\mathbf{P}_n = N(\mathbf{d}_{nm} \boldsymbol{\sigma}_{mn}) \tag{E.9}$$

Here *N* indicates the total free carrier density in a structure, $\mathbf{d}_{nm}$ is the dipole moment between subbands *n* and *m*, and $\boldsymbol{\sigma}_{mn}$ is the off-diagonal element of the density matrix between subbands *m* and *n*.

Multiplying $F_n^*(y,z)$ and integrating over *y*-*z* plane in (E.8) lead to

$$\frac{de_n(x)}{dx} = -\frac{\mu_0 \sigma_n \omega_n}{2k_n} e_n(x) + \frac{i\mu_0 \omega_n^2 e^{-ik_n x}}{2k_n} \frac{\int_{-\infty}^{\infty}\int_{-\infty}^{\infty} F_n^*(y,z)\, \mathbf{P}_n(x,y,z)\, dydz}{\int_{-\infty}^{\infty}\int_{-\infty}^{\infty} \left|F_n(y,z)\right|^2 dydz} \tag{E.10}$$

where x is the propagating direction of fields, and z is the sample growth direction. The polarization is expanded in terms of the susceptibilities $\chi^{(m)}$ as

$$\mathbf{P}_n = \varepsilon_0 \chi_n^{(1)} \mathbf{E}_n + \varepsilon_0 \chi_n^{(2)} \mathbf{E}_l \mathbf{E}_m + \cdots \equiv \varepsilon_0 \chi_n^{(1)} \mathbf{E}_n + \mathbf{P}_n^{NL} \tag{E.11}$$

Then, (E.10) becomes

$$\frac{de_n(x)}{dx} = -\frac{\mu_0 \sigma_n \omega_n}{2k_n} e_n(x) + \frac{i\varepsilon_0 \mu_0 \omega_n^2 \chi_n^{(1)}(x) \Gamma_n^{(1)}}{2k_n} e_n(x) + \frac{i\mu_0 \omega_n^2 e^{-ik_n x}}{2k_n} \frac{\int_{-\infty}^{\infty}\int_{-\infty}^{\infty} F_n^*(y,z)\, \mathbf{P}_n^{NL}\, dydz}{\int_{-\infty}^{\infty}\int_{-\infty}^{\infty} \left|F_n(y,z)\right|^2 dydz} \tag{E.12}$$

where the confinement factor for the linear term is defined as

$$\Gamma_n^{(1)} = \frac{\iint_{AR} \left|F_n(y,z)\right|^2 dydz}{\int_{-\infty}^{\infty}\int_{-\infty}^{\infty} \left|F_n(y,z)\right|^2 dydz} \tag{E.13}$$

and the first term and the real part of the second term represent the free carrier losses and the resonant losses respectively.

The density matrix equations[31, 32] for the three-level medium schematically shown in Fig. 1-4 take the following form:

$$\frac{d\sigma_{mn}}{dt} + \Gamma_{mn}\sigma_{mn} = \frac{i}{\hbar}\sum_{q=1}^{3}\left(d_{mq}E_{mq}\sigma_{qn} - d_{qn}E_{qn}\sigma_{mq}\right)$$

$$\frac{d\sigma_{nn}}{dt} + R_n = \frac{i}{\hbar}\sum_{q=1}^{3}\left(d_{nq}E_{nq}\sigma_{qn} - d_{qn}E_{qn}\sigma_{nq}\right)$$

$$\sum_n \sigma_{nn} = 1$$

where $\Gamma_{mn} = \gamma_{mn} + i(\omega_{mn} - \omega_0)$, γ_{mn} is the line broadening at the half width at half maximum (HWHM), and ω_{mn} is the intersubband transition frequency, and ω_0 is the field frequency. R_n can be specifically expressed as

$$R_1 = (r_{12} + r_{13})n_1 - r_{21}n_2 - r_{31}n_3$$

$$R_2 = (r_{21} + r_{23})n_2 - r_{12}n_1 - r_{32}n_3$$

$$R_3 = (r_{31} + r_{32})n_3 - r_{13}n_1 - r_{23}n_2$$

where r_{nm} is the relaxation rate, and $n_m = \sigma_{mm}$.

By keeping terms up to the first order with respect to the difference frequency field e_3 since it is much weaker compared to pump fields, the off-diagonal elements are solved to be

$$\begin{aligned}\sigma_{21} = {} & \frac{-i\Omega_{21}}{\tilde{\Gamma}_{21}} n_{21} + \frac{\Omega_{23}\Omega_{31}}{\tilde{\Gamma}_{21}}\left(\frac{n_{32}}{\tilde{\Gamma}_{23}} + \frac{n_{31}}{\Gamma_{31}}\right) + \frac{i|\Omega_{31}|^2\Omega_{21}}{\tilde{\Gamma}_{21}\tilde{\Gamma}_{23}}\left(\frac{n_{31}}{\tilde{\Gamma}_{13}} + \frac{n_{21}}{\Gamma_{21}}\right) \\ & - \frac{\Omega_{31}\Omega_{23}}{\tilde{\Gamma}_{21}\tilde{\Gamma}_{23}}\left(\frac{|\Omega_{31}|^2}{\tilde{\Gamma}_{21}\Gamma_{31}} n_{31} - \frac{|\Omega_{12}|^2}{\tilde{\Gamma}_{13}\Gamma_{12}} n_{21}\right) - \frac{\Omega_{23}|\Omega_{21}|^2\Omega_{31}}{\Gamma_{31}\tilde{\Gamma}_{21}\tilde{\Gamma}_{32}}\left(\frac{n_{31}}{\tilde{\Gamma}_{31}} + \frac{n_{21}}{\tilde{\Gamma}_{12}}\right) \\ & + \frac{\Omega_{31}\Omega_{23}}{\tilde{\Gamma}_{21}} \frac{|\Omega_{12}|^2|\Omega_{13}|^2}{|\tilde{\Gamma}_{23}|^2}\left(\frac{n_{31}}{\tilde{\Gamma}_{13}} + \frac{n_{21}}{\tilde{\Gamma}_{12}}\right)\left(\frac{1}{\tilde{\Gamma}_{21}\Gamma_{31}} - \frac{1}{\tilde{\Gamma}_{13}\Gamma_{12}}\right)\end{aligned} \tag{E.14}$$

$$\sigma_{31} = \frac{-i\Omega_{31}}{\tilde{\Gamma}_{31}} n_{31} + \frac{\Omega_{21}\Omega_{32}}{\tilde{\Gamma}_{31}}\left(\frac{n_{23}}{\tilde{\Gamma}_{32}} + \frac{n_{21}}{\Gamma_{21}}\right) + \frac{i|\Omega_{21}|^2\Omega_{31}}{\tilde{\Gamma}_{31}\tilde{\Gamma}_{32}}\left(\frac{n_{31}}{\tilde{\Gamma}_{31}} + \frac{n_{21}}{\Gamma_{12}}\right)$$

$$+\frac{\Omega_{21}\Omega_{32}}{\tilde{\Gamma}_{31}\tilde{\Gamma}_{32}}\left(\frac{\left|\Omega_{31}\right|^2}{\tilde{\Gamma}_{12}\Gamma_{13}}n_{31}-\frac{\left|\Omega_{12}\right|^2}{\tilde{\Gamma}_{31}\Gamma_{21}}n_{21}\right)-\frac{\Omega_{32}\left|\Omega_{31}\right|^2\Omega_{21}}{\Gamma_{21}\tilde{\Gamma}_{31}\tilde{\Gamma}_{32}}\left(\frac{n_{31}}{\tilde{\Gamma}_{13}}+\frac{n_{21}}{\tilde{\Gamma}_{21}}\right)$$

$$-\frac{\Omega_{21}\Omega_{32}}{\tilde{\Gamma}_{31}}\frac{\left|\Omega_{12}\right|^2\left|\Omega_{13}\right|^2}{\left|\tilde{\Gamma}_{32}\right|^2}\left(\frac{n_{31}}{\tilde{\Gamma}_{13}}+\frac{n_{21}}{\tilde{\Gamma}_{21}}\right)\left(\frac{1}{\tilde{\Gamma}_{12}\Gamma_{13}}-\frac{1}{\tilde{\Gamma}_{31}\Gamma_{21}}\right) \tag{E.15}$$

$$\sigma_{32}=\frac{-i\Omega_{32}}{\tilde{\Gamma}_{32}}n_{32}-\frac{\Omega_{12}\Omega_{31}}{\tilde{\Gamma}_{32}}\left(\frac{n_{31}}{\tilde{\Gamma}_{31}}+\frac{n_{21}}{\tilde{\Gamma}_{12}}\right)+\frac{i\Omega_{32}}{\tilde{\Gamma}_{32}}\left(\frac{\left|\Omega_{31}\right|^2}{\tilde{\Gamma}_{12}\Gamma_{13}}n_{31}-\frac{\left|\Omega_{12}\right|^2}{\tilde{\Gamma}_{31}\Gamma_{21}}n_{21}\right)$$

$$-\frac{i\left|\Omega_{12}\right|^2\left|\Omega_{13}\right|^2}{\left|\tilde{\Gamma}_{32}\right|^2}\Omega_{32}\left(\frac{n_{31}}{\tilde{\Gamma}_{13}}+\frac{n_{21}}{\tilde{\Gamma}_{21}}\right)\left(\frac{1}{\tilde{\Gamma}_{12}\Gamma_{13}}-\frac{1}{\tilde{\Gamma}_{31}\Gamma_{21}}\right) \tag{E.16}$$

where $n_{pq}\equiv\sigma_{pp}-\sigma_{qq}$, $\Omega_{mn}=d_{mn}E_{mn}/\hbar$, $\Omega_{mn}=\Omega_{nm}^{*}$, $\Gamma_{mn}=\Gamma_{nm}^{*}$,

$$\tilde{\Gamma}_{32}=\Gamma_{32}+\frac{\left|\Omega_{12}\right|^2}{\tilde{\Gamma}_{31}}+\frac{\left|\Omega_{13}\right|^2}{\tilde{\Gamma}_{12}} \tag{E.17}$$

$$\tilde{\Gamma}_{21}=\Gamma_{21}+\frac{\left|\Omega_{32}\right|^2}{\Gamma_{31}}, \tag{E.18}$$

$$\tilde{\Gamma}_{31}=\Gamma_{31}+\frac{\left|\Omega_{32}\right|^2}{\Gamma_{21}}. \tag{E.19}$$

All non-zero susceptibilities are obtained by equating (E.9) and (E.11) along with replacing σ_{nm} by (E.14) ~ (E.16) and approximating that $\tilde{\Gamma}_{21}=\Gamma_{21}$ and $\tilde{\Gamma}_{31}=\Gamma_{31}$. The approximation is appropriate because of the very weak difference frequency field. The resulting optical susceptibilities are followed as

$$\chi_1^{(1)}=\frac{N}{\varepsilon_0\hbar}\frac{\left|d_{12}\right|^2}{i\Gamma_{21}}n_{21} \tag{E.20}$$

$$\chi_2^{(1)} = \frac{N}{\varepsilon_0 \hbar} \frac{\left|d_{13}\right|^2}{i\Gamma_{31}} n_{31} \tag{E.21}$$

$$\chi_3^{(1)} = \frac{N}{\varepsilon_0 \hbar} \frac{\left|d_{23}\right|^2}{i\widetilde{\Gamma}_{32}} n_{32} \tag{E.22}$$

$$\chi_1^{(2)} = \frac{N}{\varepsilon_0 \hbar^2} d_{12} d_{23} d_{31} \left(\frac{n_{32}}{\Gamma_{21}\widetilde{\Gamma}_{23}} + \frac{n_{31}}{\Gamma_{21}\Gamma_{31}} \right) \tag{E.23}$$

$$\chi_2^{(2)} = \frac{N}{\varepsilon_0 \hbar^2} d_{13} d_{32} d_{21} \left(\frac{n_{23}}{\Gamma_{31}\widetilde{\Gamma}_{32}} + \frac{n_{21}}{\Gamma_{31}\Gamma_{21}} \right) \tag{E.24}$$

$$\chi_3^{(2)} = \frac{N}{\varepsilon_0 \hbar^2} d_{23} d_{31} d_{12} \left(\frac{n_{13}}{\Gamma_{31}\widetilde{\Gamma}_{32}} + \frac{n_{12}}{\Gamma_{12}\widetilde{\Gamma}_{32}} \right) \tag{E.25}$$

$$\chi_1^{(3)} = \frac{N}{\varepsilon_0 \hbar^3} \frac{i\left|d_{31}\right|^2 \left|d_{21}\right|^2}{\widetilde{\Gamma}_{23}\Gamma_{21}} \left(\frac{n_{31}}{\Gamma_{13}} + \frac{n_{21}}{\Gamma_{21}} \right) \tag{E.26}$$

$$\chi_2^{(3)} = \frac{N}{\varepsilon_0 \hbar^3} \frac{i\left|d_{31}\right|^2 \left|d_{21}\right|^2}{\widetilde{\Gamma}_{32}\Gamma_{31}} \left(\frac{n_{31}}{\Gamma_{31}} + \frac{n_{21}}{\Gamma_{12}} \right) \tag{E.27}$$

$$\chi_{3,1}^{(3)} = \frac{N}{\varepsilon_0 \hbar^3} \frac{i\left|d_{23}\right|^2 \left|d_{31}\right|^2}{\widetilde{\Gamma}_{32}\Gamma_{12}\Gamma_{13}} n_{31} \tag{E.28}$$

$$\chi_{3,2}^{(3)} = \frac{N}{\varepsilon_0 \hbar^3} \frac{i\left|d_{23}\right|^2 \left|d_{21}\right|^2}{\widetilde{\Gamma}_{32}\Gamma_{31}\Gamma_{21}} n_{12} \tag{E.29}$$

$$\chi_{1,1}^{(4)} = \frac{N}{\varepsilon_0 \hbar^4} d_{12} d_{23} d_{31} \left|d_{12}\right|^2 \left(\frac{n_{21}}{\left|\Gamma_{21}\right|^2} i2\,\mathrm{Im}\left(\frac{1}{\widetilde{\Gamma}_{23}\Gamma_{13}} \right) - \frac{n_{31}}{\left(\Gamma_{31}\right)^2 \Gamma_{21}\widetilde{\Gamma}_{32}} \right) \tag{E.30}$$

$$\chi_{1,2}^{(4)} = \frac{N}{\varepsilon_0 \hbar^4} d_{12} d_{23} d_{31} \left| d_{13} \right|^2 \frac{n_{13}}{\left(\Gamma_{21}\right)^2 \Gamma_{31} \widetilde{\Gamma}_{23}} \tag{E.31}$$

$$\chi_{2,1}^{(4)} = \frac{N}{\varepsilon_0 \hbar^4} d_{13} d_{32} d_{21} \left| d_{31} \right|^2 \left(\frac{n_{31}}{\left|\Gamma_{31}\right|^2} i2 \,\mathrm{Im}\left(\frac{1}{\widetilde{\Gamma}_{32} \Gamma_{12}} \right) - \frac{n_{21}}{\left(\Gamma_{21}\right)^2 \Gamma_{31} \widetilde{\Gamma}_{23}} \right) \tag{E.32}$$

$$\chi_{2,2}^{(4)} = \frac{N}{\varepsilon_0 \hbar^4} d_{13} d_{32} d_{21} \left| d_{12} \right|^2 \frac{n_{12}}{\left(\Gamma_{31}\right)^2 \Gamma_{21} \widetilde{\Gamma}_{32}} \tag{E.33}$$

Using (E.11) with the above non-zero optical susceptibilities, the coupled wave equation (E.12) is explicitly expressed as,

$$\frac{de_1}{dx} + \frac{\mu_0 \sigma_n \omega_1}{2k_1} e_1(x) - \frac{i\varepsilon_0 \mu_0 \omega_1^2 \chi_1^{(1)}(x) \Gamma_1^{(1)}}{2k_1} e_1(x)$$

$$= \frac{i\varepsilon_0 \mu_0 \omega_1^2}{2k_1} \Gamma \left(\chi_1^{(2)} e_2 e_3^* e^{-i\Delta kx} + \chi_1^{(3)} \left| e_2 \right|^2 e_1 + \left(\chi_{1,1}^{(4)} \left| e_1 \right|^2 + \chi_{1,2}^{(4)} \left| e_2 \right|^2 \right) e_2 e_3^* e^{-i\Delta kx} \right) \tag{E.34}$$

$$\frac{de_2}{dx} + \frac{\mu_0 \sigma_n \omega_2}{2k_2} e_2(x) - \frac{i\varepsilon_0 \mu_0 \omega_2^2 \chi_2^{(1)}(x) \Gamma_2^{(1)}}{2k_2} e_2(x)$$

$$= \frac{i\varepsilon_0 \mu_0 \omega_2^2}{2k_2} \Gamma \left(\chi_2^{(2)} e_3 e_1 e^{i\Delta kx} + \chi_2^{(3)} \left| e_1 \right|^2 e_2 + \left(\chi_{2,1}^{(4)} \left| e_2 \right|^2 + \chi_{2,2}^{(4)} \left| e_1 \right|^2 \right) e_3 e_1 e^{i\Delta kx} \right) \tag{E.35}$$

$$\frac{de_3}{dx} + \frac{\mu_0 \sigma_n \omega_3}{2k_3} e_3(x) - \frac{i\varepsilon_0 \mu_0 \omega_3^2 \chi_3^{(1)}(x) \Gamma_3^{(1)}}{2k_3} e_3(x)$$

$$= \frac{i\varepsilon_0 \mu_0 \omega_3^2}{2k_3} \Gamma \left(\chi_3^{(2)} e_1^* e_2 e^{-i\Delta kx} + \left(\chi_{3,1}^{(3)} \left| e_2 \right|^2 + \chi_{3,2}^{(3)} \left| e_1 \right|^2 \right) e_3 \right) \tag{E.36}$$

where we approximated that $\Gamma \equiv \Gamma^{(2)} \approx \Gamma^{(3)} \approx \Gamma^{(4)}$, and

$$\Gamma^{(2)} = \frac{\iint_{AR} \left(F_1(y,z)\right)^* F_2(y,z) \left(F_3(y,z)\right)^* dydz}{\int_{-\infty}^{\infty} \int_{-\infty}^{\infty} \left|F_1(y,z)\right|^2 d\,ydz} \approx \frac{\iint_{AR} \left(F_2(y,z)\right)^* F_3(y,z) F_1(y,z) dydz}{\int_{-\infty}^{\infty} \int_{-\infty}^{\infty} \left|F_2(y,z)\right|^2 d\,ydz}$$

$$\approx \frac{\iint_{AR} (F_3(y,z))^* F_2(y,z)(F_1(y,z))^* dydz}{\int_{-\infty}^{\infty}\int_{-\infty}^{\infty} |F_3(y,z)|^2 d\,ydz}$$

$$\Gamma^{(3)} = \frac{\iint_{AR} |F_1(y,z)|^2 |F_2(y,z)|^2 dydz}{\int_{-\infty}^{\infty}\int_{-\infty}^{\infty} |F_1(y,z)|^2 d\,ydz} \approx \frac{\iint_{AR} |F_1(y,z)|^2 |F_2(y,z)|^2 dydz}{\int_{-\infty}^{\infty}\int_{-\infty}^{\infty} |F_2(y,z)|^2 d\,ydz}$$

$$\approx \frac{\iint_{AR} |F_2(y,z)|^2 |F_3(y,z)|^2 dydz}{\int_{-\infty}^{\infty}\int_{-\infty}^{\infty} |F_3(y,z)|^2 d\,ydz} \approx \frac{\iint_{AR} |F_1(y,z)|^2 |F_3(y,z)|^2 dydz}{\int_{-\infty}^{\infty}\int_{-\infty}^{\infty} |F_3(y,z)|^2 d\,ydz}$$

$$\Gamma^{(4)} = \frac{\iint_{AR} (F_1(y,z))^* F_2(y,z)(F_3(y,z))^* |F_1(y,z)|^2 dydz}{\int_{-\infty}^{\infty}\int_{-\infty}^{\infty} |F_1(y,z)|^2 d\,ydz}$$

$$\approx \frac{\iint_{AR} (F_1(y,z))^* F_2(y,z)(F_3(y,z))^* |F_2(y,z)|^2 dydz}{\int_{-\infty}^{\infty}\int_{-\infty}^{\infty} |F_1(y,z)|^2 d\,ydz}$$

$$\approx \frac{\iint_{AR} (F_2(y,z))^* F_3(y,z)F_1(y,z)|F_2(y,z)|^2 dydz}{\int_{-\infty}^{\infty}\int_{-\infty}^{\infty} |F_2(y,z)|^2 d\,ydz}$$

$$\approx \frac{\iint_{AR} (F_2(y,z))^* F_3(y,z)F_1(y,z)|F_1(y,z)|^2 dydz}{\int_{-\infty}^{\infty}\int_{-\infty}^{\infty} |F_2(y,z)|^2 d\,ydz}$$

If the contribution of terms higher than the second order is much smaller than the second order term, the coupled wave equations can be written in more compact forms.

$$\frac{de_1}{dx} + \frac{1}{2}\left[\alpha_1(x) - \frac{i\varepsilon_0\mu_0\omega_1^2 \,\mathrm{Re}\left(\chi_1^{(1)}(x)\right)\Gamma_1^{(1)}}{k_1}\right]e_1(x) = \frac{i\varepsilon_0\mu_0\omega_1^2}{2k_1}\Gamma\chi_1^{(2)}(x)e_2e_3^*e^{-i\Delta kx} \qquad \text{(E.37)}$$

$$\frac{de_2}{dx} + \frac{1}{2}\left[\alpha_2(x) - \frac{i\varepsilon_0\mu_0\omega_2^2 \,\mathrm{Re}\left(\chi_2^{(1)}(x)\right)\Gamma_2^{(1)}}{k_2}\right]e_2(x) = \frac{i\varepsilon_0\mu_0\omega_2^2}{2k_2}\Gamma\chi_2^{(2)}(x)e_3e_1e^{i\Delta kx} \qquad \text{(E.38)}$$

$$\frac{de_3}{dx}+\frac{1}{2}\left[\alpha_3(x)-\frac{i\varepsilon_0\mu_0\omega_3^2\,\mathrm{Re}\left(\chi_3^{(1)}(x)\right)\Gamma_3^{(1)}}{k_3}\right]e_3(x)=\frac{i\varepsilon_0\mu_0\omega_3^2}{2k_3}\Gamma\chi_3^{(2)}(x)e_1^*e_2e^{-i\Delta kx} \quad \text{(E.39)}$$

where $\alpha_n(x)=\alpha_n^{fca}+\Gamma_n^{(1)}(x)\alpha_n^{res}(x)$, and α_n^{fca}, the free carrier absorption (fca) and $\alpha_n^{res}(x)$, the resonant absorption are given as

$$\alpha_n^{fca}=\frac{\mu_0\sigma_n\omega_n}{k_n} \quad \text{(E.40)}$$

$$\alpha_n^{res}(x)=\frac{\varepsilon_0\mu_0\omega_n^2}{k_n}\mathrm{Im}\left(\chi_n^{(1)}(x)\right) \quad \text{(E.41)}$$

where sub-index *n* indicates each field.

E.2 THz DFG POWER IN LIMITING PUMP POWERS

Now we express the DFG output power with a single analytical expression in two limiting cases: a very weak and a very strong pump power. Basically, the difference between the two cases comes from the distinctive subband populations (n_m), which affect the linear and the second order susceptibilities in (E.20) ~ (E.25). First, in the weak pump power regime all electrons are approximately in the ground state, i.e., $n_{12}(=n_1-n_2)\approx n_{13}\approx 1$. On the other hand, in the strong pump power regime electrons are nearly evenly distributed over subbands, i.e.,

$$n_{12}\approx\frac{1}{\frac{6\left|\Omega_{12}\right|^2}{r_{21}\gamma_{12}}+2},\quad n_{13}\approx\frac{1}{\frac{6\left|\Omega_{13}\right|^2}{r_{31}\gamma_{13}}+2}$$

where we assumed zero-detuning, $r_{12} \approx r_{13} = 0$, and $r_{21} >> r_{32}$. By substituting these into (E.20) for each limiting case, the linear susceptibilities for pump fields become

$$\chi_{1w}^{(1)} \approx i \frac{N}{\varepsilon_0 \hbar} \frac{|d_{12}|^2}{\gamma_{12}} \qquad \text{(weak pump)}$$

$$\chi_{1s}^{(1)} \approx i \frac{N}{\varepsilon_0 \hbar} \frac{r_{21} \hbar^2}{6|e_1|^2} \qquad \text{(strong pump)}$$

Then straightforwardly applying them to (E.41), the total absorptions become

$$\alpha_1^{weak} = \alpha_1^{fca} + \Gamma_1^{(1)} \frac{\varepsilon_0 \mu_0 \omega_1^2}{k_1} \left(\frac{N}{\varepsilon_0 \hbar} \frac{|d_{12}|^2}{\gamma_{12}} \right) \qquad \text{(weak pump)}$$

$$\alpha_1^{strong} = \alpha_1^{fca} + \Gamma_1^{(1)} \frac{\varepsilon_0 \mu_0 \omega_1^2}{k_1} \left(\frac{N}{\varepsilon_0 \hbar} \frac{r_{21} \hbar^2}{6|e_1|^2} \right) \approx \alpha_1^{fca} \qquad \text{(strong pump)}$$

and, as a result, pump field amplitudes can be written as

$$e_1^{weak} = e_0 e^{-\frac{\alpha_1^{weak}}{2} x} \qquad \text{(weak pump)}$$

$$e_1^{strong} = e_0 e^{-\frac{\alpha_1^{fca}}{2} x} \qquad \text{(strong pump)}$$

Here, e_0 is the incident pump field amplitude. Then, the second order susceptibilities in (E.25) can be written as

$$\chi_{3w}^{(2)} = \frac{2N}{\varepsilon_0 \hbar^2} \frac{d_{23} d_{31} d_{12}}{\gamma_{12} \gamma_{32}} \qquad \text{(weak pump)}$$

$$\chi_{3s}^{(2)} = \frac{N}{\varepsilon_0 \hbar^2} \frac{d_{23} r_{21} \gamma_{12} \hbar^4}{12 |d_{12}|^2 e_0^4} e^{2\alpha_1^{fca} x} \qquad \text{(strong pump)}$$

where N is the average doping density in the nonlinear active region, and we used the following with the approximation that $\gamma_{12} \approx \gamma_{13}$ and $\alpha_1^{fca} \approx \alpha_2^{fca}$.

$$\widetilde{\Gamma}_{32}^{weak} \approx \gamma_{32}$$

$$\widetilde{\Gamma}_{32}^{strong} = \frac{\left|d_{21}\right|^2}{\gamma_{12}\hbar^2} e_0^2 e^{-\alpha_1^{fca} x}$$

By substituting the above pump amplitudes, the linear and the second order susceptibility of limiting cases into (E.39) and solving for the DFG field, then the DFG power becomes

$$p_{DFG}^{weak} \approx e^{-a_3^f x} \frac{2\rho_3 A}{Z_0}\left(\frac{\varepsilon_0\mu_0\omega_3^2}{2k_3}\right)^2\left(\frac{N}{\varepsilon_0}\right)^2\left|d_{23}\right|^2\left(\Gamma^{(2)}\right)^2\left(\frac{2d_{31}d_{12}}{\gamma_{12}\gamma_{32}\hbar^2}\right)^2 e_0^4$$

$$\times\left|\frac{e^{\left(-\alpha_1^{weak}-\alpha_2^{weak}+\alpha_3^f\right)x} - 2e^{\frac{1}{2}\left(-\alpha_1^{weak}-\alpha_2^{weak}+\alpha_3^f\right)x}\cos\left(\Delta k x\right)+1}{\frac{1}{4}\left(-\alpha_1^{weak}-\alpha_2^{weak}+\alpha_3^f\right)^2+\left(\Delta k\right)^2}\right| \qquad \text{(E.42)}$$

$$p_{DFG}^{strong} \approx e^{-a_3^f x} \frac{2\rho_3 A}{Z_0}\left(\frac{\varepsilon_0\mu_0\omega_3^2}{2k_3}\right)^2\left(\frac{N}{\varepsilon_0}\right)^2\left|d_{23}\right|^2\left(\Gamma^{(2)}\right)^2\left(\frac{r_{12}\gamma_{12}\hbar^2}{12\left|d_{21}\right|^2}\right)^2\frac{1}{e_0^4}$$

$$\times\left|\frac{e^{2\left(\alpha_1^f+\frac{\alpha_3^f}{2}\right)x} - 2e^{\left(\alpha_1^f+\frac{\alpha_3^f}{2}\right)x}\cos\left(\Delta k x\right)+1}{\left(\alpha_1^f+\frac{\alpha_3^f}{2}\right)^2+\left(\Delta k\right)^2}\right| \qquad \text{(E.43)}$$

where ρ_3 and A are the modal refractive index and the modal cross section of the difference frequency field respectively, and Z_0 is the free space impedance. Note that

DFG output power depends on e_0^4 and e_0^{-4} in the very weak and the very strong pump power regimes respectively.

VITA

Name:	Yong Hee Cho
Address:	Youngtong-Gu, 1211, Maetan 2-Dong, Hangook 1-Cha APT 105-108 Suwon, Gyeonggi-Do 443-712 South Korea
Email Address:	phyleganza@hotmail.com
Education:	B.S., Physics, Hanyang University (Seoul), 2000 Ph.D., Department of Physics & Astronomy, Texas A&M University, 2011